BOS-correction of refraction for water based PIV measurements within a natural convection boundary layer

A thesis submitted to the University of Manchester for the degree of Doctor of Philosophy in the Faculty of Science and Engineering.

2022

Martyn Kendrick

Department of Mechanical, Aerospace and Civil Engineering

Contents

Acronyms

2D2C two dimension two component.

BOS background orientated schlieren.

BOS@BOS BOS conducted at the BOS plane.

BOS@PIV BOS conducted at the PIV plane.

CCD charged couple device.

CFD computational fluid dynamics.

CMOS complementary metal-oxide-semiconductor.

DAQ data acquisition.

DIC digital image correlation.

DRE data reduction equation.

DUA detailed uncertainty analysis.

FOV field of view.

HDPE high density polyethylene.

HEDH heat exchanger design handbook.

IAPWS international association for the properties of water and steam.

IR infrared.

IRT infrared thermography.

ITO tin-doped indium oxide.

LDV laser doppler velocimetry.

LIF laser induced fluorescence.

Nd:YAG neodynium yttrium aluminium garnet.

PIV particle image velocimetry.

PIV+BOS simultaneous BOS-corrected PIV.

PSU power supply unit.

PTV particle tracking velocimetry.

SET separate effect test.

SMR small modular reactor.

SNR signal to noise ratio.

TCO transparent conductive oxide.

TSM Taylor series method.

UMF uncertainty magnification factor.

UPC uncertainty percentage contribution.

V&V verification and validation.

Nomenclature

Latin letters

A	Area
A	Scaling factor
b	Seperation
b	Systematic uncertainty
d	Diameter
E	Transition variable; $E = G^*\left(\frac{\nu^2}{gx^3}\right)^{2/15}$
g	Gravitional constant
h	Convective heat transfer coefficient
$\vec{I}$	Identity vector
I	Current
k	Thermal conductivity
ℓ	Charactistic length
M	Molar weight
n	Refractive index
$\dot{Q}$	Rate of heat transfer
Q	Convected thermal energy; $Q(x) = q''x$
q''	Heat flux
R	Molar refractivity
R	Resistance
R	Thermal resistance

r Random uncertainty

s Uncertainty

T Temperature

u Uncertainty

u Velocity (flowise)

V Voltage

W Distance travelled through variable refractive index field

X Flowise direction

X Variable

x Flowise direction/distance

Y Wall normal direction

y Wall normal direction/distance

Z Transverse direction

z Transverse direction/distance

Dimensionless groups

G^* Alternative Grashof number; $G^* = 5[(1/5)Gr_x^*]^{1/5}$

Gr Grashof number; $Gr = \frac{g\beta\theta_w\ell^3}{\nu^2}$

Gr^* Modified Grashof number; $Gr^* = Gr.Nu$

Nu Nusselt number; $Nu = \frac{h\ell}{k}$

Pr Prandtl number

Ra Rayleigh number; $Ra = \frac{g\beta\theta_w\ell^3}{\alpha\nu}$

Ra^* Modified Rayleigh number; $Ra^* = Ra.Nu$

Greek letters

α Thermal diffusivity

β Volumetric thermal expansion coefficient

δ Hydrodynamic boundary layer thickness

δ Realtive uncertainty

η Similarity variable (isoflux); $\eta = \frac{yG^*}{5x}$

η Similarity variable (isothermal); $\eta = \frac{yG}{4x}$

κ Scaling factor

λ Instantaneous distortion field

$\overline{\lambda}$ Average distortion field

λ^* Instantaneous distortion field (scaled)

μ Dynamic viscosity

ν Kinematic viscosity

ρ Density

θ Sensitivity coefficient

θ Wall excess temperature; $\theta_w = T - T_\infty$

ϑ Angle of interception

$\vec{\xi}$ x-component of displacement

$\vec{\zeta}$ y-component of displacement

Subscripts

BOS BOS plane

f Film

∞ Quiescent

L Spatially averaged over length

p Particle

PIV PIV plane

r Result

w Wall

x Local (flowise)

List of Figures

List of Tables

Abstract

Particle image velocimetry (PIV) is a ubiquitous optical based experimental technique for providing high resolution measurements of the velocity and derived turbulent quantities. Such data is relied upon for the validation of computer codes which are used to design and safety assure many engineering systems in use today. A desire for greater performance and safety within nuclear reactor designs increasingly demands the use of computational fluid dynamics (CFD). To fulfil this role CFD codes and models must be validated to the exceedingly high standards of the nuclear industry which in large part is expected to be performed using PIV.

For nuclear reactors, water is the most commonly used coolant and thus the performance of CFD to simulate the related flow physics in water is of great interest. One particular area of interest is natural convection, which is relied upon in reactor designs as a passive heat removal capability in the event of emergency. Performing PIV measurements in water based natural convection experiments has traditionally been limited by the distorting effect of refraction which may result in substantial measurement error.

In this thesis high resolution PIV measurements of natural convection from a uniformly heated vertical surface submerged in thermally stratified water are performed. The relatively high heat flux results in a transition to turbulence and substantial refractive distortion and blurring. A correction method is developed to correct for the refractive distortion and some amount of blurring. The method involves performing simultaneous background orientated schlieren (BOS) measurements to measure the distortion and provide a correction for the instantaneous PIV images as a pre-processing operation.

The technical challenges of performing measurements in such circumstances and the methods employed to overcome them are discussed through this thesis. Novel methods for scaling the measured distortion and accounting for differing thermal conditions between measurements are presented. Finally, the uncorrected PIV result is compared against an instantaneous and time averaged corrected results. It is found that whilst the flow is laminar the effect of refraction is negligible, and as the flow transitions to turbulence the applicability of a time averaged correction method is limited.

Declaration

No portion of the work referred to in the thesis has been submitted in support of an application for another degree or qualification of this or any other university or other institute of learning.

Copyright statement

i The author of this thesis (including any appendices and/or schedules to this thesis) owns certain copyright or related rights in it (the "Copyright") and s/he has given the University of Manchester certain rights to use such Copyright, including for administrative purposes.

ii Copies of this thesis, either in full or in extracts and whether in hard or electronic copy, may be made **only** in accordance with the Copyright, Designs and Patents Act 1988 (as amended) and regulations issued under it or, where appropriate, in accordance with licensing agreements which the University has from time to time. This page must form part of any such copies made.

iii The ownership of certain Copyright, patents, designs, trademarks and other intellectual property (the "Intellectual Property") and any reproductions of copyright works in the thesis, for example graphs and tables ("Reproductions"), which may be described in this thesis, may not be owned by the author and may be owned by third parties. Such Intellectual Property and Reproductions cannot and must not be made available for use without the prior written permission of the owner(s) of the relevant Intellectual Property and/or Reproductions.

iv Further information on the conditions under which disclosure, publication and commercialisation of this thesis, the Copyright and any Intellectual Property and/or Reproductions described in it may take place is available in the University IP Policy (see http://documents.manchester.ac.uk/DocuInfo.aspx?DocID=24420), in any relevant Thesis restriction declarations deposited in the University Library, the University Library's regulations (see http://www.library.manchester.ac.uk/about/regulations/) and in the University's policy on Presentation of Theses.

Acknowledgements

Over the nine years this work was conducted I have been advised, supported, inspired and enabled by many people to whom I owe thanks.

The study, apparatus and preparation of this thesis would not have been possible without the funding provided by the Nuclear Department, Ministry of Defence, UK. My thanks to all my colleagues who have discussed, supported, inspired and advised me over the years. In particular I would like to thank Dr Simon Jewer for his support.

I would also like to offer thanks to my supervisory team; Prof Hector Iacovides and Dr Tim Craft for their guidance in the preparation of this thesis. Thanks also to my examiners Dr Yasser Mahmoudi Iarimi and Dr Hossein Zare-Behtash for their advice and critique.

I must also acknowledge the technical support provided by Dr Alex Charogiannis of LaVision with whom I spoke on many occasions; usually in the midst of despair!

Finally, I offer thanks to my mother and my wife for their encouragement, support and patience.

Chapter 1

Introduction

Optical flow visualisation techniques are ubiquitous experimental tools which are applied to a vast array of fluid dynamic and thermo-fluid engineering challenges. A routine application of these techniques is in the validation of high fidelity analytical methods such as computational fluid dynamics (CFD). Once validated, the results of the analytical method may be used to inform the design of, or safety justify, engineered components or systems. Validation becomes increasingly important if the system or components are safety critical or the consequences of failure are high. Thus, the validity of experimental validation data is critical since it is relied upon to provide confidence and credibility in the analytical method.

Uncertainty quantification is of significance to the design and justification of safety critical components or systems. Bestion et al.[1] recently posited this as a holistic problem whereby the overall uncertainty is a combination of the analysis conducted and the supporting validation work. Briefly, the validation data only reduces the overall uncertainty if it has less uncertainty than the analytical method. Whilst this is perhaps a little obvious, it demonstrates the requirement and motivation to reduce the uncertainty in experimental measurements as the accuracy of analytical methods improves.

Another motivation to examine experimental error and uncertainty comes from application to new phenomena. Analytical methods such as CFD are increasingly applied to more varied, complex or safety critical challenges. Thus it is necessary to similarly apply optical flow visualisation techniques to these varied, complex or safety critical challenges. However, some of these applications introduce fundamental difficulties in applying optical flow visualisation techniques. For example, achieving sufficient optical access, providing sufficient illumination and the introduction of phenomena induced optical distortion. The latter of these is the subject of this thesis, in particular the error introduced by refractive distortion on the measurement of flow quantities.

The effect of *thermally induced* refractive distortion is shown in Figure 1.1. In Figure 1.1a a reference target is shown submerged in water and adjacent to a heating surface with no heating applied. Figure 1.1b shows the same target with power being supplied to the heater. It may be seen that the image becomes blurred and distorted due to the presence of the resultant thermal

gradient in the water. This thermal gradient results in a density gradient thus a gradient in the refractive index of the water. It is this variation in refractive index that causes the observed distortion and blurring. The effect of the distortion on the velocity is shown in Figure 1.1c. This shows the difference between the uncorrected, and therefore distorted, velocity profile and corrected velocity profiles. Furthermore, the profiles are shown at two different x (distance from the leading edge of the heating surface) locations. The detail of the applied correction is discussed later in this thesis, for now it may be seen that at the $x = 100$ mm location the correction makes little difference. However, at $x = 175$ mm the uncorrected velocity has nearly double the magnitude and the shape of the velocity profile is quite different compared to the corrected profiles. Plainly, the effect of refractive distortion is to measure an errant velocity at an errant location.

This example serves to show that the effects of refractive distortion can be substantial and should ideally be corrected or at least contribute to the uncertainty of flow quantities of interest. Whilst a temperature gradient is the cause of refractive distortion in this example, similar effects could result from other gradients such as concentration, compressibility or chemical reaction etc. Furthermore, velocity is not the only quantity affected. Other vectorial or derived quantities such as turbulence and pressure are naturally affected. However, optically measured scalar quantities such as temperature and concentration may also have an errant location.

Thermally induced refractive distortion can be expected to occur wherever a substantial thermal gradient is present. Examples of such cases of engineering interest include;

- Mixing flows i.e. jets or T-junctions with a large temperature difference
- Convective flows i.e. within the forced or natural boundary layer on a heated surface with sufficiently high heat flux

Thus, such cases are naturally more challenging to apply flow visualisation techniques to except for where the effect of thermally induced refractive distortion is negligible. The requirement for negligible refractive distortion is therefore bounding on what range of parameters can be measured i.e. limited temperature difference or heat flux.

Unlike other phenomena, buoyancy driven flow cannot be attained without a density gradient and thus refractive distortion is inevitable. In particular, natural convection is relied upon in many engineering applications to remove heat and nowhere is this more safety critical than in the removal of heat within a nuclear reactor core. Historically natural convection and circulation phenomena have been used as a passive safety mechanisms to provide cooling in the event of an emergency[2,3]. However, some small modular reactor (SMR) designs aim to take this further and rely solely on natural convection and circulation for the removal of heat in normal operation - and thus with much greater heat flux. This increased employment and reliance on natural convection and circulation has renewed academic interest in the phenomena. To enable the application of modern analytical methods, such as CFD, it is therefore necessary to provide high fidelity validation data. In turn, this requires a wider range of parameters and fluids to be investigated; notably higher heat flux and water, respectively. Thus, it is necessary to investigate and address

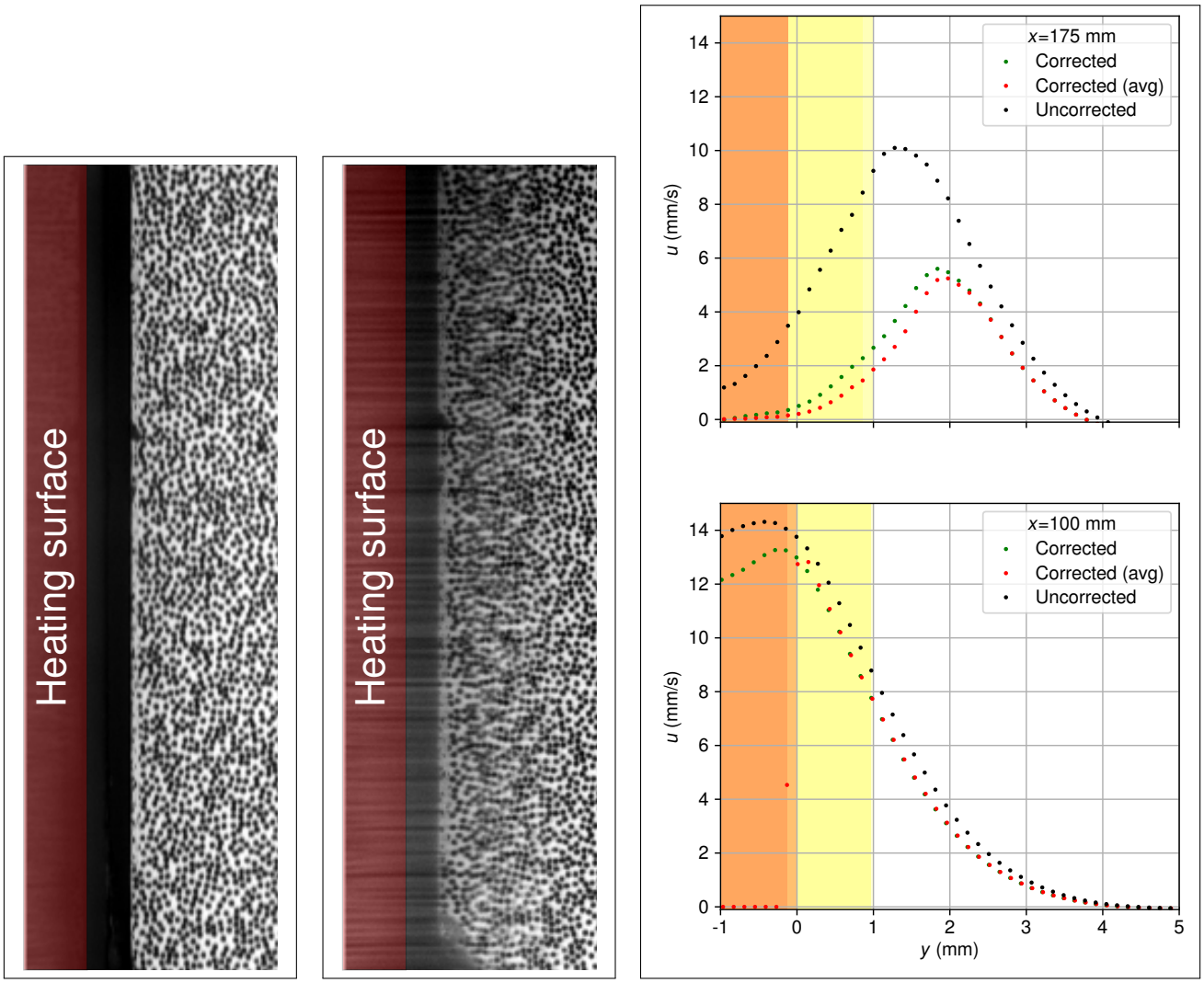

(a) (b) (c)

Figure 1.1: The effect of thermally induced refractive distortion from a naturally convecting heated surface (located to the left). Included are the; (a) undistorted reference pattern, (b) distorted reference pattern and (c) the resultant measured velocity profile.

the error introduced by thermally induced refractive distortion.

The objectives of the work documented in this thesis are:

- Design an experimental apparatus and procedure to measure the effect of thermally induced refractive distortion on flow quantities measured using state-of-the-art flow visualisation techniques.
- Develop a correction method to account for the effects of thermally induced refractive distortion.
- Investigate the extent to which the effects of thermally induced refractive distortion can be considered negligible.

Natural convection from a vertical heated surface is the phenomena investigated, however, it is expected that the insights and methodologies developed can be applied more generally beyond this case.

1.1 Outline of the thesis

In chapter 2 the literature relating to natural convection and refractive distortion is reviewed. The experimental apparatus and a detailed uncertainty analysis of the experimental conditions is provided in chapter 3. Chapter 4 introduces the novel methodology and techniques used for measurement, correction and analysis. Results and discussion are presented in chapter 5 with the main conclusions and recommendations for further work summarised in chapter 6.

Chapter 2

Literature survey

The objectives of this literature survey are to introduce the fundamental characteristics of natural convection flows, the challenges of applying PIV to such flows, and, the methodologies proposed to overcome them.

The amount of literature relating to natural convection flows is vast owing to a century of research effort on the topic. Hence, the scope is limited to the conditions of interest; natural convection from heated surfaces and channels. Similarly, focus is given to applications and methodologies pertaining to PIV measurements.

The chapter is arranged as per the table of contents aside and concludes with a summary of the main implications.

2.1 Natural convection from smooth surfaces

Natural convection from a vertical heated surface is a topic that has received extensive research over many decades. The literature has been reviewed many times; including dedicated books on the topic such as by Gebhart et al.[4] and chapters in more general heat transfer texts such as Holman[5], Incropera and DeWitt[6], Hewitt[7].

Given the broad scope of the literature it is necessary to limit interest to that which can aid in the design of apparatus and verification of the results. To do so one must consider the sort of thermal and flow conditions present within a reactor that would be replicated in a separate effect test (SET). Namely, a high heat flux is expected and the flow will likely be highly turbulent.

Typically isothermal and isoflux conditions are produced experimentally due to the relative ease of both approaches compared to some prescribed geometric variation in temperature or heat flux over the heater surface. For isothermal conditions a separate circulating heater system is typically used to continually supply coolant to the isothermal surface thereby ensuring a constant temperature. Whereas for an isoflux condition one might employ an electrical heater with uniform

heat flux density as achievable by resistive heaters.

Regarding the flow condition, unlike forced convection where a critical Reynolds number can be used to define the onset of transition to turbulence, there is no direct parallel for natural convection. Partly, this is because no single characteristic group has been identified to sufficiently describe all types of natural convection flows and thermal boundary conditions. However, the most similar dimensionless group used to indicate turbulence is the so-called *Rayleigh* number Ra, or a modification thereof.

The Rayleigh number is typically[5,6] derived for flows with an isothermal boundary condition and is defined here as

$$Ra = Gr.Pr = \frac{g\beta\theta_w\ell^3}{\alpha\nu} \tag{2.1}$$

where Gr is the Grashof number, Pr is the Prandtl number, g is the gravitational acceleration, β is the volumetric thermal expansion coefficient, $\theta_w = T - T_\infty$ is the wall excess temperature; the difference between the wall and quiescent temperatures T and T_∞, ℓ is a characteristic dimension e.g. for a surface the distance from the leading edge, α is the thermal diffusivity and ν is the momentum diffusivity or kinematic viscosity.

For isoflux conditions the Rayleigh is modified by the definition:

$$Gr^* = GrNu \tag{2.2}$$

where Nu is the Nusselt number and the superscript $*$ typically denotes a modified or isoflux condition. The Nusselt number is used to replace the a priori unknown excess wall temperature with a known heat flux as so:

$$Nu = \frac{h\ell}{k} = \frac{q''\ell}{\theta_w k} \tag{2.3}$$

where q" and k are the surface heat flux [W/m^2] and thermal conductivity [W/mK], respectively.

Hence the modified Rayleigh number can thus be written as:

$$Ra^* = Gr^*.Pr = \frac{g\beta q"\ell^4}{k\alpha\nu} \tag{2.4}$$

Historically, similar dimensionless groups have also been defined which are modifications of the above. It may be seen that these are further modification of the basic Rayleigh number. In a similar fashion the dimensionless groups to be defined in channel flows are also modified versions of the above.

Whilst no single modified Rayleigh number quantifies the transition to turbulence, most fluids are expected to transition in the vicinity of $Ra_x^* \approx 1 \times 10^{10} \rightarrow 10^{11}$ with suppression or advancement occurring as a result of many contributing factors beyond heat flux. Here the subscript x refers to the distance from the leading edge of the heating surface.

Oosthuizen and Kalendar[8] describes the influence of dimensionless width on the three dimensionality of the flow about isothermal and isoflux heated surfaces. Whilst only open edges are investigated by the authors, it is assumed that similar behaviour could be expected for enclosed edges albeit with a different phenomenological behaviour due to increased wall friction. Hence the recommendations of the authors should be treated as liberal since they do not account for the assumed increased three dimensionality due to increased wall friction on the enclosed sides.

The authors state that heat transfer from sufficiently narrow plates is improved due to out-of-plane motion. This is evidenced by a deviation in the typical trend of Nu to Ra^* for increasingly narrow plates.

The authors introduce an aspect ratio, or as they refer to it a dimensionless width, W defined as $W = w/L$ where w is the heater width and L the height. Based on computational results for $10^4 \leq Ra^* \leq 10^8$ they derive an empirical correlation (2.5) to quantify where three dimensionality of the flow may be assumed negligible.

$$W \geq \frac{15.2}{(Ra^*)^{0.2}} \tag{2.5}$$

3D effects are assumed to occur when the relationship between Nu and Ra^* for a narrow plate deviates from the existing correlations for wide plates by $\geq 2\%$.

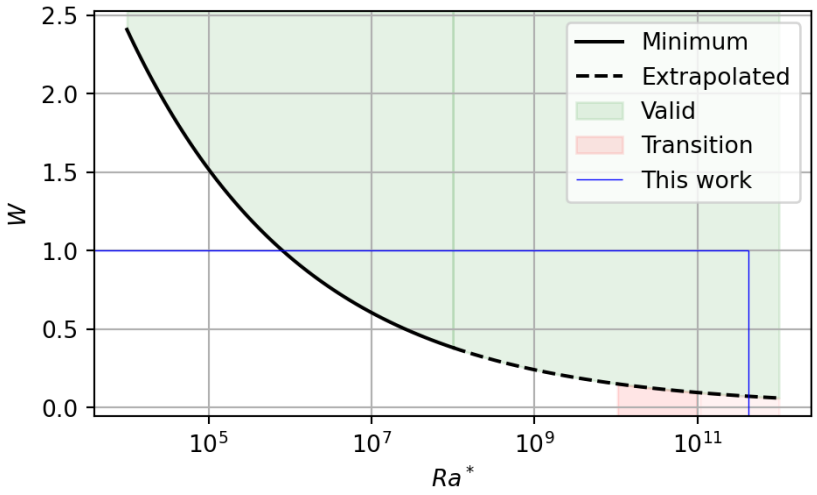

Figure 2.1: Plot of the minimum dimensionless width W required to yield a pseudo 2D flow from a vertical isoflux surface as a function of Ra^* as given by (2.5). Pseudo 2D assumption valid in the shaded region above the curve. The dashed line represents extrapolating the results beyond the reported limits.

Equation (2.5) is plotted in Figure 2.1 from which it may be seen that as the flow approaches turbulence (transition is shaded orange) the minimum dimensionless width becomes smaller and thus the surface can be narrower.

It may be seen that the correlation of Oosthuizen and Kalendar[8] covers only the laminar range and increased three dimensionality is to be expected as the flow transitions to turbulence. In a later publication[9] the author states that for problems of practical engineering interest involving

turbulent flows, side effects will be negligible due to the relative thickness of the boundary layer and the surface width. Care must taken when interpreting this statement since the boundary layer thickness is expected to increase as turbulence is encountered in addition to the local production of out-of-plane motion. Thus, this statement is instead interpreted as: Where turbulence is encountered the out-of-plane motion introduced via side effect becomes negligible with respect to that introduced by turbulence directly. Conversely this does not state that a turbulent flow is 2D.

In addition to local heat transfer; quantified by Nu_x, many early works[10] were concerned with the determination of surface averaged conditions. These works sought to determine an average Nusselt number $\overline{Nu}_L$ such that the average surface temperature may be calculated. The subscript L refers to the use of the entire surface length as the characteristic length in the definition of the Nusselt number i.e.

$$\overline{Nu}_L = \frac{\overline{h}L}{k} \tag{2.6}$$

Since the average convective heat transfer coefficient $\overline{h}$ is unknown a priori, correlations using the modified Rayleigh number, or a variant, were published in the form[10]:

$$\overline{Nu}_L = f(Pr)g(Ra^*_L) \tag{2.7}$$

where $f()$ and $g()$ are empirical functions. Note that the Rayleigh number also has a subscript L and like $\overline{Nu}_L$ uses the entire plate length as the characteristic length.

Similarly, correlations are also proposed for local heat transfer in the form

$$Nu_x = f(Pr)g(Ra^*_x) \tag{2.8}$$

The origin and form of these correlations is dependent upon the thermal boundary condition and whether the flow is laminar, transitioning or turbulent. In the case of laminar flow, correlations may be determined analytically by simplifying assumptions. However, for turbulent flow such analysis is not possible and empirical correlations are typically based upon experimental measurements.

2.1.1 Laminar flow

For laminar flow from an isoflux vertical heated surface, Sparrow and Gregg[11] produced an analytical solution for velocity and temperature distributions using the similarity method introduced by Pohlhausen[12] and the boundary conditions employed by Schmidt and Beckmann[13]. From this the temperature and velocity profiles, and the local heat transfer coefficients, were calculated for Prandtl numbers of different orders of magnitude encompassing, but not accurately matching, that of water at atmospheric conditions for which $Pr \approx 7$.

Sparrow and Gregg[11] compared their results to the similar earlier analytical work of Ostrach[14] on laminar isothermal surfaces. They found good agreement could be achieved for surface averaged, rather than local, conditions. This was an important finding as it meant that correlations developed from isoflux experiments could be applied to isothermal scenarios. They found excellent agreement could be achieved if an appropriate choice of wall excess temperature was used in the definition of the isothermal correlation.

For local heat transfer the authors again compared to the results of Ostrach[14] to demonstrate that isoflux surfaces tended to have slightly improved heat transfer performance over isothermal. The difference was of the order $\frac{Nu_{x,q''}}{Nu_{x,T}} = 12\% \rightarrow 15\%$ as $Pr = 100 \rightarrow 0.1$. The reason for the improved heat transfer performance is that in the case of an isothermal surface the wall excess temperature reduces with x resulting in reduced buoyancy downstream and thus impeding flow upstream. Such a degradation is not experienced with an isoflux surface.

Despite the difference in downstream conditions the two cases yield similar results. Due to the similarity many analytical and computation studies preferred isothermal conditions whilst experimentalists would continue to produce both isoflux and isothermal results. Much of this early work described above is summarised well by Ede[10].

The analytical approach used by Sparrow and Gregg[11] came to be known as the Kármán-Pohlhausen approximation method, as coined by the authors. This method uses the similarity solutions introduced by Pohlhausen[12] but ascribes quadratic functions to the temperature and velocity profiles allowing for solution without the aid of a computer. The form of the quadratic functions is determined by application of the similarity boundary conditions which yields velocity and temperature profiles.

The method is demonstrated in Holman[5] and the temperature profile has a profile defined by

$$\frac{T - T_\infty}{T_w - T_\infty} = \left(1 - \frac{y}{\delta}\right)^2 \tag{2.9}$$

where T is the temperature at any location x, y with the dependence on y being apparent. The x dependence lies within δ which is the boundary layer thickness and is a function of x.

Similarly the velocity profile is given by

$$\frac{u}{u_x} = \frac{y}{\delta}\left(1 - \frac{y}{\delta}\right)^2 \tag{2.10}$$

where u_x is a fictitious velocity which essentially performs the function of allowing the velocity profile to be scaled by the fluid properties and the x position is again scaled by δ.

Both profiles are illustrated in Figure 2.2. It may be seen that the temperature profile is similar to that found for forced convection. However, the velocity profile is quite different and can be seen to vary from zero at the surface $y/\delta = 0$, to a maxima at $y/\delta = 1/3$ and back to zero at $y/\delta = 1$.

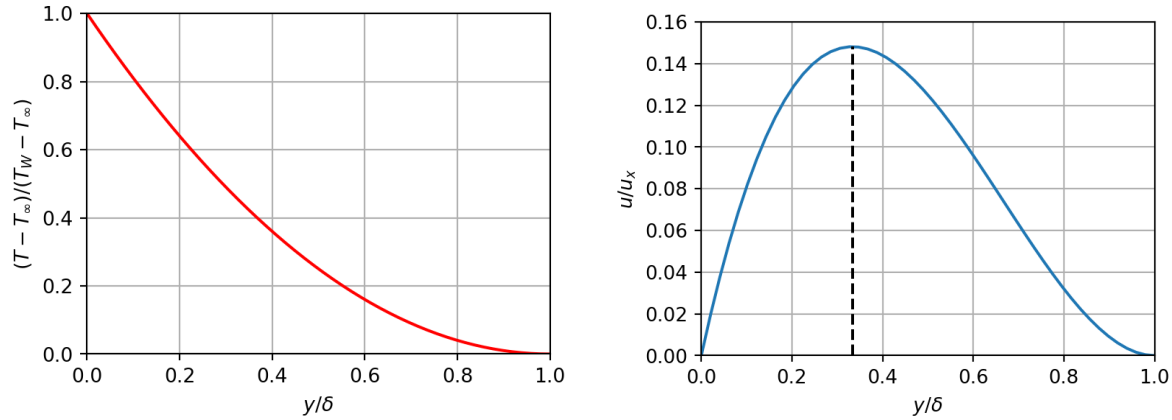

(a) (b)

Figure 2.2: Analytically derived dimensionless laminar temperature (a) and velocity (b) profiles as defined by eqn (2.9) and eqn (2.10), respectively.

The boundary layer thickness can be expressed as[5]

$$\frac{\delta}{x} = 3.93 Pr^{-1/2}(0.952 + Pr)^{1/4} Gr_x^{-1/4} \tag{2.11}$$

and the fictitious velocity by

$$u_x \frac{x}{\nu} = 5.17(0.952 + Pr)^{-1/2} Gr_x^{1/2} \tag{2.12}$$

It may be seen that with a knowledge of the Pr and Gr_x (the isothermal Grashof number $Gr_x = Ra_x/Pr$) one may determine the temperature and velocity profile at any location whilst the flow remains laminar. Thus to apply the preceding equations to an isoflux surface it is necessary to estimate an appropriate Gr_x which cannot be determined a priori due to the requirement to specify the wall excess temperature. To do so one may make use of the relation between Gr_x and Gr_x^* as introduced in eqn (2.2). This may be expanded as follows:

$$\begin{aligned} Gr_x Pr &= Ra_x \\ Ra_x &= \frac{Ra_x^*}{Nu_x} \\ \frac{Ra_x^*}{Nu_x} &= \frac{g\beta q'' x^4}{k\alpha\nu} \frac{\theta_x k}{q'' x} \\ \therefore \theta_x &= \frac{Ra_x^*}{Nu_x} \frac{\alpha\nu}{g\beta x^4} \end{aligned} \tag{2.13}$$

$$Gr_x = \frac{g\beta\theta_x x^3}{\alpha\nu} \tag{2.14}$$

Thus, to estimate θ_x a knowledge of Nu_x is required. A suitable correlation can be used for this purpose. However, it must be noted that the Kármán-Pohlhausen approximation method is only appropriate for application to the laminar boundary layer and thus any correlation used should also be equally applicable.

Holman[5] summarises the water-based isoflux experimental results of Vliet[15] and for laminar flow they recommend

$$Nu_x = \frac{hx}{k} = 0.60(Ra_x^*)^{1/5} \tag{2.15}$$

where Nu_x is the local Nusselt number and the characteristic length is distance from the leading edge of the heater x. The correlation is valid for $10^5 < Ra_x^* < 10^{11}$. This range falls short of covering the entire laminar region with transition reported[5] occur between $3 \times 10^{12} < Ra^* < 4 \times 10^{13}$. Fully developed turbulent flow is to be expected for values exceeding $Ra^* > 2 \times 10^{13}$. However, the exact value for transition to turbulence is not known, with authors suggesting various values and criterion (e.g. G^*) to indicate the start and end of transition which will be described in a later section.

In the turbulent region Holman[5] reports the correlation

$$Nu_x = 0.17(Ra_x^*)^{1/4} \tag{2.16}$$

for $2 \times 10^{13} < Ra^* < 10^{16}$. Thus, between $10^{11} < Ra^* < 2 \times 10^{13}$ no correlation is provided.

Holman[5] shows an average Nusselt number correlation provided by Churchill and Chu[16]

$$\overline{Nu}_L^{1/4}/(\overline{Nu}_L - 0.68) = \frac{0.67(Ra_L^*)^{1/4}}{[1 + (0.492/Pr)^{9/16}]^{4/9}} \tag{2.17}$$

For comparison Churchill[17], in the heat exchanger design handbook[7], proposes similar correlations where the Prandtl number effect is described separately by

$$\psi(Pr) = \left[1 + \left(\frac{0.437}{Pr}\right)^{9/16}\right]^{-16/9} \tag{2.18}$$

For laminar the local Nusselt number correlation is

$$Nu_x = 0.631(Ra_x^* \psi(Pr))^{1/5} \tag{2.19}$$

and the average Nusselt number is

$$\overline{Nu}_L = 0.726(Ra_L^* \psi(Pr))^{1/5} \tag{2.20}$$

This can alternatively be expressed in terms of an isothermal Rayleigh number[11]

$$\overline{Nu}_{L,L/2} = 0.670(Ra_{L,L/2} \psi(Pr))^{1/4} \tag{2.21}$$

where $\overline{Nu}_{L,L/2}$ and $Ra_{L,L/2}$ use L as the characteristic length but the wall excess temperature at the mid height.

For turbulent conditions the local Nusselt number is

$$Nu_x = 0.241(Ra_x^* \psi(Pr))^{1/4} \tag{2.22}$$

No range of applicability is provided by Churchill [17], except to say they apply to laminar or turbulent conditions. Equation (2.21) is compared by the author to the water data of Fujii and Imura [18] with reasonable agreement, but poor agreement for air.

2.1.2 Transition and turbulence

As the thermal transition begins the time averaged temperature profile varies from that shown for laminar flow in Figure 2.2. The gradient near the wall becomes steeper and away from the surface becomes shallower i.e. the profile has a greater kurtosis which results in a larger thermal boundary layer overall. As the level of turbulence increases so too does the kurtosis. This is shown in Figure 2.3 which is extracted from the experimental work by Godaux and Gebhart [19].

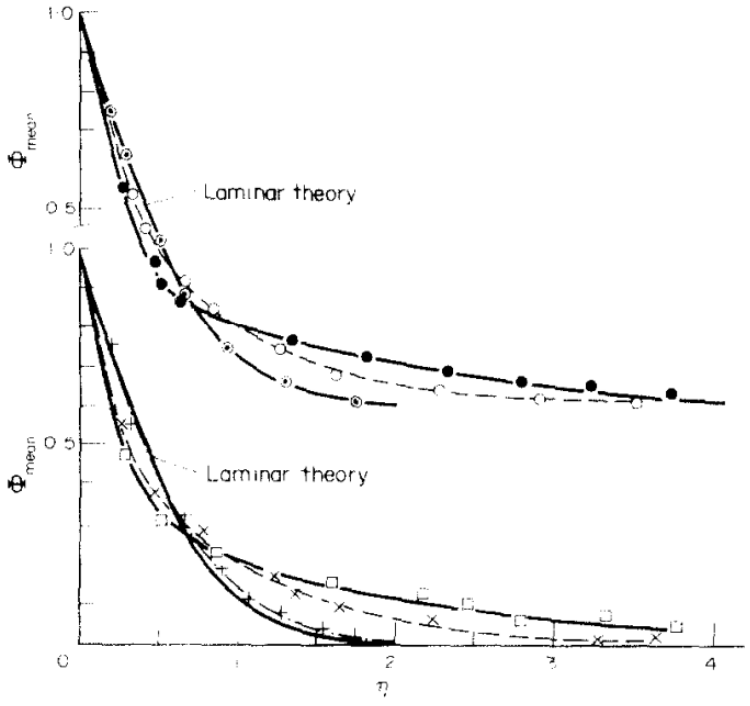

Mean temperature distributions.

Data:

	x (cm)	G*	Γ(η = 2·5)		x (cm)	G*	Γ(η = 2·5)
★	36·2	485	0	+	100	948	0·05
○	36·2	608	0·18	×	100	1031	0·6
●	36·2	625	0·68	□	100	1131	0·9

Figure 2.3: From Godaux and Gebhart [19] temperature profiles during turbulent transition ($\Phi = T - T_\infty / T_w - T_\infty$) and $\eta = \frac{yG^*}{5x}$ is a similarity variable

Figure 2.3 shows the temperature profile at two locations x and a variety of G^* values by varying q''. It can be seen that good agreement with the laminar theory is apparent for values $G^* = 485$

at $x = 36.2\,\text{cm}$ and $G^* = 948$ at $x = 100\,\text{cm}$. However, at other values of G^* the profile alters, adopting that of a turbulent profile. They further emphasise this with a thermal transition factor Γ which is related to instantaneous fluctuations in the temperature profile. The result is compelling and evidences the authors' suggestion that transition is not solely a function of G^*, or any other established grouping i.e. Gr^*.

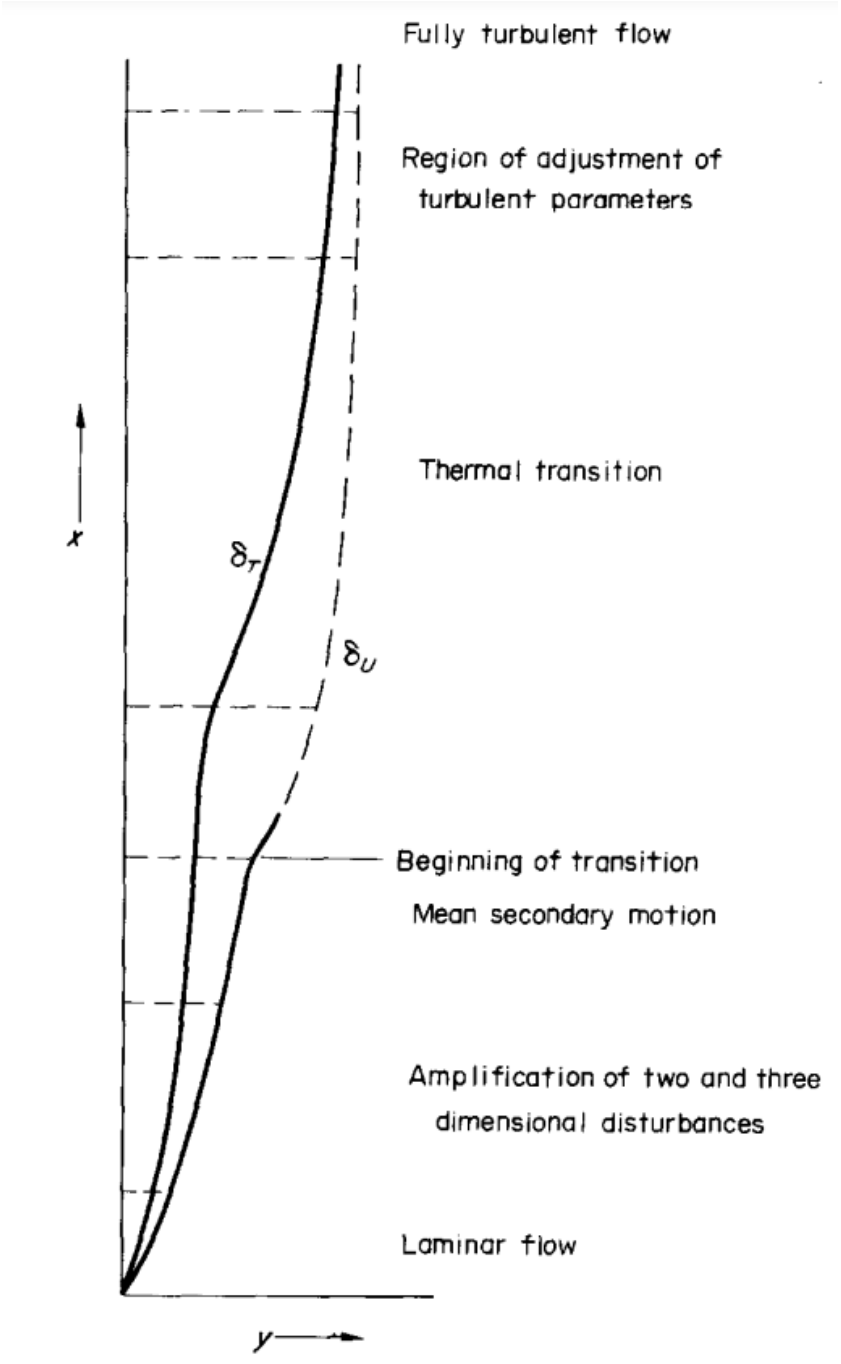

Figure 2.4: From Godaux and Gebhart[19] Mechanism of turbulent transition in water

According to Godaux and Gebhart[19] the transition to turbulence for a vertical isoflux heated surface in water occurs as shown in Figure 2.4. They demonstrate that at the beginning of transition the hydrodynamic boundary layer thickness increases and out-of-plane motion (aka secondary motion) is observed. At this location the level of turbulence within the thermal boundary layer also

increases but without an observable increase in the thermal boundary layer thickness.

The authors postulate that during the thermal transition, turbulent eddies are initially present at the outer edge of the thermal boundary layer due to the different thicknesses in hydrodynamic and thermal boundary layers as a result of the Prandtl number for water being $Pr \approx 7$. Thus the hydrodynamic boundary layer is significantly thicker than the thermal; a facet that distinguishes water based flows from other fluids. They suggest that this initially causes minor disturbance to the thermal boundary layer and it isn't until further downstream that larger, deeper reaching eddies are able to drive the transition of the thermal boundary layer. Hence the presence of a delayed thermal transition.

Using their own and others' data, they suggest that the start and end of thermal transition may be characterised by

$$Q(x) = q'' x \tag{2.23}$$

where $Q(x)$ is the convected thermal energy.

They suggest thermal transition begins at $Q(x) \approx 370\,\mathrm{W/m}$ and ends at $Q(x) \approx 650\,\mathrm{W/m}$.

The experimental apparatus used by Godaux and Gebhart [19] is relatively large ($L = 1.3\,\mathrm{m}$ and $w = 0.504\,\mathrm{m}$) with a heat flux range of $320\,\mathrm{W/m^2} \leq q'' \leq 1800\,\mathrm{W/m^2}$. The apparatus could produce a maximum of $Ra_x^* \approx 7.29 \times 10^{11}, 4.25 \times 10^{13}$ at the measurement locations $x = 36.2\,\mathrm{cm}, 100\,\mathrm{cm}$, respectively. Since both measurement locations demonstrated a transition to turbulence, and because the lower measurement position achieved conditions similar to that in the present work, it is reasonable to assume that a transition to turbulence will occur.

Jaluria and Gebhart [20] performed a follow on work of Godaux and Gebhart [19] and reported velocity measurements in addition to temperature measurements which they used to redefine the limits of transition proposed by Godaux and Gebhart [19]. They propose the onset of transition can be defined by:

$$E = G^* \left(\frac{\nu^2}{g x^3} \right)^{\frac{2}{15}} \tag{2.24}$$

where G^* is a function of the Grashof number defined by:

$$G^* = 5(\tfrac{1}{5} Gr_x^*)^{\frac{1}{5}} \tag{2.25}$$

For water they propose the onset of transition occurs at $E = 13.6$ and that thermal transition occurs at $E = 15.2$. The end of transition was considered by Mahajan and Gebhart [21] who proposed another method of defining the transition limits using:

$$Q_{ET} = Q B^{\frac{1}{30}} = 5^{4/5} (Ra^*)^{1/5} B^{1/6} = 11.4 \tag{2.26}$$

where $Q = (q''/g\mu)^{1/5}$ and $B = g x^3/\nu^2$. They propose a similar formulation for the beginning of transition. However, this simply converts the Q_{BT}, which defines the beginning of transition, back

to E as defined by eqn (2.24) through the introduction of a constant based on thermodynamic properties. The authors developed the correlation for use with gases and demonstrated it's use with air ($Pr = 0.7$). They also determine values of Q_{ET} for the water based experiments reported by Jaluria and Gebhart[20] ($Pr \approx 6.7$) and Vliet and Liu[22] ($5.05 \leq Pr \leq 6.4$). They found good agreement with the results of Jaluria and Gebhart[20] but less so with that of Vliet and Liu[22]. They posited this was due to a larger variation of thermal properties in the work by Vliet and Liu[22] who performed experiments at a wider range of Grashof number which resulted in a larger temperature difference between surface and quiescent region.

Figure 2.5 shows how the dimensionless velocity profile changes through the transition from laminar to turbulent flow. The profiles are plotted with respect to a similarity variable $\eta = \frac{yG^*}{5x}$ which serves to non dimensionalise the wall distance. It may be seen that as the flow transitions to turbulence the peak velocity occurs at the same $\eta \approx 0.8$ and the boundary layer thickness increases substantially.

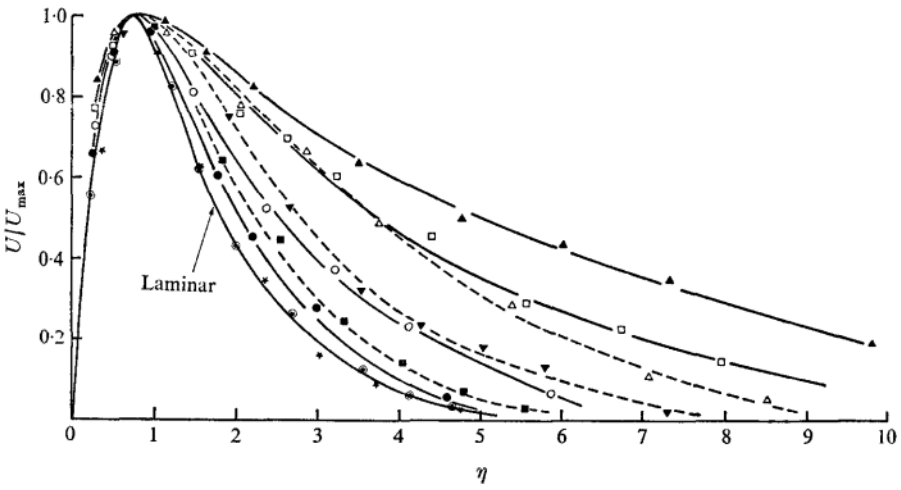

Mean velocity distribution. ——, x = 42 in.; ⊙, G^* = 752; ●, G^* = 838; ○, G^* = 914; □, G^* = 1240; ▲, G^* = 1342; – – – –, x = 15 in.; ★, G^* = 504; ■, G^* = 551; ▼, G^* = 586; △, G^* = 625.

Figure 2.5: From Jaluria and Gebhart[20]. Velocity profiles through the entirety of turbulent transition. U_{max} is the local maximum velocity and $\eta = \frac{yG^*}{5x}$ is a similarity variable.

The temperature profiles shown in Figure 2.3 may be compared to the velocity profiles in Figure 2.5. In doing so one should note a key observation; the laminar temperature boundary layer thickness is $\eta \approx 2$, which corresponds with the region of significant change during turbulent transition in the velocity profile.

In addition to changes in mean variables both Godaux and Gebhart[19] and Jaluria and Gebhart[20] investigate intermittent fluctuations about the mean profiles, as seen in Figure 2.6. These fluctuations are considered to play a significant role Joshi and Gebhart[23] in the transition to turbulence but can also provide insight in the required frequency and duration of a PIV measurement. They report the encountered frequencies at various x locations for all of which $0.1 \leq f < 1$ Hz.

The implication of these relatively low frequency fluctuations for PIV measurements is that the

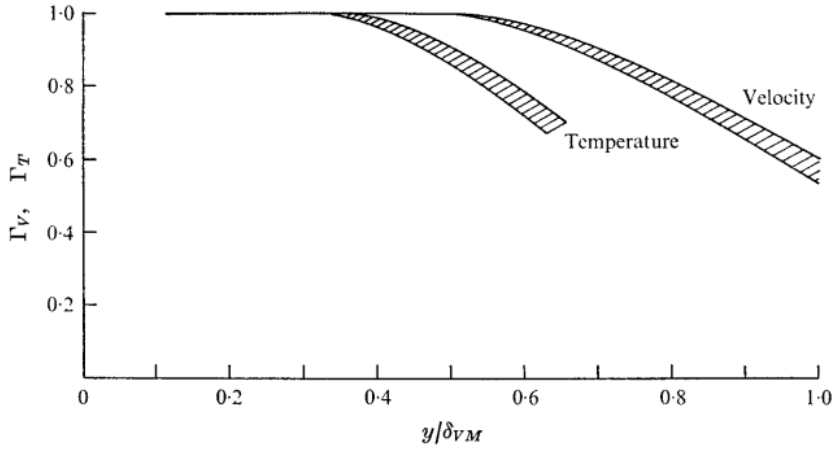

Distribution of the intermittency factors Γ_V and Γ_T across the boundary region at the end of transition for the downstream locations x where measurements were taken.

Figure 2.6: From Jaluria and Gebhart[20] disparity between the location of fluctuation in the thermal and hydrodynamic boundary layers ($Pr = 6.7$)

recording frequency is more constrained by flow velocity than oscillatory behaviour. However, the recording duration can be expected to be tens of seconds to suitably capture such fluctuations.

Also of significance is that Jaluria and Gebhart[20] reports the fluctuations of the hydrodynamic and thermal profiles differ during transition for a given G^*. This is important due to its implications on correcting distortion in PIV imagery. Since the relative thickness of the hydrodynamic and thermal boundary layers are a function of G^*, as are the respective fluctuations within these boundary layers, the optical distortion of PIV imagery will be dependent upon G^*.

For water, in the near wall region the imagery can be expected to be highly distorted. Little to no distortion is expected beyond the relatively thin thermal boundary layer, which corresponds with the outer reaches of the hydrodynamic boundary layer. This may be the reason why previous authors of publications of water-based experimental investigations have not mentioned refractive distortion; because the resolution of their works was not sufficient to observe the distortion of the relatively thin thermal boundary layer.

With regards to correction of the PIV imagery, it is clearly inappropriate to apply time averaged or asynchronous estimations of the refractive distortion due to the fluctuating nature of the flow and independence of fluctuations of the two boundary layers. This essentially demands the application of a simultaneous whole field measurement technique be used to correct for refractive distortion for water based natural convection experiments using PIV.

A final contribution from Jaluria and Gebhart[20] of interest is the relative magnitude of out-of-plane motion (z-direction) which they report to be very weak as compared to the velocity in the x-direction. Whilst a complete map of the out-of-plane motion was not provided this was due to difficulty measuring such a low velocity hence bolstering the suggestion that out-of-plane motion is relatively negligible. The authors comment on the presence of the vortical structures, one of which is out-of-plane. Such out-of-plane structures were later observed by Zhao et al.[24]. Of significance is the symmetry of the out-of-plane motion due to turbulence, where the plane of

symmetry is mid span of the heated surface as may be expected. Hence, it is desirable to measure a wall-normal plane at the midspan of the heating surface.

The implication of relatively low, symmetric, out-of-plane motion for PIV is that the majority of the flow features occur in a 2D plane. Thus, it is appropriate to use two dimension two component (2D2C) PIV. This is desirable for a simplified experimental setup but also for computation as it would be less computationally expensive and thus desirable as it enables quicker and easier verification and validation (V&V).

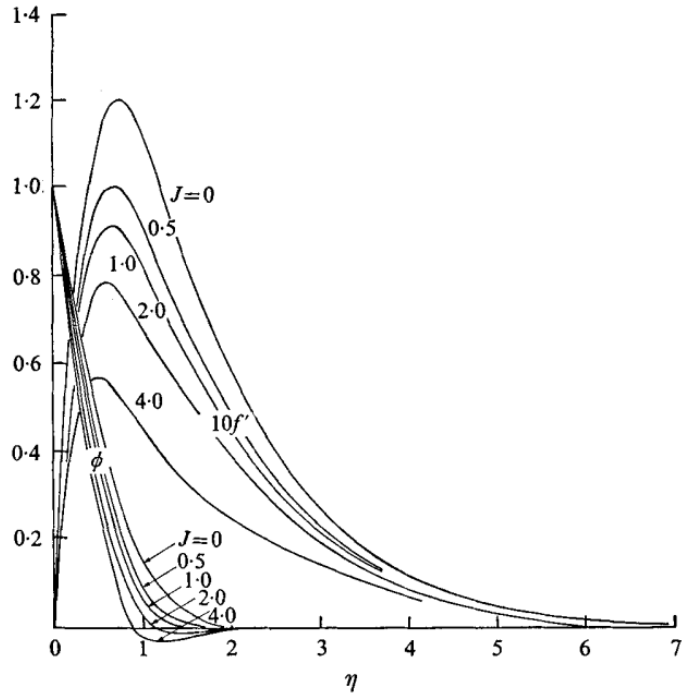

Figure 2.7: A plot of time averaged velocity profiles (f') and temperature profile (ϕ) for various amounts of stratification described by J. From Jaluria and Gebhart[25]

The effect of thermal stratification on transition to turbulence from an isoflux vertical surface was analytically and experimentally investigated by Jaluria and Gebhart[25] using water ($Pr \approx 6.7$). As in their earlier work[20] they used a similarity solution but included an additional term for the thermal stratification. The type of stratification considered was described by a power law relationship. The correlation constants from this relationship were used to define a stratification parameter J with $J = 0$ having no stratification and $J > 0$ being increasingly stratified. Figure 2.7 shows a plot of time averaged velocity for various amounts of stratification. The velocity is reported as a function of the stream function which can be converted back to a real velocity by:

$$u = U_c f'$$

where U_c is a reference velocity defined by

$$U_c = \frac{\nu G^2}{4x}$$

and

$$G = 4\left(\frac{g\beta(T_{wx} - T_{\infty x})x^3}{4\nu^2}\right)^{1/4}$$

In Figure 2.7 the wall-normal distance y is non-dimensionalised and replaced by the similarity variable η defined as:

$$\eta = \frac{y}{4x/G}$$

However, for an isoflux surface a slightly different definition of η is used given by:

$$\eta = \frac{y}{5x/G^*} \tag{2.27}$$

where y is the wall-normal distance, x the distance along the surface and G^* is defined by eqn (2.25). In practice both definitions of η yield almost identical values and can be used interchangably. The benefit of plotting data against such a variable is that it highlights features of non-similarity. Hence, if one were to plot a laminar velocity profile with the velocity non-dimensionalised (for example by dividing by the local peak velocity) against the similarity variable, all the profiles should collapse onto a single line. Whereas, flow features which result in non-similarity such as a transition to turbulence or the effect of stratification, result in a deviation from the similarity solution such as is shown in Figure 2.5 and Figure 2.7, respectively.

In addition the authors report that the presence of thermal stratification delays the transition to turbulence.

The presence of thermal stratification is known to sometimes result in the production of a flow reversal at the outer edge of the hydrodynamic boundary layer. This didn't occur in the experiments by Jaluria and Gebhart[25], and so doesn't not appear in the velocity profiles in Figure 2.7. However, another feature termed the *temperature deficit* is apparent[1]. In Figure 2.7 the time averaged temperature profile is given in dimensionless form by

$$\phi = \frac{T - T\infty x}{T_{wx} - T_{\infty x}} \tag{2.28}$$

where T_{wx} and $T_{\infty x}$ are the local wall and quiescent temperatures. Hence, a value of $\phi < 0$ suggests a local temperature that is less than the local quiescent. Since buoyancy is dependent on the difference in temperature this means the temperature deficit could either slow, stall or reverse the flow due to the production of a buoyant force opposite to that of the majority of the flow. Jaluria and Gebhart[25] posits that this is caused when the advection of cooler fluid is more rapid than the gradient of thermal stratification. The experimental results by Jaluria and Gebhart[20,25] do not yield a flow reversal region despite the presence of a temperature deficit. The authors comment the effect was too weak to yield a flow reversal, perhaps due to a lower heat flux or lesser thermal stratification, which is apparent in the comparison of results.

Tanny and Cohen[26] experimentally studied an isothermal surface in a linearly stratified water

[1] Whilst not recorded, evidence of a temperature deficit in the current apparatus has been observed when measuring the near wall region with a thermocouple.

medium in which the authors observed a temperature deficit. The authors only report temperature profiles for various levels of thermal stratification.

Paolucci and Zikoski[27] reports that Prandtl in Oswatitsch et al.[28] (in German) was the first to document a flow reversal region in the outer regions of the boundary layer for an isoflux surface in a linearly stratified quiescent medium.

Paolucci and Zikoski[27] demonstrates a method to solve all similarity solutions which account for various types of stratification i.e. linear, exponential etc. They provide plots of velocity and temperature profiles which show that a flow reversal is achievable for all types of stratification depending upon the level of temperature deficit. The plots they report are intended to demonstrate their technique making them unsuited to use for verification.

2.2 Technical challenges of investigating natural convection phenomena with PIV

A detailed description of PIV is given in Raffell et al.[29]. However to briefly summarise, PIV is an optical based technique where a working fluid is seeded with neutrally buoyant particles. These particles are illuminated and imaged by cameras which enables the velocity to be determined by comparing the displacement of particles between images.

Heat convection measurements present specific technical challenges to the application of PIV for a number of reasons:

1. **Greater restrictions on the choice of working fluid -**
   Seeding particles must be sufficiently large to be detectable by the imaging optics, but small enough that they do not influence the flow, provide a high resolution, and remain neutrally buoyant. In practice, certain working fluids are preferred as a suitable seeding material has already been identified and is commercially available. By this metric air and water are the most easily adopted fluids. However, the coupled nature of the hydrodynamic and thermal boundary layers in a natural convection problem introduces additional limitations on sizing the apparatus and what flow conditions are achievable with a given fluid.
2. **Loss of neutral buoyancy for seeding in the presence of a strong thermal gradient -**
   How faithfully the seeding particle follows the flow can be approximated by Stokes' law[29] to yield

$$\delta u = d_p^2 \frac{\rho_p - \rho}{18\mu} g \tag{2.29}$$

   where $\delta u, d_p, \rho_p, \rho, \mu$ and g are the velocity lag, particle diameter, particle density, fluid density, fluid viscosity and gravitational acceleration. As may be seen, ρ and μ are fluid properties and are thus temperature dependent. Thus, in the presence of a large thermal gradient these properties can be expected to vary and δu vary also. In practice this necessitates the use of very small diameter seeding particles in the range $1 \leq d_p \leq 20\,\mu$m for liquid

flows[29]. However, it is important to consider that as fluid velocity reduces, such as near to a heated surface with a no-slip boundary condition, the resulting δu may not be negligible. Furthermore, particles in a stationary fluid can be expected to gradually fall out of suspension presenting a difficulty in maintaining high seeding density in a low velocity flow over long durations.

3. **Refractive distortion of particle images in the presence of a strong thermal gradient -**
   High thermal gradients may be encountered near to a heated surface and are proportional to the heat flux. They may also be encountered where substantial fluid mixing occurs such that fluids of different temperatures are brought into contact. The refractive index of a fluid is a thermal property and varies with density, which in turn varies with temperature. Hence, in regions of large thermal gradient, for some fluids, a large change in refractive index may occur. For water this is particularly problematic and results in distortion and blurring of the particle image. If uncorrected this introduces a position and velocity error in the resulting data.
4. **Measurement near a surface -**
   Performing measurements near to a surface results in reflection of the light sheet which obscures the seeding particles from view. One method to overcome this is to used coated seeding particles which fluoresce in a different wavelength to the light source. In this way a suitable filter may be used to allow only the appropriate wavelengths through to the image sensor. A fluorescence signal is substantially less intense than a reflection which requires a brighter illumination.
5. **Selection of recording parameters -**
   Natural convection flows are by definition wall bounded and thus a large range of velocities are expected to be encountered. This was illustrated in Figure 2.2b. The challenge here is in selecting an appropriate Δt i.e. the time between subsequent images of the same particles. If this value is too high then the slow moving fluid may appear not to move or have sub-pixel displacement. Conversely, if this is too low then the fastest moving particles may travel too far between images. Both of these cases result in the introduction of error[29]. Thus, the larger the velocity gradients the larger the error introduced and the more difficult it is to define a suitable compromise for Δt. There are several methods to counter such problems, notably multi-pass post-processing algorithms[29] and adaptive window functions[30]. The latter of these defines the region or direction in which to search for a paired particle image.

In addition, there are general technical challenges for heat transfer experiments such as:

1. **Competing requirements for sizing of experimental apparatus -**
   Natural convection flows are typically characterised by some variation of the Rayleigh number (defined in section 2.1) which is highly sensitive to a characteristic dimension of the geometry. Thus, to achieve a turbulent flow (with a high Rayleigh number) one might consider a large experiment. A benefit of a larger experiment is increased resolution of the flow

features. However, the larger the experiment the larger the power supply required to heat the surface(s) which is typically a limiting consideration.

2. **Thermal losses (e.g. radiative and conductive) -**
   Air based experiments must account for heat loss due to thermal radiation as this is often comparable to the heat loss via convection, whereas liquid water readily attenuates thermal radiation thus negating this consideration. In both cases, due to the relatively low Nusselt numbers to be expected in natural convection, it is necessary to consider heat losses from the heat source. This typically involves additional instrumentation in the form of thermocouples and/or heat flux sensors.
3. **Thermal stratification of the surrounding fluid -**
   Motion is achieved in a thermo-convective buoyant flow due to the difference in temperature, and thus density, between fluid near to a surface and a surrounding bulk or quiescent fluid. In the case of heat transfer from a vertical heated surface to a cooler quiescent fluid, the effect of thermal stratification is to diminish the temperature difference between near-wall and quiescent fluid. Thus thermal stratification must be avoided by controlling the environment, or taking measurements quickly (and thus approximately adiabatically). However, this is generally not possible for pseudo-steady turbulent natural convection which requires extended periods of time to establish. In this case thermal stratification is unavoidable and must be minimised, measured and reported. A discussion of the effect of thermal stratification on a natural convection channel flow are given by Thebault et al.[31]. An example of correcting optical distortion from a thermally stratified fluid using BOS is reported by Verso and Liberzon[32]

PIV was the natural successor to particle based flow visualisation techniques which provided only qualitative measurement of the flow kinematics. Prior to PIV, quantitative measurement of velocity would typically be determined by anemometry; an intrusive technique whereby one or several small probes are inserted into the flow and unavoidably disturb the local flow condition. Around the same time that PIV was conceived another technique, laser doppler velocimetry (LDV), also gained popularity. LDV is an optical method that uses seeding particles; like PIV. However, LDV, like traditional anemometry, provided measurements at a single point. Since the LDV measurements occur at a single point the position error introduced by refraction could be calibrated when setting up the instrumentation and velocity error should be minimal so long as the measurement region was not substantially blurred. In contrast, the ability of PIV to both visualise and quantify a field, and later volume, provided greater insight into flow kinematics and popularised the technique through the 1970s and 80s with it being ubiquitous today for measurement of all manner of flows.

PIV has been applied to thermo-convective flows for several decades but in some earlier publications it was referred to as particle tracking velocimetry (PTV) or, more generally, as laser speckle velocimetry. Whilst PIV and PTV are distinct they are both types of laser speckle velocimetry with

broadly the same requirements [2].

The earliest publication describing a technique recognisable today as PIV is by Archbold and Ennos[33] in 1972 who described measuring displacement from a speckle pattern. In 1977 Barker and Fourney[34] demonstrated the application to a moving fluid. Only four months later PIV (or laser speckle velocimetry as it was known at that time) had been applied to a Rayleigh-Bénard convection cell by Simpkins and Dudderar[35].

The technique rapidly grew in popularity during the 1980s with many developments and applications. By the 1990s the technique had become digital, rather than the earlier analogue methods of doubly exposing a photosensitive film. This advancement made it possible to simultaneously apply PIV and thermometry techniques such as liquid crystal thermometry, an example of which is Dabiri and Gharib[36] who applied these techniques to a cavity flow.

2.2.1 Natural convection surfaces

Despite the interest in the geometry, there are very few examples of PIV being employed to measure natural convection from a smooth vertically heated plate. In order to estimate the required recording parameters a broader range of sources are consulted. The reported PIV recording details, where available or calculable, are summarised in Table 2.1.

There are some commonalities between all the reported works:

1. Air is the most commonly employed working fluid with only two examples using water as the working fluid which were performed by Zhao et al.[24,37].
2. The range of recording frequencies used but with the exception of Hattori et al.[38] these are < 15 HZ and of similar order of magnitude. This is significant since 15 Hz is the maximum frequency achievable with the laser illumination available.
3. The window size is most commonly 32×32 pixels.
4. With the exception of Sanvicente et al.[39] and Tkachenko et al.[40], the works are all performed with isothermal surfaces.

Notably, there are substantial variations in the duration of recordings (from 30 s to 12 min) and the fidelity of the results (scaling factors from 50 µm/px to 192 µm/px).

[2] The main difference is PTV requires a much lower seeding density than PIV and a different approach to processing. Otherwise the techniques are very similar.

Author	Fluid	Geometry	Condition(s)	FOV (Scale factor)	Window size	Freq.	Duration
Hattori[38]	Air	Surface	$Gr = 1.3 \times 10^8 \rightarrow 3.5 \times 10^{11}$	200 by 200 mm (50 µm/px)	20×20	30 Hz	900 images (30 s)
Zhao[37]	Water	Surface	$Ra = 9.3 \times 10^9$	140 by 110 mm (50 µm/px)	32×32	15 Hz	6300 images (7 min)
Zhao[24]	Water	Surface	$Ra = 9.8 \times 10^9$	160 by 200 mm (70 µm/px)	32×32	-	- (300 s)
Ayinde[41]	Air	Channel	$Ra = 2 \times 10^6 \rightarrow 8 \times 10^8$	62.5 by 10, 20, 40 mm (66 µm/px)	64×8	8 Hz	300 images (37.5 s)
Ayinde[42]	Air	Channel	$Ra = 1 \times 10^8, 2 \times 10^8$	62.5 by 10, 20, 40 mm (100 µm/px)	64×32	8 Hz	500 images (62.5 s)
Sanvicente[39,43]	Air	Channel	$Ra^*_d(d/H) = 3.5 \times 10^6$	200 by 200 mm (192 µm/px)	32×32	11 Hz	8000 images (12 min)
Tkachenko[40]	Air	Channel	None uniform heating	200 by 200 mm (192 µm/px)	32×32	11 Hz	8000 images (12 min)

Table 2.1: Reported PIV recording details from various literature sources concerned with thermo-convective flows

Whilst not stated by the authors, Hattori et al.[38] appears to be the earliest application of PIV to a vertical heated plate with combined forced and natural convection. The work was concerned with the transition to turbulence and the effect of an assistive free stream on this process. The aim of the work, like many others using PIV, was to gain deeper insight into the fundamental fluid motion and heat transfer processes rather than provide usable validation data.

Tsuji et al.[44] used PIV to gain greater insight into the effect of introducing a protrusion, for the purposes of heat transfer enhancement, within a turbulent natural convection boundary layer adjacent to a vertical isothermal heated surface. The experimental apparatus appears to be similar to that of Hattori et al.[38] (of the same research group) but without a forced free stream. Few details of the PIV recording parameters were reported, however the field of views were reported as 150×150 mm and 200×200 mm.

More recently, Zhao et al.[37] used planar PIV for the first time to investigate transition to turbulence for an isothermal surface in water and the same authors continued this work in a publication Zhao et al.[24] with two cameras to extend the field of view. They investigated a plane parallel, rather than the more common perpendicular, to the surface and offset by 10 mm. The maximum resulting flow velocities were of the order $O(\times 10^{-}4)$m/s and demonstrated fluctuation of less than 1 Hz with a peak around 0.31 Hz. They demonstrated a three stage evolution in the transition from start up to pseudo steady state over the duration of 350 s with the pseudo-steady state beginning after approximately 150 s. As the only example of PIV in a water based experiment it is interesting to note that there is no mention of blurring or distortion. However, this may be as a result of a relatively small temperature difference of $\Delta T \approx 10\,^{\circ}$C. Furthermore, the direction and location of the measurement plane may have made such distortions imperceptible.

Laein et al.[45] performed PIV on laminar flow for a vertical and horizontal isoflux (3 and 7 kW/m^2) surface using a nanofluid (suspension of TiO_3 with water as the base fluid). Of interest is the relatively high heat flux used in this publication $q'' = 3,7$ kW/m^2 which approaches the values used in the present study. However, the author provided little detail of the PIV recording parameters.

As commented by Laein et al.[45], there are relatively few examples of PIV being applied to heated surfaces with more attention being given to channel and cavity flows. To speculate, this is possibly due to a combination of greater engineering interest in such geometries, a large body of existing experimental measurements (using other techniques) for surfaces, and, a slight increase in difficulty to apply other whole field techniques, such as interferometry, to internal geometries. However, since the motivations to use one technique over another are typically not discussed in these publications it is impossible to know definitively why PIV has a relatively small application for natural convection surfaces.

2.2.2 Natural convection channels

The first application of PIV to channel geometry appears to be by Ayinde et al.[41] in 2006 which continued the earlier work of Habib et al.[46] who used LDV to perform flow visualisation of turbulent heat transfer from a natural convection channel. The working fluid in both cases was air and relatively small heaters of height 125 mm and width 200 mm were used with a separation of $b = 10, 20, 40$ mm. The measurement plane was observed at two positions with a scale factor of $SF = 66$ µm/px.

Sanvicente et al.[39] used PIV to investigate the turbulent transition of an asymmetrically heated isoflux channel. The authors conclude that there is a limited amount of experimental data relating to isoflux boundary conditions and that the transition to turbulence is difficult to measure due to the unsteady nature of the flow which they illustrate well.

A follow on study by Tkachenko et al.[40] performed a combined PIV and CFD study of the near wall flow for a non-uniform heating arrangement. A spectral analysis of the PIV data in both studies indicates a range of frequencies are present within the flow but typically less than 1 Hz.

Later Thebault et al.[31] used the same experiment to investigate the effects of thermal stratification of the surrounding fluid i.e. not in the channel, on the induced channel flow. They proposed a method to approximate the effect of stratification which agrees well with their data but not the LDV data of a water based experiment by Daverat et al.[47].

It may be seen that there are very few examples of PIV being applied to natural convection surfaces or channels and the majority of these use air as the working fluid and isothermal heating conditions. Beyond the uncertainty relating to the PIV calculation algorithm, no authors, besides Thebault et al.[31], consider additional contributions to uncertainty and no authors consider or mention refractive distortion. Where the boundary layer is not resolved this is understandable as the effects of refractive distortion may not be apparent. However, if one wishes to investigate increasingly turbulent natural convection flows, particularly to resolve the boundary layer kinematics, the limiting amount of power will require more authors to use water as the working fluid such that experiments may be smaller.

Thus, to complete the discussion of technical difficulties one must consider the literatures pertaining to the effect of refractive distortion on PIV results.

2.2.3 Refractive distortion as a source of uncertainty

In order to provide high fidelity, high confidence, experimental validation data from PIV measurements, some authors have investigated some of the major contributions to uncertainty specifically related to this scenario. These sources of uncertainty are summarised by Sciacchitano[48].

To produce a natural convection flow requires a heat source such as a heating surface. Thus, performing PIV measurements within the boundary layer necessitates these are made near to

the heating surface. Unless specifically coated, the heating surface reflects the light sheet with sufficient intensity to obscure the seeding particle images from the camera. A good early example of this are the flow visualisation experiments of Joshi and Gebhart[23,49]. In those experiments natural convection of water with a seeding particle was illuminated by a laser light sheet next to a 1.27 m tall isoflux heated flat plate. The reported images clearly show signs of reflection in the heated surface. The images are also streaky due to a long exposure being used for visualisation. Whilst not conclusive, due to the original publication now only being accessible as a scanned document, there appears to be blurring and distortion of the apparent heater surface and a darker region in the immediate vicinity of the heating surface at higher heat flux. These observations are not discussed in the publication and the visualisations were only treated qualitatively, but this could represent early examples of the effects due to refraction in water based natural convection experiments.

Alahyari and Longmire[50] report that whilst refractive distortion is a well known problem for LDV, they were the first to successfully apply PIV to a variable density flow. They achieve this by using two liquid solutions, with differing density, that have approximately the same refractive index.

A variation of this technique was recently performed by Partridge et al.[51] who investigated the mixing of a stratified fluid within an inclined duct.

The technique used by Alahyari and Longmire[50] and Partridge et al.[51] appears successful in the respective applications. However, this is achieved by very carefully matching refractive indices of the fluids prior to measurement and thus would be impractical to implement for a continuous heat transfer problem such as natural convection.

The refractive index matching approach can be thought of as avoiding the problem. The alternative is to encounter, measure, and if necessary, correct for the refraction.

Elsinga et al.[52] considered the effect of refractive distortion on PIV measurements in air. In their case the source of refraction was due to compressibility in the wake of a shock-wave at supersonic flow conditions. They state that refractive distortion causes blurring and a position error in the particle images in regions of high refractive index gradient. When calculating the velocity from such images this will result in a velocity error due primarily to the contribution from position error, irrespective of the working fluid. The position and velocity error are illustrated in Figure 2.8.

In Figure 2.8a the so-called *disturbed* light trajectory can be seen to be curving as it passes through a region of variable refractive index. This results in the particle position appearing in the wrong location shown by a hollow circle on the PIV plane. The position error introduced is thus the distance on the PIV plane between the hollow and solid circles. Similarly for the velocity error, the light ray trajectories for the same particle imaged at different times are shown together. It may be seen in Figure 2.8b that the actual particle should move a distance of $V_P \Delta t$, however due to distortion the particle appears (at the wrong position) to move a distance of $V'_P \Delta t$.

The authors state that the effect of blur is to introduce an astigmatism in the particle image which

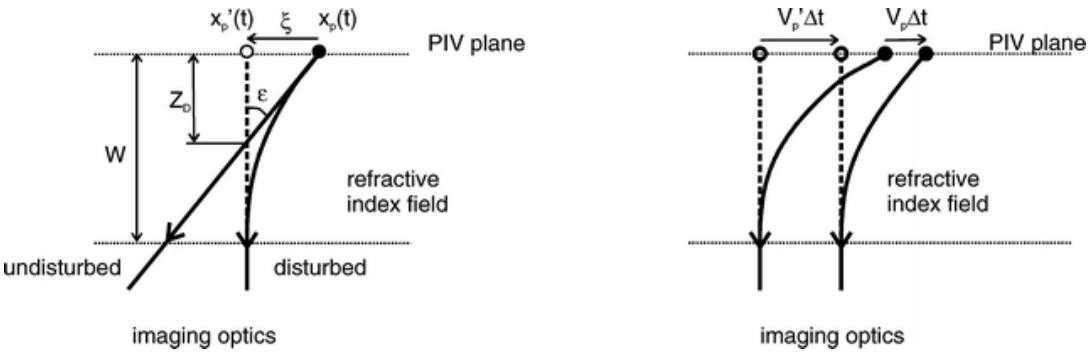

Figure 2.8: Illustration of the origin of the (a) position $(x'_P(t) - x_P(t))$ and (b) velocity $(V'_P - V_P)$ error. Solid lines represent actual light ray trajectory. Solid and hollow circles the actual and apparent position of a particle, respectively. From Elsinga et al.[52]

has a detrimental impact on the signal to noise ratio. Whilst developed for aero optical distortion these observations are equally valid for thermally induced refractive distortion in water. The authors propose a time averaged correction method that uses background orientated schlieren (BOS) to measure the distortion and correct the PIV results as a post process. This process was later used by Ihle et al.[53] to estimate, but not correct, the error due to distortion in their measurements.

Background orientated schlieren (BOS), originally proposed by Meier[54] and described in detail in Raffel[55], has a similar working principle to PIV. This may be achieved by observing a dot pattern, resembling a particle image, with and without distortion. Assuming the distortion is not sufficient to result in blurring, the resulting apparent shift of the dot pattern can be assessed in much the same way as PIV; cross-correlation and in fact a PIV solver is perfectly adequate in this task[56]. The calculated distortions are typically used to determine the density[57], temperature[53,56,58] and pressure, or in the case of Elsinga et al.[52] to correct the PIV measurements. Some authors have even recently extended the BOS technique for tomographic measurements[59–61].

The work of Elsinga et al.[52] is the inspiration for the BOS-correction approach developed in the present study which is described in greater detail in Chapter 4.

Of particular significance is the scaling of the refractive distortion from the PIV plane (which introduces the error in the measurement) to the BOS plane (where the distortion is measured), shown in Figure 2.9. For Elsinga et al.[52] a variable refractive index region was produced in the wake of a shockwave. Since light rays must travel a different distance through the region of variable refractive index the distortion at each plane will differ. To account for this, Elsinga et al.[52] introduced a so-called *scaling factor* (A) which was derived from optical equations for the light travelling from each plane. Through simplifying assumptions they proposed a scaling factor based on the physical separation of the two measurement planes.

$$A = \frac{W_{PIV}^2}{W_{BOS}^2} = 0.25 \tag{2.30}$$

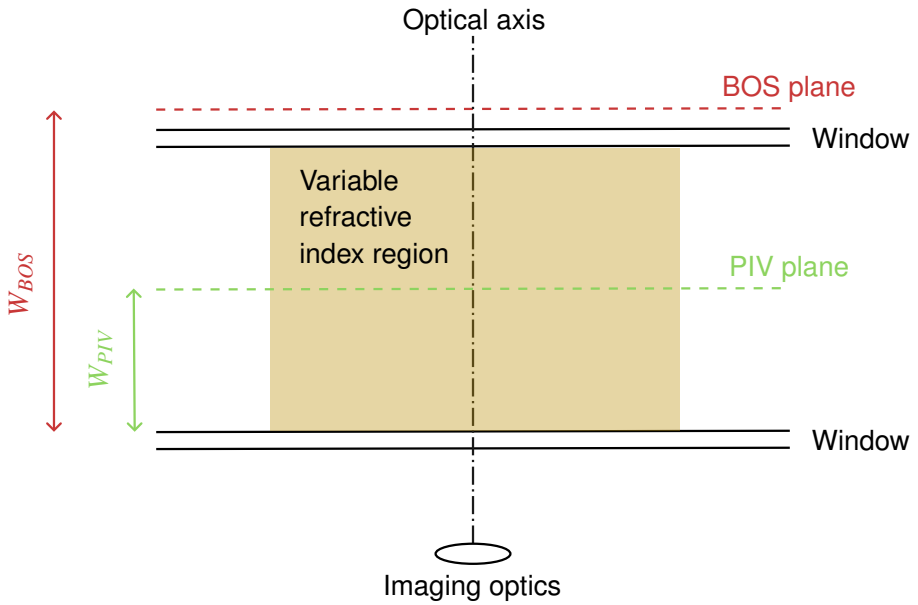

Figure 2.9: Schematic of the PIV, BOS and imaging planes, adapted from Elsinga et al.[52]

where W_{PIV} and W_{BOS} are the distance the light travels through the variable refractive index field. Referring to Figure 2.9, W_{BOS} is the distance across the test section along the optical axis, and W_{PIV} is located halfway across, hence the value of 0.25. The approach is simple and easily applied, however as will be shown later the assumption of a uniform scaling factor is not necessarily appropriate in all cases.

For a linearly stratified flow, Sveen and Dalziel[62] sequentially recorded BOS (referred to as synthetic schlieren) and PIV images on the same camera through the use of an alternating pattern on a monitor used to provide the dot pattern and illuminate the seeding particles for BOS and PIV, respectively. The advantage of such an approach is that a single camera may be used for both measurements which would be cheaper than using dedicated cameras for BOS and PIV imaging. This cost reduction would become most apparent were it extended to stereoscopic and tomographic measurements. However, the disadvantages are that seeding particles obscure the BOS pattern, the resolution is limited by that achievable by the monitor, the setup is limited to a scenario where both the BOS and PIV can be kept in focus, and, measurements are never truly simultaneous instead being limited by the refresh rate of the monitor.

Dalziel et al.[57] adopted the same alternating background approach of Sveen and Dalziel[62], but instead used dedicated cameras for BOS and PIV. The resulting density field, as determined from BOS measurements, was used as a post process to correct the PIV results, as in Elsinga et al.[52].

Ihle et al.[53] achieved simultaneous PIV and BOS measurements by implementing dedicated cameras and illumination for each technique. This enabled the use of a simple printed BOS target. A colour separation was achieved through the use of a filter on the PIV camera which was used to discriminate between the imaged dot pattern and seeding particles. Here the computed density fields from BOS were used to estimate the temperature field rather than correct for refractive

distortion. Ihle et al.[53] used the methods presented by Elsinga et al.[52] and Dalziel et al.[57] to estimate the error introduced by refractive distortion which were then considered negligible.

Tokgoz et al.[56] also achieved simultaneous measurements using dedicated equipment for PIV and BOS. Here a dichroic mirror is used to ensure both cameras use the same optical path which is at an angle to a reflective surface. This arrangement allows for a back illuminated BOS pattern to be reflected on the surface. However, deposition of seeding material onto the reflective surface posed a challenge to measurement and resulted in a lower seeding density to be adopted to avoid a loss in visibility. The authors found that using a separate camera to perform PIV and BOS measurements makes the error due to particle images in the BOS image negligible, due to these being out of focus. Thus, they demonstrated that if the distance between the PIV and BOS measurement planes is beyond the depth of field of the imagers used no special treatment is required, such as the colour separation of Ihle et al.[53]. The authors also used a PIV algorithm to process the BOS measurements rather than dedicated software. The computed density fields were used to estimate the temperature field and no correction of the PIV imagery was performed with the results being qualitative only.

More recently Rajendran et al.[63] developed a python based ray tracing computational tool to estimate refractive distortion for the purpose of experimental design and error analysis. The tool produces exemplary PIV and BOS images based on a user defined optical setup. The defined optical setup may include a density gradient but this must either be stationary, or applicable only at an instant. The ray tracing algorithm is reported to be computationally expensive and benefits from parallelisation.

It may be seen that BOS is receiving increased adoption and application as a companion technique to PIV. However, rarely has it been used to correct the refractive distortion of the PIV imagery with this typically being assumed negligible. Whilst for some experiments the effects of refractive distortion are negligible this is not the case for water based experiments where large density gradients are encountered, such as natural convection flows.

2.3 Summary

Optical measurement techniques such as PIV have been identified as key contributors of experimental validation data with increasing adoption in the study of natural convection flows. However, there have been relatively few PIV studies of water based natural convection.

The technical challenges of applying these techniques to water based natural convection problems has been discussed; with thermal stratification and refractive distortion receiving particular attention. BOS has been identified as a method to correct for refractive distortion but with very few examples of its use for this application within the literature.

A selection of the literature relating to natural convection from a vertically heated surface has been reviewed. A number of dimensionless groups have been introduced to describe the character of the flow. For transitional water natural convection flows, the hydrodynamic and thermal behaviour has been reported to fluctuate independently as distinct frequencies.

Some of the PIV recording parameters have been discussed with respect to expected experimental conditions and the dependence on factors such as thermal stratification.

However, there is a distinct lack of PIV measurements of natural convection flows, particularly for transitional or turbulent flow conditions. This is assumed to be due to the technical difficulties introduced by thermally induced refractive distortion. Hence, the work reported in this thesis is intended to address this technical challenge and enable the successful application of PIV to such flows.

Chapter 3

Apparatus

In this work the convective motion of water adjacent to a vertical plate heater is measured over a plane perpendicular to the surface and parallel to the flow. The plane, henceforth referred to as the *PIV plane*, is mid span of the heating surface as illustrated by a green line in sub-figure 3.1b. The PIV plane is named after the flow visualisation technique employed; particle image velocimetry (PIV) which is used to measure velocity. A further optical technique called background orientated schlieren (BOS) is employed to measure the thermally induced refractive distortion.

Figure 3.1 shows the position of the cameras with respect to the planes of interest. The beam splitter houses a dichroic mirror which allows both cameras to observe the same field of view via the same optical axis. Hence, the optical path between the beam splitter and the plane of interest is as follows:

1. **Beam splitter to reservoir wall** media: air
2. **Through reservoir wall** media: acrylic
3. **Inner reservoir wall to shroud** media: water
4. **Through shroud** media: acrylic
5. **Inner shroud wall to plane of interest** media: water. This is the fluid which has a large thermal gradient and thus causes the thermally induced refractive distortion.

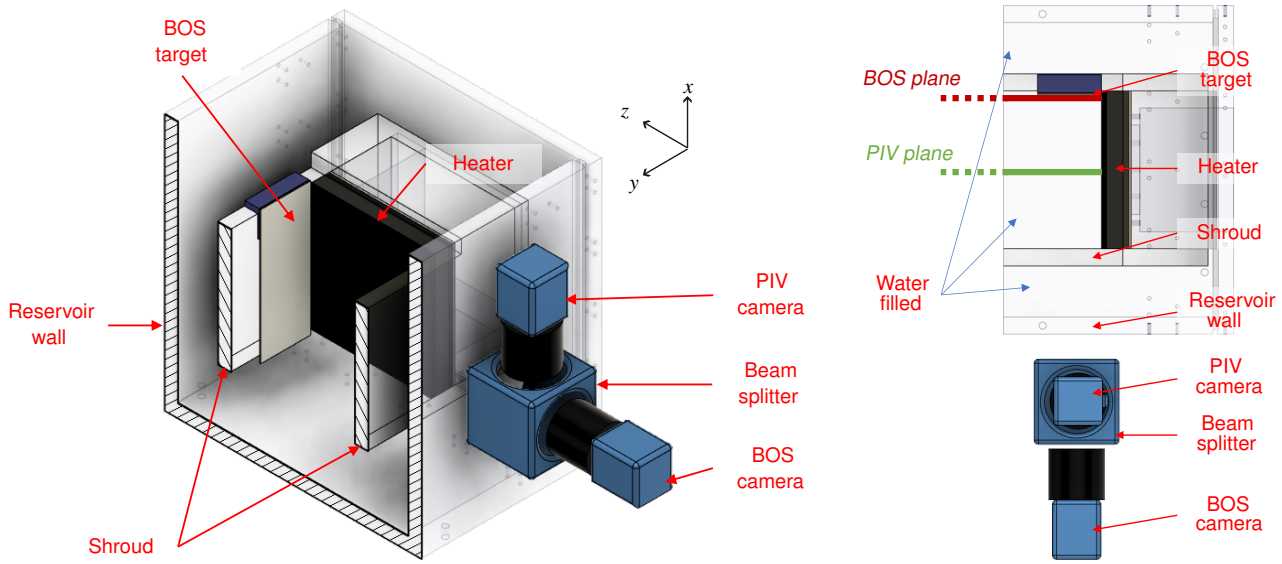

(a) (b)

Figure 3.1: Illustration of the optical measurement path; (a) perspective, (b) top-down.

3.1 Flow visualisation instrumentation

Particle image velocimetry (PIV) and background orientated schlieren (BOS) are well established flow visualisation techniques which are described in Raffell et al.[29] and Raffel[55], respectively.

The PIV instrumentation in this work is configured for a planar measurement i.e. only two components of velocity are measurable over a plane (the so-called PIV plane as seen in Figure 3.1). This arrangement is also called a 2D2C PIV measurement. The instrumentation and parameters of interest for PIV are detailed in Table 3.1 and Table 3.2, respectively. Similarly, the instrumentation and parameters of interest for BOS are detailed in Table 3.3 and Table 3.4, respectively.

A photograph of the experimental apparatus is shown in Figure 3.2. The apparatus consists of a water[1] filled reservoir with a heating surface, a target for BOS measurements. Some of the instrumentation may also be seen including a laser with light sheet optics[2], cameras and a beam splitter to repeat the same field of view on both cameras. The position of power supplies and the data acquisition device (labelled NI cDAQ) can also be seen.

The PIV measurement requires imaging the movement of seeding particles. The effects of thermally induced refractive distortion will cause the particles to appear in the wrong location which results in a velocity and position error. If the thermal field is time dependent, for example due to turbulence, the distortion of each image recorded will be unique. To account for this instantaneous distortion of the PIV images the BOS measurements must be performed simultaneously. These simultaneous measurements are referred to as PIV+BOS.

[1]The water appears pink in the photo as dye had been added to perform laser induced fluorescence (LIF) measurements which are not reported in this thesis.

[2]The laser optics is obscured from view. The light sheet is emitted from left to right

Table 3.1: PIV instrumentation

Component	Supplier	Model	Note(s)
Light source	Litron	PIVnano	Nd:YAG dual cavity 532 nm laser with -50 mm cylindrical lens
Camera	LaVision	sCMOS imager	-
Lens	Tokina	100 mm macro AT-X pro	-
Seeding particles	Micro particles GmbH	PS-RhB-FRAK	Rhodamine-B coated polystyrene spherical microparticles with nominal 20 µm diameter.

Table 3.2: PIV recording parameters

Parameter	Value	Note(s)
Field of view	50 mm $\times$ 60 mm	Later masked to ≈ 10 mm $\times$ 60 mm
Scaling factor	≈ 43 px/mm	
Laser pulse separation (dt)	0	Both cavities fire simultaneously
Camera mode	Single frame	
Recording frequency	15 Hz	
Exposure	30 µs	
Duration	5000 images	≈ 333.33 s
Interrogation window size	64×64 with 50% overlap	$\times 1$ initial pass
	64×64 with 75% overlap	$\times 1$ final pass
Interrogation window function	Adaptive	Default 4:1 elliptical shape function

Table 3.3: BOS instrumentation

Component	Supplier	Model	Note(s)
Light source	Travor	TR-60WS	60 W LED video light
Camera	LaVision	sCMOS imager	-
Lens	Tokina	100 mm macro AT-X pro	-
Target	-	-	Black on white random 0.1 mm dot pattern with 0.2 mm$spacing$

Table 3.4: BOS recording parameters

Parameter	Value	Note(s)
Field of view	50 mm $\times$ 60 mm	Later masked to ≈ 10 mm $\times$ 60 mm
Scaling factor	≈ 43 px/mm	
Camera mode	Single frame	
Recording frequency	15 Hz	
Exposure	5000 µs	
Duration	5000 images	≈ 333.33 s
Interrogation window size	64×64 with 50% overlap	$\times 1$ initial pass
	64×64 with 75% overlap	$\times 1$ final pass
Interrogation window function	Adaptive	Default 4:1 elliptical shape function

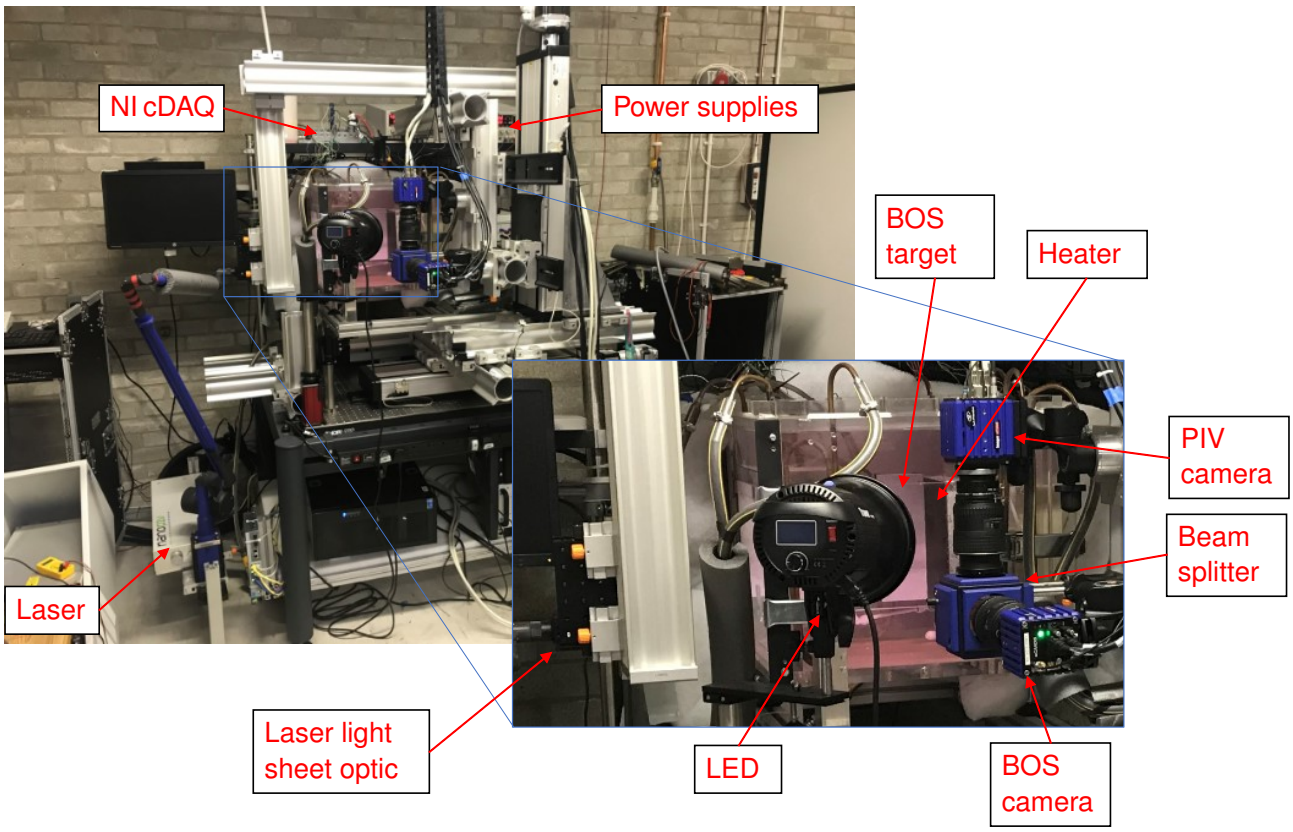

Figure 3.2: Photograph of the experimental apparatus

The BOS technique produces an integral measurement of distortion between the camera and a background target. To avoid disturbing the flow phenomena measured at the PIV plane the BOS target is located further from the camera i.e. in the background. This background plane is called the *BOS plane* and is illustrated by the red line on sub-figure 3.1b. Performing BOS at the BOS plane means the measurements also include the distortion contribution from the fluid between the PIV and BOS plane. In order to correct the distortion of the PIV images at the PIV plane the BOS measurements must be scaled to the BOS plane. In this work, for the first time, the appropriate scaling is determined experimentally. This is achieved through an additional round of BOS measurements with a target located at the PIV plane. Since the BOS technique is applied at the PIV and BOS planes the respective measurements are referred to as BOS@PIV and BOS@BOS to avoid confusion. The two BOS targets and mounting equipment are illustrated in Figure 3.3.

Limitations on the camera field of view required that imaging the entire length of the surface be conducted in four segments. For each segment the camera and light sheet were repeatably positioned by precision motorised linear translation stages. These positions are defined in Table 3.5. It may be seen that the field of view of adjacent positions overlap slightly. This overlap region is used for alignment between the measurement positions and requires calibration. This was achieved using a ruler which is aligned with the leading edge of the heater (illustrated in figure 3.4a and photographed in figure 3.4b). Images of the ruler are taken at each measurement position which could then be stitched together as seen in figure 3.4c. There was no transition or

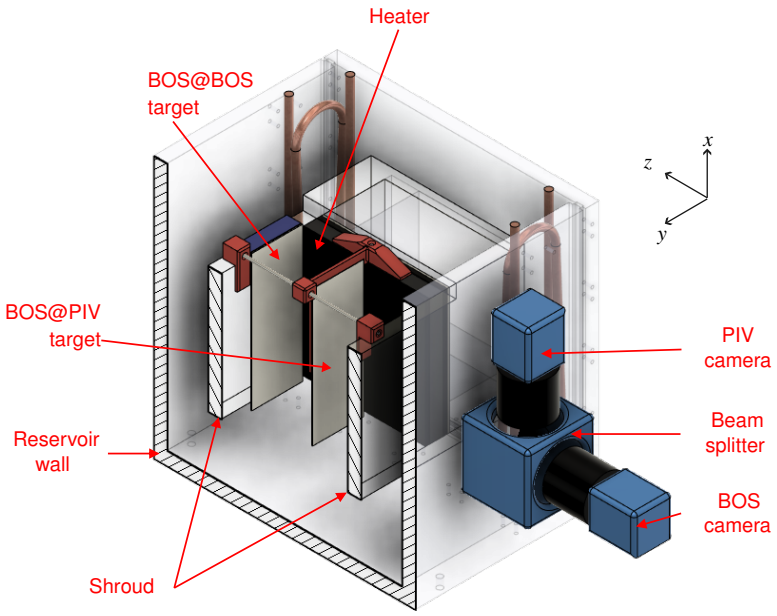

Figure 3.3: Background orientated schlieren (BOS) targets (white) with 3D printed rigid mounting for BOS plane (blue) and positioner for the PIV plane (red). (Colours for illustration only, the printed parts were black)

blending between fields of view. Rather, the choice of where one position begins and the other ends was later determined by comparing the time averaged velocity profiles. The resulting extent of each position is shown in 3.4d.

Table 3.5: Table of measurement positions (x is the distance from the leading edge of the heater)

Pos.	Instrumentation centred at	Viewable interval	Actual interval
4	$x \approx 170\,\text{mm}$	$140\,\text{mm} \leq x \leq 200\,\text{mm}$	$138\,\text{mm} \leq x \leq 187\,\text{mm}$
3	$x \approx 120\,\text{mm}$	$90\,\text{mm} \leq x \leq 150\,\text{mm}$	$88\,\text{mm} \leq x \leq 138\,\text{mm}$
2	$x \approx 70\,\text{mm}$	$40\,\text{mm} \leq x \leq 100\,\text{mm}$	$45\,\text{mm} \leq x \leq 88\,\text{mm}$
1	$x \approx 20\,\text{mm}$	$-10\,\text{mm} \leq x \leq 50\,\text{mm}$	$0\,\text{mm} \leq x \leq 45\,\text{mm}$

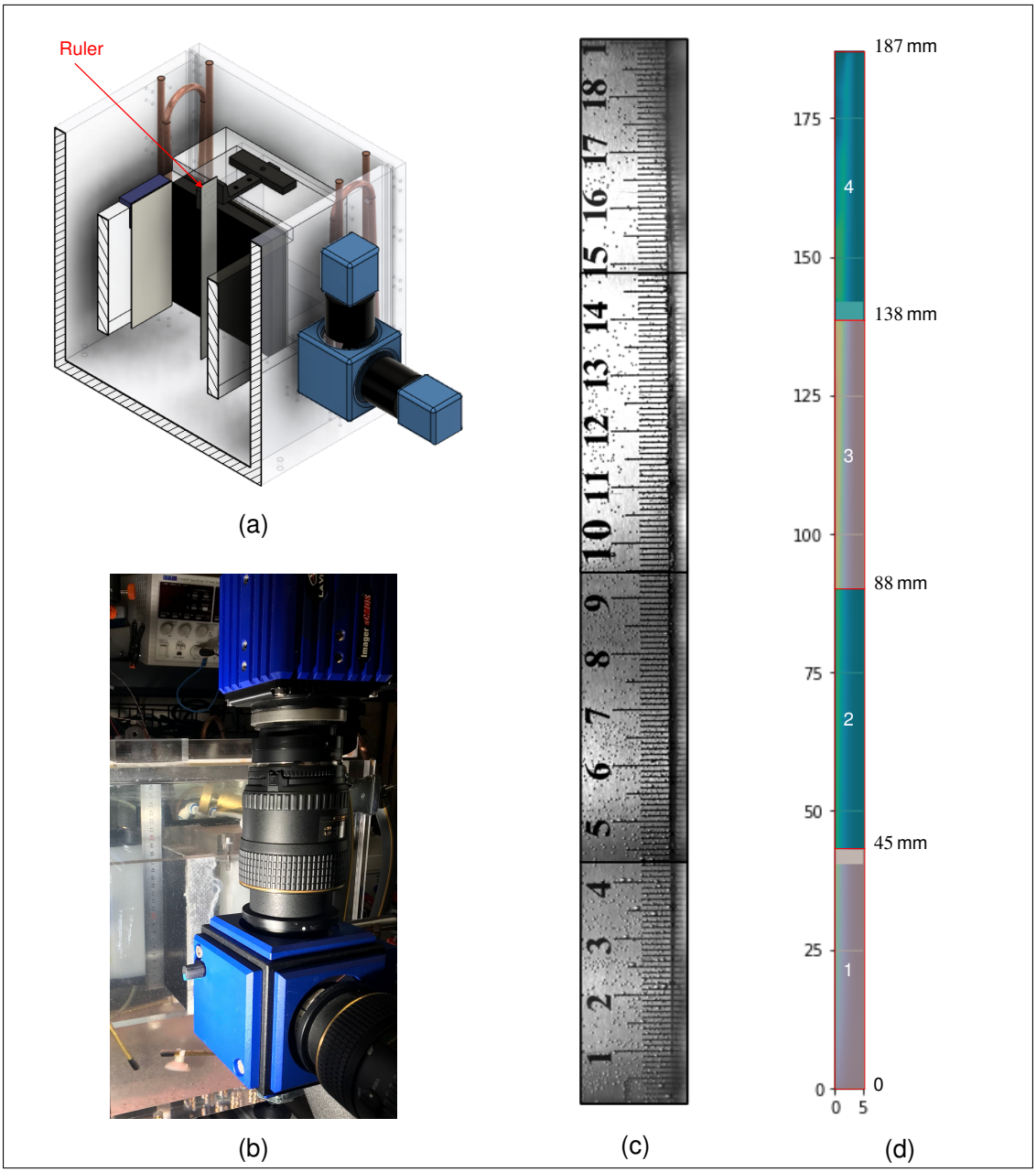

Figure 3.4: Method of locating imaged segments with a ruler (a) illustration, (b) photo, (c) composite image and (d) defined positions

3.2 Apparatus

3.2.1 Reservoir

An exploded view of the apparatus can be seen in Figure 3.5 and consists of a U-shaped section to which interchangeable side panels can be affixed. With side panels attached a reservoir is produced which can hold up to a maximum of ≈ 50 L of water, or other working fluid.

The design is different to other apparatus reported in literature (e.g. Sparrow and Azevedo[64] and Daverat et al.[47,65]) which tend to follow the approach of the seminal works by Elenbaas[66] who mounted heaters on threaded rods which could be positioned with shims. Suspending the heater from a single rod may lead to deflection and thus the production of a converging channel, or at least non-parallel, such was the case for Ayinde et al.[41] who introduced supports to the experimental design reported in later works[42].

The more complicated reservoir design is to enable optical measurements to be taken of the rear side of the heater, or through a transparent heater/surface. An illustration of this setup is shown in Figure 3.6. No measurements from this direction are reported in this work, this information is included only to provide context to the reservoir design.

To achieve this optical access the side panels (Figure 3.5b) include a raised platform and bolt hole pattern such that heaters (Figure 3.5c) and/or extension blocks (Figure 3.5d) may be mounted. To produce a closed channel geometry a shroud (Figure 3.5e) can be suspended between the side panels. In addition to the components shown, there are also blank side panels and a lid to reduce heat loss.

The apparatus was sized to produce pseudo-2D flows when configured as a channel or a single heated surface. This is achieved by ensuring the heating surface is sufficiently wide which is reported for a surface by Oosthuizen and Kalendar[8], Oosthuizen[9], and for a channel by Oosthuizen and Kalendar[8], Oosthuizen[9], Habib et al.[46].

3.2.2 Heaters

Square ($187\,\text{mm} \times 187\,\text{mm}$) plate heaters, similar to many of those found within the literature e.g. Daverat et al.[47,65], are used.

Figure 3.7 shows the plate heater construction. The faceplate is CNC machined from aluminium onto which two electrically heated, independently controlled, self-adhesive silicone coated foil heater pads are attached. The heater is attached to the rest of the apparatus via a high density polyethylene (HDPE) stand-off and machined aluminium rear plate. The internal void is filled with polyester Dacron insulation.

The aluminium faceplate is 4 mm thick and has 3 mm deep slots for thermocouples. Hence, the

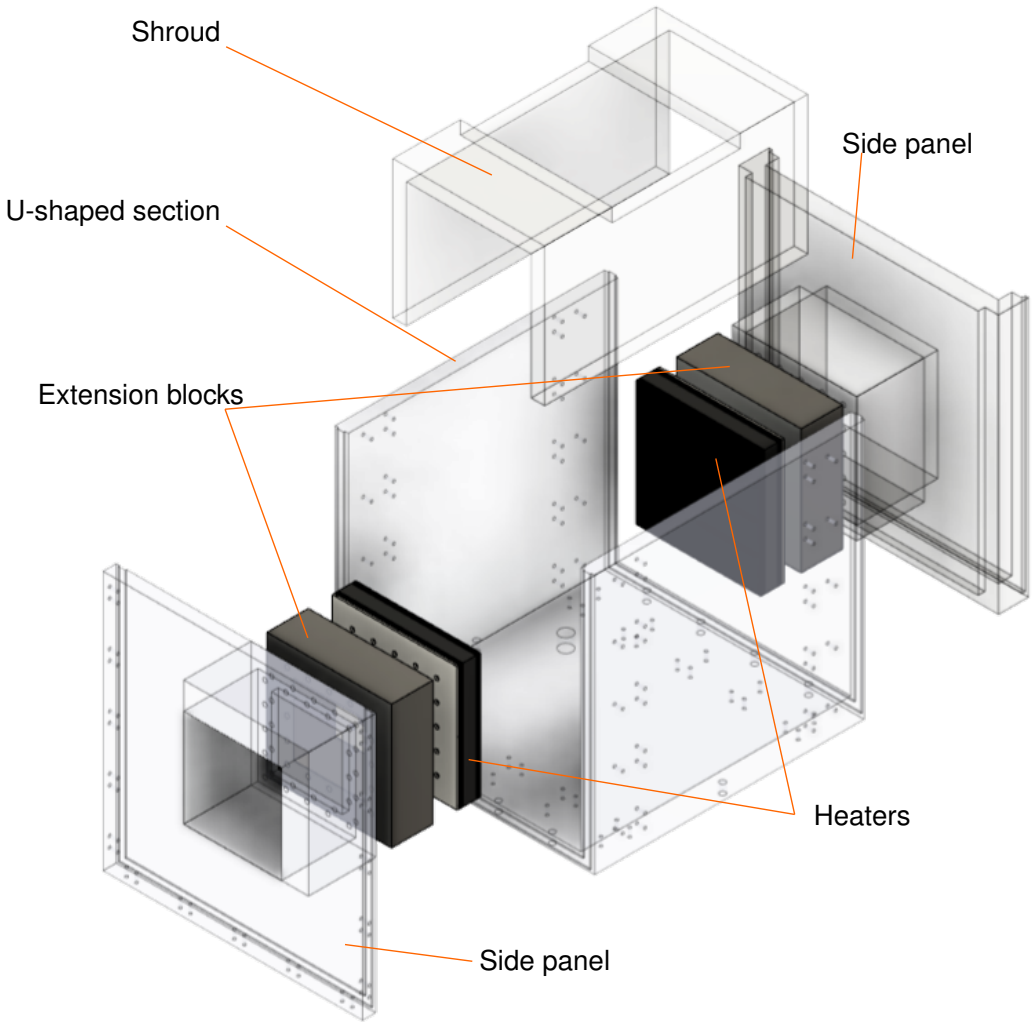

(a) Exploded view of the apparatus

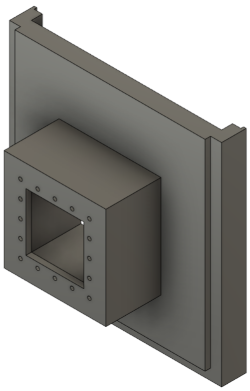

(b) Side panel

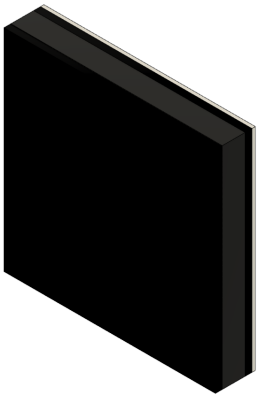

(c) Heater

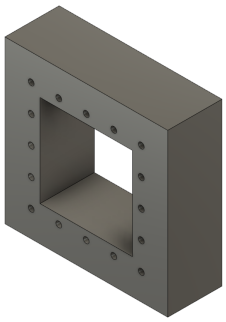

(d) Extension block

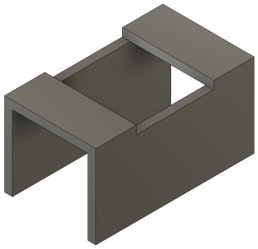

(e) Shroud

Figure 3.5: Apparatus

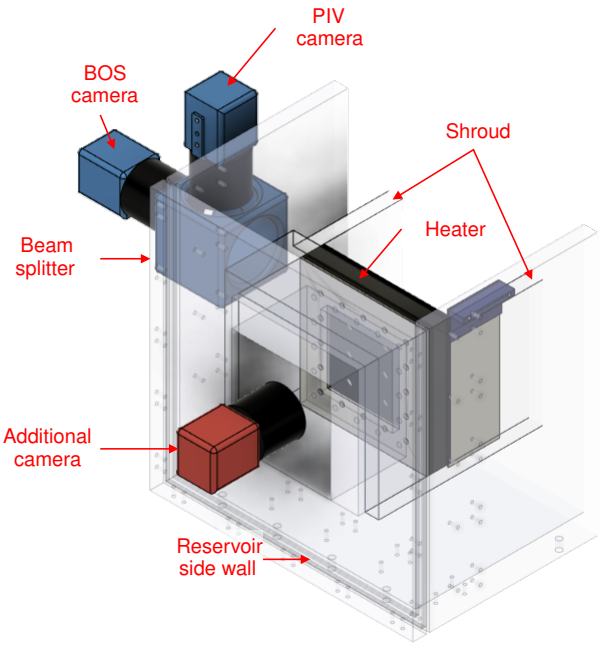

Figure 3.6: Optical access for an additional camera (coloured red) or IR camera.

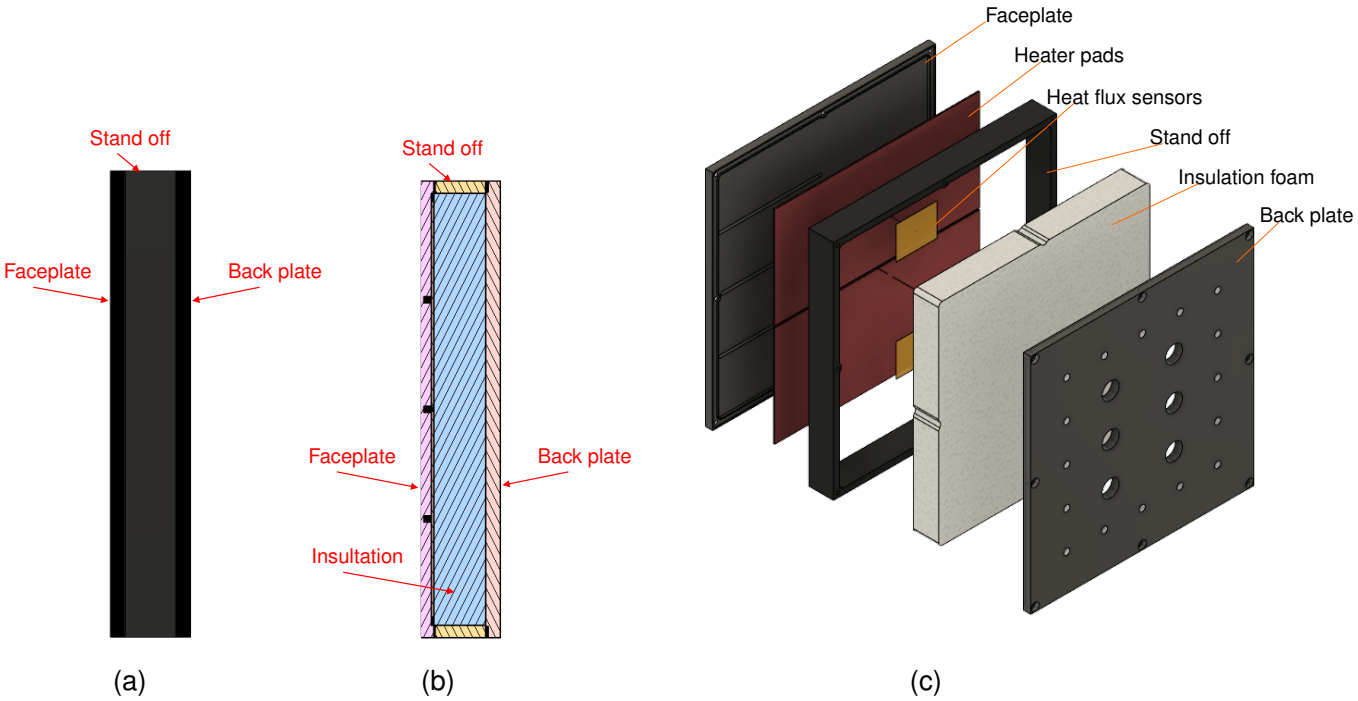

Figure 3.7: Plate heater construction (a) side view, (b) section view and (c) exploded view.

thermocouples measure the temperature ≈ 1 mm from the water surface. These measurements are used to infer the wet surface temperature, an uncertainty analysis of these measurements is discussed in section 3.5. Aluminium is used due to its high thermal conductivity as compared to other commonly used materials such as stainless steel. However, this required the faceplate and rear plate to be anodised to minimise corrosion. During the anodisation process the aluminium surfaces were dyed matte black to minimise reflections. HDPE was used as a stand-off due to its thermal and electrical insulation properties and the ease with which it may be machined. As a result the conductive heat loss from the heater to the rest of the apparatus was assumed negligible. The silicone heater pads are a standard commercially available product[3] with nominal dimensions 170 mm by 85 mm and are anecdotally reported to generate heat more uniformly than similar style heaters i.e. MICA or polyimide (Kapton) coated heaters. Each heater is rated to a nominal 200 W and thus a maximum heat flux of $13.84\,\mathrm{kW/m^2}$. Despite having two independent heat generating elements separated by ≈ 1 mm, an isoflux condition is assumed to be achieved due to the relatively thick and high thermal conductivity aluminium substrate. This was qualitatively confirmed using an IR camera with the heater in air.

Once installed it was discovered that the heating surface was slightly dished as shown in Figure 3.8. As discussed in chapter 5, this curvature appears to influence the flow and complicates the analysis due to difficulty in identifying the heating surface position in the PIV and BOS images.

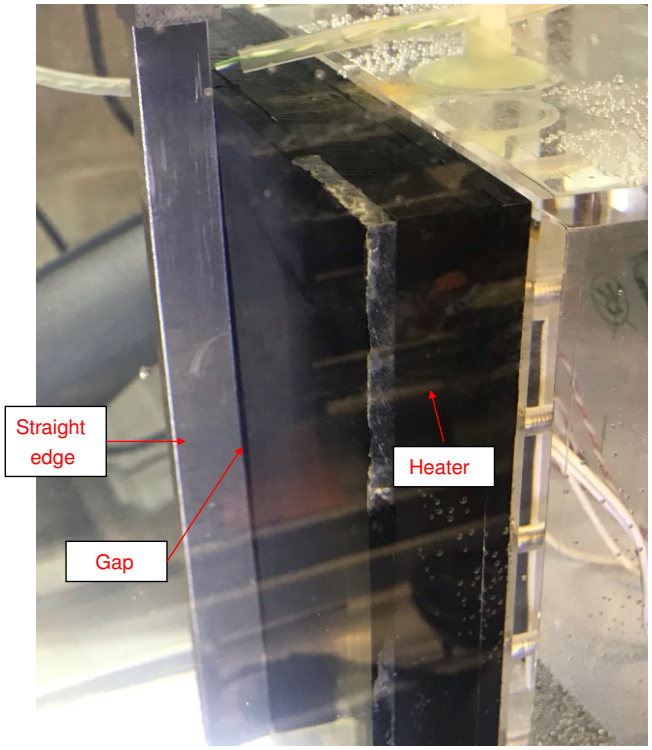

Figure 3.8: Photograph of the curvature of the heating surface when installed. The heater is a 187 mm square, the maximum gap is ≈ 1 mm

[3] supplied by tecnologic UK

3.3 Cooling

The reservoir is lagged with Dacron insulation foam during operation to minimise heat losses to the environment. Additionally the ambient temperature in the lab was maintained at $\approx 26\,^{\circ}$C. To prevent the water in the reservoir achieving exceedingly high temperatures a cooling system was required. A schematic of the system is shown in Figure 3.9. A $500\,$W aquarium chiller is used which approximately matches the heat input from the heater.

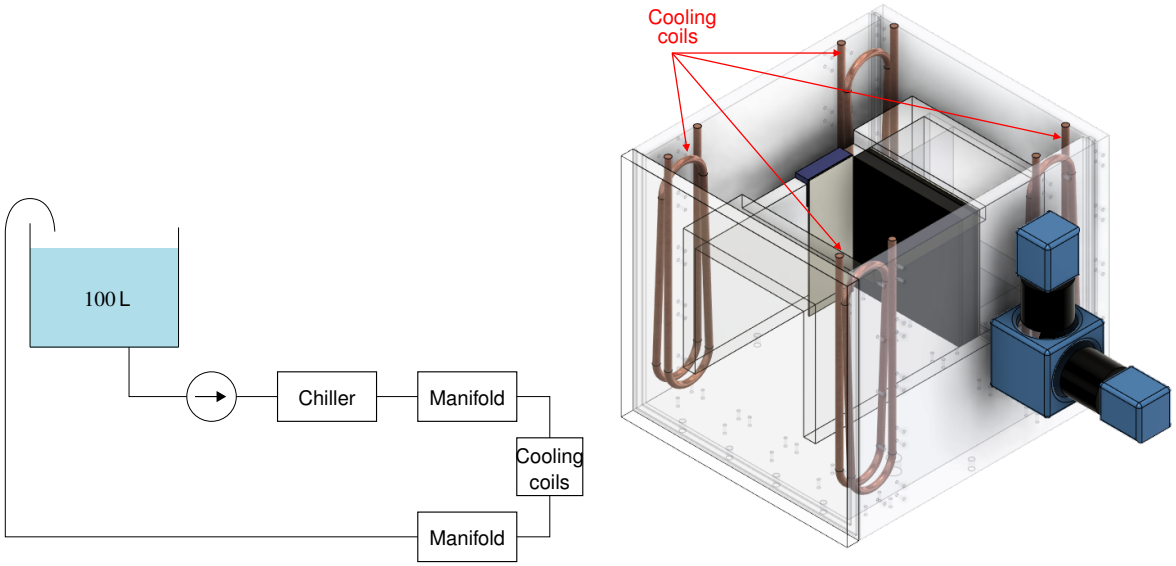

Figure 3.9: Cooling system (a) schematic, (b) cooling coil locations.

Daverat et al.[47,65] used a suction and discharge cooling arrangement. Given the more complex reservoir design used in this work a heat exchanger type cooling system was used instead. The heat exchangers were four coiled copper tubes located in the corners of the reservoir away from the measurement region as seen in Figure 3.9b.

The coolant, water, is circulated continuously through four cooling coils which are inserted into the corners of the reservoir as far from the measurement region as is possible. Each cooling coil is made from bent copper tube in a two loop arrangement which spans the vertical height of the reservoir and is approximately $75\,$mm wide. A large body of water is used which ensures that the ambient condition has little effect on the cooling system.

3.4 Power, control and data acquisition

3.4.1 Ancillary instrumentation

Determination of the experimental conditions requires measurement of the temperature, heat flux, voltage, and current. A summary of the ancillary instrumentation is given in Table 3.6. Note that for the work reported in this thesis none of the instrumentation associated with Heater 2 was installed. Figure 3.10 illustrates the thermocouple and heat flux sensor installation locations. It may be seen that the temperature and heat flux measurements are taken in the reservoir and in the vicinity of the heaters. Voltage and current measurements are taken from the power supply units (PSUs) and from shunt resistors (described in subsection 3.4.3).

Table 3.6: Ancillary instrumentation

Identifier	Type	Supplier	Region	Location
Tbh	K-type thermocouple	RS components Ltd	Reservoir	No. 1 in Figure 3.10
Tbm	K-type thermocouple	RS components Ltd	Reservoir	No. 2 in Figure 3.10
Tbc	K-type thermocouple	RS components Ltd	Reservoir	No. 3 in Figure 3.10
Tout	K-type thermocouple	RS components Ltd	Reservoir	No. 4 in Figure 3.10
Tin	K-type thermocouple	RS components Ltd	Reservoir	No. 5 in Figure 3.10
TH1t	K-type thermocouple	RS components Ltd	Heater 1	No. 6 in Figure 3.10
TH1m	K-type thermocouple	RS components Ltd	Heater 1	No. 7 in Figure 3.10
TH1b	K-type thermocouple	RS components Ltd	Heater 1	No. 8 in Figure 3.10
TH2t	K-type thermocouple	RS components Ltd	Heater 2	Not used
TH2m	K-type thermocouple	RS components Ltd	Heater 2	Not used
TH2b	K-type thermocouple	RS components Ltd	Heater 2	Not used
Tamb	K-type thermocouple	RS components Ltd	Ambient	Indicator only
THFSH1T	T-type thermocouple	-	Heater 1	No. 9 in Figure 3.10
THFSH1B	T-type thermocouple	-	Heater 1	No. 10 in Figure 3.10
THFSH2T	T-type thermocouple	-	Heater 2	Not used
THFSH2B	T-type thermocouple	-	Heater 2	Not used
VS1	Voltage	-	Heater 1	See Figure 3.15
VS2	Voltage	-	Heater 1	See Figure 3.15
VS3	Voltage	-	Heater 2	Not used
VS4	Voltage	-	Heater 2	Not used
COM	Voltage	-	Heater 1&2	See Figure 3.15
HFSH1t	HFS-5 heat flux sensor	Omega Ltd	Heater 1	No. 9 in Figure 3.10
HFSH1b	HFS-5 heat flux sensor	Omega Ltd	Heater 1	No. 10 in Figure 3.10
HFSH2t	HFS-5 heat flux sensor	Omega Ltd	Heater 2	Not used
HFSH2b	HFS-5 heat flux sensor	Omega Ltd	Heater 2	Not used

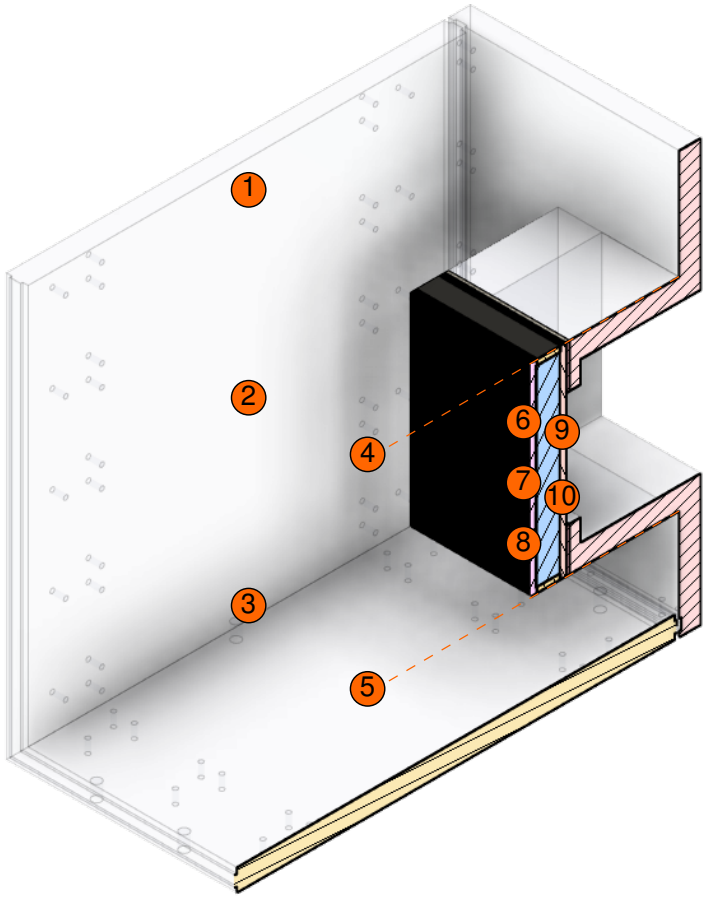

Figure 3.10: Ancillary instrumentation locations are showed over a cross section of the apparatus. The numbered locations refer to (1) Tbh, (2) Tbm, (3) Tbc, (4) Tin, (5) Tout, (6) TH1t, (7) TH1m, (8) TH1b, (9) HFSH1T and THFSH1T, and (10), HFSH1B and THFSH1B.

3.4.2 Data acquisition

Control, monitoring and data acquisition was achieved through a National Instruments LabView program[4] as shown in Figure 3.11. On the left are the sensor inputs which are collected by either a Keithley 2701 digital multimeter, or one of two modules within the National Instruments compact DAQ device.

Data from these input devices is processed by the LabView program and output to the user interface (UI) and if desired recorded as a TDMS file output. Select screenshots of the UI are shown in Figure 3.12. Through the UI, a user could control the PSUs, view instantaneous data via a schematic of the apparatus or a time history output. Also provided was a temperature calibration function which recorded temperature over a defined period and provided an average and standard deviation of the results.

[4]The program is written as a state machine to handle the large number of concurrent activities.

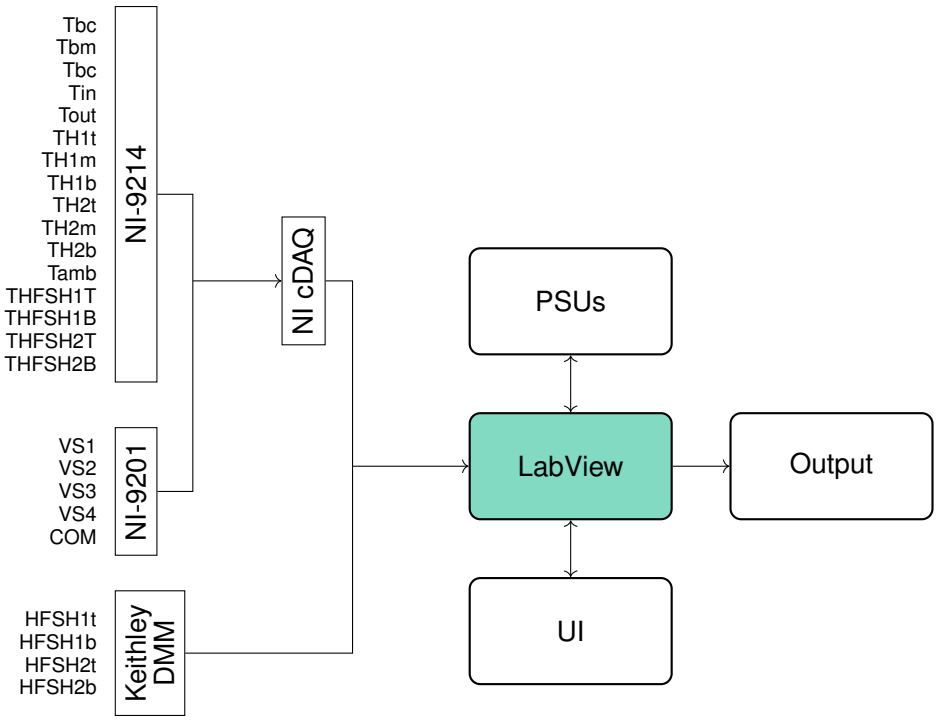

Figure 3.11: LabView schematic

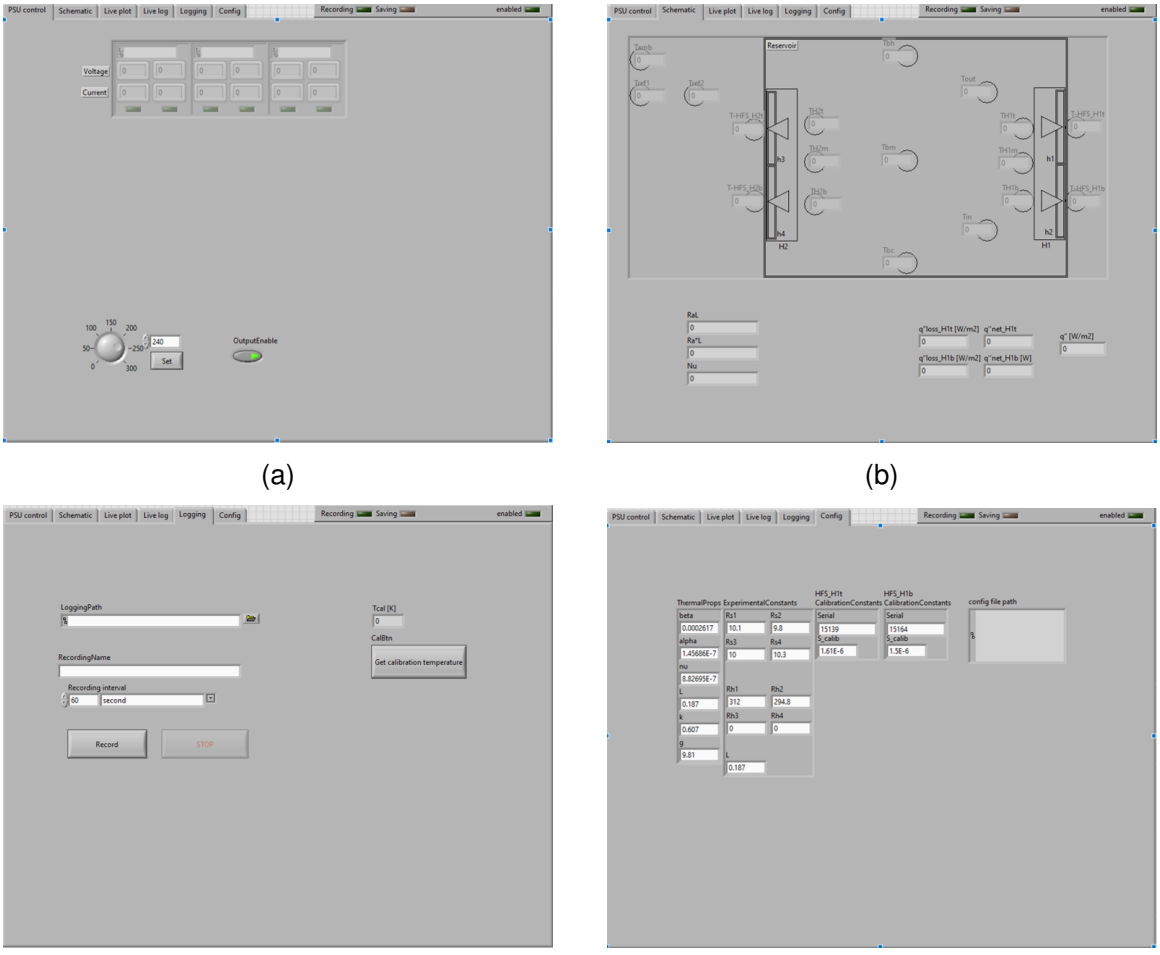

(a) (b)

(c) (d)

Figure 3.12: Screenshots of the LabView user interface. (a) Heater control, (b) schematic, (c) data logging, and (d) configuration

3.4.3 Power and control

Power is supplied by three dual channel DC Aim TTi CPX400DP power supplies connected in series. These power supplies offer onboard measurement of voltage and current, and are readily controllable via National Instruments LabView. When connected in series the combined maximum output is 300 VDC and 20 A which was more than sufficient to produce the required experimental conditions.

The resistance (R) of each silicone heater pad was measured using a Metrix MTX 3293 multimeter[67] over a range of conditions encompassing the experimental conditions. The average resistance over this range was found to be $R_1 = 312.0\,\Omega$ and $R_2 = 294.8\,\Omega$ for the top and bottom pads, respectively. The variation in resistance with temperature over this operating range was measured to be of the order $0.1\,\Omega$ and is thus negligible. Therefore, the resistance of the metal plate heaters is assumed not to be temperature dependent and the average values are used henceforth.

Since each silicone pad heater has a different resistance the current supplied to each must be adjusted. This is achieved through the introduction of a rheostat and resistor as seen in Figure 3.13.

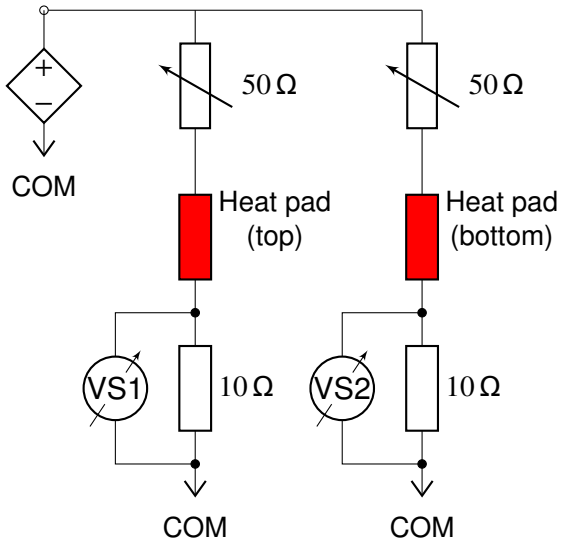

Figure 3.13: Circuit diagram of the power supply and control of individual pad heaters (red).

The circuit features $50\,\Omega$ rheostats used for fine tuning the current supplied to each silicone pad heater. Also, a nominal $R_S = 10\,\Omega$ shunt resistor is introduced to enable indirect measurement of the current supplied to each silicone heater pad. A shunt resistor is used in place of an ammeter due to the high DC voltage and impractical cost of an ammeter suited to these conditions.

The $50\,\Omega$ range of the rheostats was determined such that it exceeded the variation in resistance of the supplied silicone heater pads. The $R_S = 10\,\Omega$ shunt resistor was specified based on the resolution of the measurement device; a National Instruments data acquisition (DAQ) module (NI9201). The NI9201 DAQ module has a 12-bit resolution and, like most voltage sensors, has a

range of $V_S = \pm 10\,\text{V}$ and thus a maximum resolution of $4.88\,\text{mV}$. Using Ohm's law the nominal current for a single heater pad at maximum output voltage is $I_{max} = V_{max}/R = 1\,\text{A}$. Thus to use the majority of the sensing range of the NI9201 module, resistance is $R_S = V_S/I_{max} = 10\,\Omega$.

The relatively high DC voltage requires components with a high power rating. At the maximum achievable voltage each rheostat dissipates $50\,\text{W}$ and each shunt resistor $\leq 10\,\text{W}$. Thus, the electrical components are housed in a fireproof plastic enclosure with a fan fitted to provide cooling during operation.

3.5 Uncertainty analysis

The experimental condition is primarily characterised by the modified Rayleigh number

$$Ra_x^* = \frac{g\beta q'' x^4}{k\nu\alpha} \tag{3.1}$$

However, verification of the conditions can be achieved by comparison with a correlation for local Nusselt number

$$Nu_x = \frac{q'' x}{\theta_{wx} k} \tag{3.2}$$

where θ_{wx} is the local wall excess temperature. Or by comparison with correlations for average Nusselt number

$$\overline{Nu}_L = \frac{q'' L}{(\theta_w)_{L/2} k} \tag{3.3}$$

where $(\theta_w)_{L/2}$ is the wall excess temperature at the mid height $(L/2)$.

The calculation of these terms is dependent upon many measured variables, each of which has an associated uncertainty. Equations which combine multiple measured variables are called data reduction equations (DREs) which may serve to magnify or demagnify the contributions to uncertainty from the various measured values. A detailed uncertainty analysis (DUA) is performed starting with the more fundamental measurements and working up to DREs. A Taylor series method is used, as defined by Coleman and Steele [68] which is briefly summarised.

The uncertainty is defined to be the combination of systematic and random errors which may be related by

$$u_r = (b_r^2 + s_r^2)^{1/2} \tag{3.4}$$

where u_r, b_r and s_r are the overall, systematic and random uncertainty, respectively.

The ultimate goal of a detailed uncertainty analysis is the determination of u_r. The systematic uncertainties are related to the average error in the measured quantities and the random uncertainty is related to the distribution over the measurement period. The random uncertainty is estimated from the standard deviation of the results over the measurement period. The analysis considered in this chapter does not consider the random uncertainty. For the results reported in Chapter 5 the random uncertainty is included and makes negligible difference to the uncertainties determined herein.

Insight into the origin of the systematic uncertainty can be gained through the definition of uncertainty magnification factors (UMFs) and uncertainty percentage contributions (UPCs). A UMF describes to what extent a variable is magnified by a DRE and can be defined as

$$UMF_i = \frac{X_i}{r}\frac{\partial r}{\partial X_i} = \frac{X_i}{r}\theta_i \tag{3.5}$$

where X_i is the ith variable, r is the result, and θ_i is the ith sensitivity coefficient.

Of greater interest are the UPCs which describe the contribution of each variable to the overall systematic uncertainty. A UPC can be defined as

$$UPC_i = \frac{(\frac{\partial r}{\partial X_i})^2 b_X^2}{b_r^2} = \frac{UMF_i^2 (\frac{b_X}{X_i})^2}{(b_r/r)^2} \tag{3.6}$$

where

$$b_r^2 = \sum_{i=1}^{j} \theta_i^2 b_{X_i}^2 \tag{3.7}$$

Introduced here are the relative uncertainties of each variable $\delta_i = b_X/X_i$ and overall $\delta_r = b_r/r$, where b_X is the uncertainty of the variable X_i. It may be noted that a nominal value for the variable X_i is required to determine these quantities and the nominal result r. These nominal values are thus based on the average of the measurements taken.

Hence the determination of the UMFs and UPCs requires the derivation of the sensitivity coefficient, the specification of the uncertainty in each variable, and the nominal values. This methodology is now applied to each of the measured and derived quantities for the determination of the experimental conditions.

3.5.1 Quiescent temperature

The apparatus is located in a room which has limited ambient temperature control and is thus susceptible to variation due to changing outdoor temperatures. To achieve the most stable conditions the room heating[5] is set to maintain a temperature $26\,^{\circ}$C which is greater than outdoor temperatures for most of the year. However, stable conditions could only be produced when excessively high or low outdoor temperatures are avoided.

It took approximately three hours to gather a complete set of experimental measurements. Measurements were taken around midday as variations in ambient were minimal $\approx \pm 0.5\,^{\circ}$C/hr. The use of a well insulated reservoir further mitigated the apparatus from variations in outdoor and ambient temperature. This enabled experimental conditions to be reproduced with excellent agreement.

The relatively high heat flux unavoidably results in a substantial, but stable, thermal stratification in the reservoir. The thermal stratification was observed to be linear and thus the quiescent temperature is also assumed to vary linearly from the leading to the trailing edge of the heater. The local quiescent temperature $T_{\infty,x}$ is thus determined from two thermocouple measurements; T_{in} and T_{out} as shown in Figure 3.10, and described by the equation (3.8).

$$T_{\infty,x} = T_{in} + \frac{x}{L}(T_{out} - T_{in}) \tag{3.8}$$

[5]This is the maximum possible setting.

The T_{in} thermocouple is at the same height as the heater leading edge ($x/L = 0$) and T_{out} is at the height of heater trailing edge at ($x/L = 1$). Both thermocouples are located far from the heating surface by approximately $\times 20$ the apparent thickness of the thermal boundary layer.

The sensitivity coefficients and nominal values are detailed in Table 3.7 and Table 3.8, respectively.

Table 3.7: Quiescent temperature sensitivity coefficients

Var.	Sensitivity coefficient
T_{in}	$\theta_{Tin} = 1 - \frac{x}{L}$
T_{out}	$\theta_{Tout} = \frac{x}{L}$
x	$\theta_x = \frac{1}{L}(T_{out} - T_{in})$
L	$\theta_L = -\frac{1}{L^2}(T_{out} - T_{in})$

Table 3.8: Values used in the detailed uncertainty analysis of $T_{\infty,x}$. X are average values, b_X uncertainty, and, δ relative uncertainty.

Var.	X	b_X	b_X/X	(X) source	$(b_X, b_X/X)$ source
T_{in}	294.41 K	-	0.75%	Measured	K-type standard
T_{out}	301.95 K	-	0.75%	Measured	K-type standard
x	$0 \leq x \leq L$	2 mm	-	-	Estimation
L	187 mm	0.1 mm	-	Measured	Instrument scale

As may be seen, the thermocouple values are used with the supplied uncertainty and no additional calibration is performed. The uncertainty of x relates to the location of the T_{in} and T_{out} thermocouple measurements. These locations were not measured directly and thus a bounding uncertainty of $b_X = \pm 2$ mm is assumed. The uncertainty of L is based on the scale accuracy on the machinist scale used to measure the surface. However, since the component has been CNC machined the tolerance is likely an order of magnitude better than this. However, as will be seen the effect on the overall uncertainty would be negligible.

The resulting $T_{\infty,x}$ and the associated uncertainty is presented in Table 3.9 and the UPCs are shown in Figure 3.14.

Table 3.9: Resulting $T_{\infty,x}$ and uncertainty at various locations

x/L	$T_{\infty,x}$	b_X
0.75	26.91 °C	1.79 °C
0.50	25.03 °C	1.58 °C
0.25	23.14 °C	1.75 °C

It may be seen that the overall uncertainty is relatively low due to the measurement being made by two thermocouples. The UPCs are dominated by the temperature measurement due to the use of K-type thermocouples with no additional calibration.

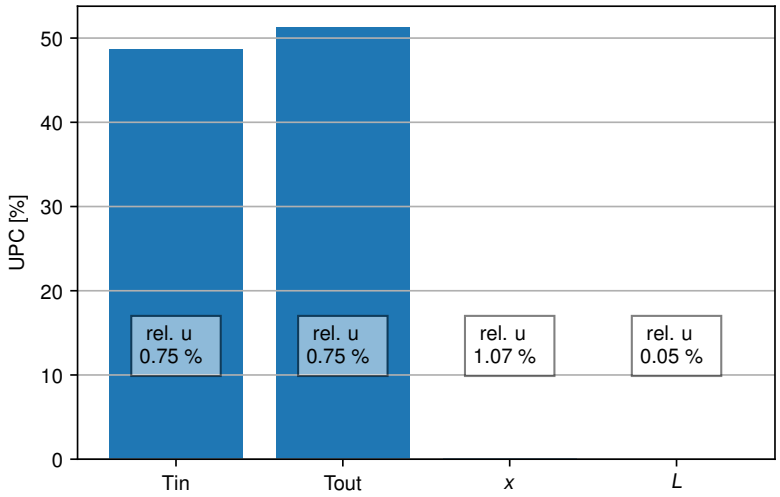

Figure 3.14: UPCs for $T_{\infty,x}$ at $x/L = 0.50$, the relative uncertainty for each variable is annotated.

3.5.2 Heat flux

A schematic of the heating arrangement is shown in Figure 3.15. As previously mentioned the heater substrate was insulated from the rest of the apparatus by a low thermal conductivity HDPE stand off. In addition to this, the entire apparatus, with the exception of the sides requiring optical access, was insulated with Dacron insulation. Thus, the remaining heat loss from the apparatus was assumed negligible [6].

Since each plate heater contains two silicone pad heaters (heater 1 and 2 as labelled in the diagram), the output from both must be sensibly combined along with unintentional heat loss to the ambient to enable calculation of the surface heat flux.

Heat loss from the silicone pad heaters, as opposed to heat directly supplied to the aluminium substrate, is measured by Omega HFS-5 sensors[69]. This is to minimise the disturbance to the isoflux condition by the sensors. Furthermore, the heat loss from each silicone heat pad is assumed to be uniform and equal to that measured by the sensors. Thus, the heat loss from each silicone pad heater is q''_{L1} and q''_{L2}, respectively.

Noting that the heat generated by the silicone heater pad can be described by Joule's law

$$\dot{Q} = I^2 R \tag{3.9}$$

[6] Confidence in this assumption was bolstered when the experiment was left to cool from a uniform reservoir temperature $\approx 50\,^{\circ}$C overnight and the maximum maximum rate of temperature drop was $< 1\,^{\circ}$C/hr.

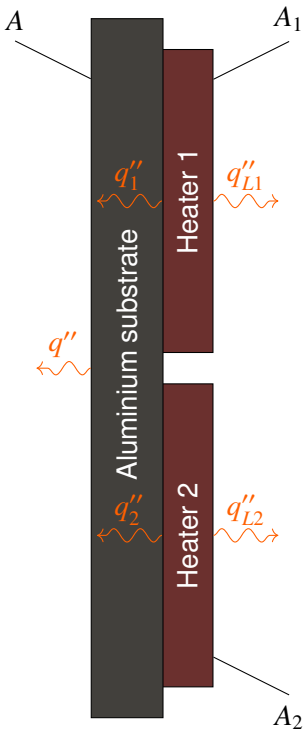

Figure 3.15: Heating schematic

An energy balance can be performed to determine the heat flux in relation to measurable quantities. The heat leaving heater 1 is given by

$$\begin{aligned} \dot{Q}_1 &= \left(\frac{V_{S1}}{R_{S1}}\right)^2 R_1 \\ &= (q_1'' + q_{L1}'')A_1 \\ \therefore q_1'' A_1 &= \left(\frac{V_{S1}}{R_{S1}}\right)^2 R_1 - q_{L1}'' A_1 \end{aligned} \tag{3.10}$$

and similarly for heater 2

$$q_2'' A_2 = \left(\frac{V_{S2}}{R_{S2}}\right)^2 R_2 - q_{L2}'' A_2 \tag{3.11}$$

The surface heat flux can thus be calculated with

$$q'' A = q_1'' A_1 + q_2'' A_2 \tag{3.12}$$

noting that $A_1 = A_2 = A_{pad}$ and $A = L^2$ is the area of the heater surface

$$\begin{aligned} q'' A &= \left(\frac{V_{S1}}{R_{S1}}\right)^2 R_1 + \left(\frac{V_{S2}}{R_{S2}}\right)^2 R_2 - (q_{L1}'' + q_{L2}'')A_{pad} \\ q'' &= \left(\frac{V_{S1}}{R_{S1}}\right)^2 \frac{R_1}{L^2} + \left(\frac{V_{S2}}{R_{S2}}\right)^2 \frac{R_2}{L^2} - (q_{L1}'' + q_{L2}'')\frac{A_{pad}}{L^2} \end{aligned} \tag{3.13}$$

$$q'' = q''_{supply} - q''_{loss} \tag{3.14}$$

It may be seen that if

$$\left(\frac{V_{S1}}{R_{S1}}\right)^2 \frac{R_1}{L^2} + \left(\frac{V_{S2}}{R_{S2}}\right)^2 \frac{R_2}{L^2} >> (q''_{L1} + q''_{L2}) \frac{A_{pad}}{L^2}$$

or

$$\frac{q''_{loss}}{q''_{supply}} << 1$$

then (3.13) simplifies to

$$q'' = \left(\frac{V_{S1}}{R_{S1}}\right)^2 \frac{R_1}{L^2} + \left(\frac{V_{S2}}{R_{S2}}\right)^2 \frac{R_2}{L^2} \tag{3.15}$$

When measured it was observed that

$$\frac{q''_{loss}}{q''_{supply}} \approxeq 1\%$$

and hence (3.15) was used to calculate the surface heat flux.

The sensitivity coefficients and nominal values are detailed in Table 3.10 and Table 3.11, respectively.

Table 3.10: Surface heat flux sensitivity coefficients

Var.	Sensitivity coefficient
V_{S1}	$\theta_{VS1} = \frac{2V_{S1}R_1}{R_{S1}^2 L^2}$
V_{S2}	$\theta_{VS2} = \frac{2V_{S2}R_2}{R_{S2}^2 L^2}$
R_{S1}	$\theta_{RS1} = -\frac{2V_{S1}^2 R_1}{R_{S1}^3 L^2}$
R_{S2}	$\theta_{RS2} = -\frac{2V_{S2}^2 R_2}{R_{S2}^3 L^2}$
R_1	$\theta_{R1} = \left(\frac{V_{S1}}{R_{S1}}\right)^2 \frac{1}{L^2}$
R_2	$\theta_{R2} = \left(\frac{V_{S2}}{R_{S2}}\right)^2 \frac{1}{L^2}$
L	$\theta_L = \frac{-2}{L^3}\left\{\left(\frac{V_{S1}}{R_{S1}}\right)^2 R_1 + \left(\frac{V_{S2}}{R_{S2}}\right)^2 R_2\right\}$

Table 3.11: Values used in the detailed uncertainty analysis of q''. X are average values, b_X uncertainty, and, δ relative uncertainty.

Var.	X	b_X	b_X/X	(X) source	$(b_X, b_X/X)$ source
V_{S1}	6.845 V	488 mV	-	Measured	Datasheet[70]
V_{S2}	6.841 V	488 mV	-	Measured	Datasheet[70]
R_{S1}	10.1 Ω	-	0.1%	Measured	User manual[67]
R_{S2}	9.8 Ω	-	0.1%	Measured	User manual[67]
R_1	312.0 Ω	-	0.1%	Measured	User manual[67]
R_2	294.8 Ω	-	0.1%	Measured	User manual[67]

The resulting q'' and the associated uncertainty is presented in Table 3.12 and the UPCs are shown in Figure 3.16.

Table 3.12: Resulting q'' and uncertainty

q''	b_X/X
$8.21\,\mathrm{kW/m^2}$	10.1%

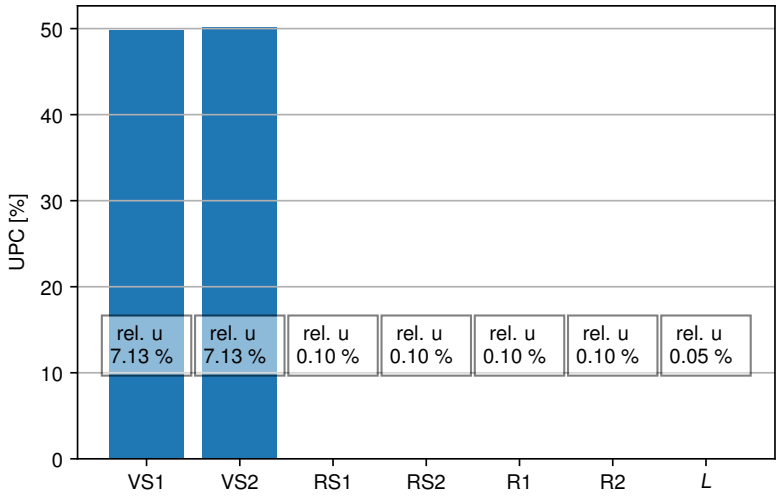

Figure 3.16: UPCs for q'' at $x/L = 0.50$, the relative uncertainty (δ) for each variable is annotated.

It may be seen that the UPCs are dominated by the voltage measurements of the shunt resistors. This is caused by the 12-bit resolution of the NI9201 DAQ module.

3.5.3 Surface temperature

The heater faceplate includes three $3\,\mathrm{mm}$ deep slots into which K-type thermocouples (TH1t, TH1m and TH1b from Table 3.6) are potted with a conductive silver loaded epoxy. The temperature measurement of the surface is thus made approximately $\geq 1\,\mathrm{mm}$ from the water facing surface. An illustration of the cross section is shown in Figure 3.17.

If one dimensional heat transfer is assumed in the steady state the temperature difference may be determined by

$$\begin{aligned} T_m - T_w &= q''\left(\frac{\Delta_a}{k_a} + \frac{\Delta_e}{k_e}\right) \\ &= q''R \end{aligned} \tag{3.16}$$

where T_w and T_m are the surface and measured temperatures, respectively. The $\Delta_a = 1\,\mathrm{mm}$ is the distance through the aluminium substrate and Δ_e is the distance from the bottom (as illustrated

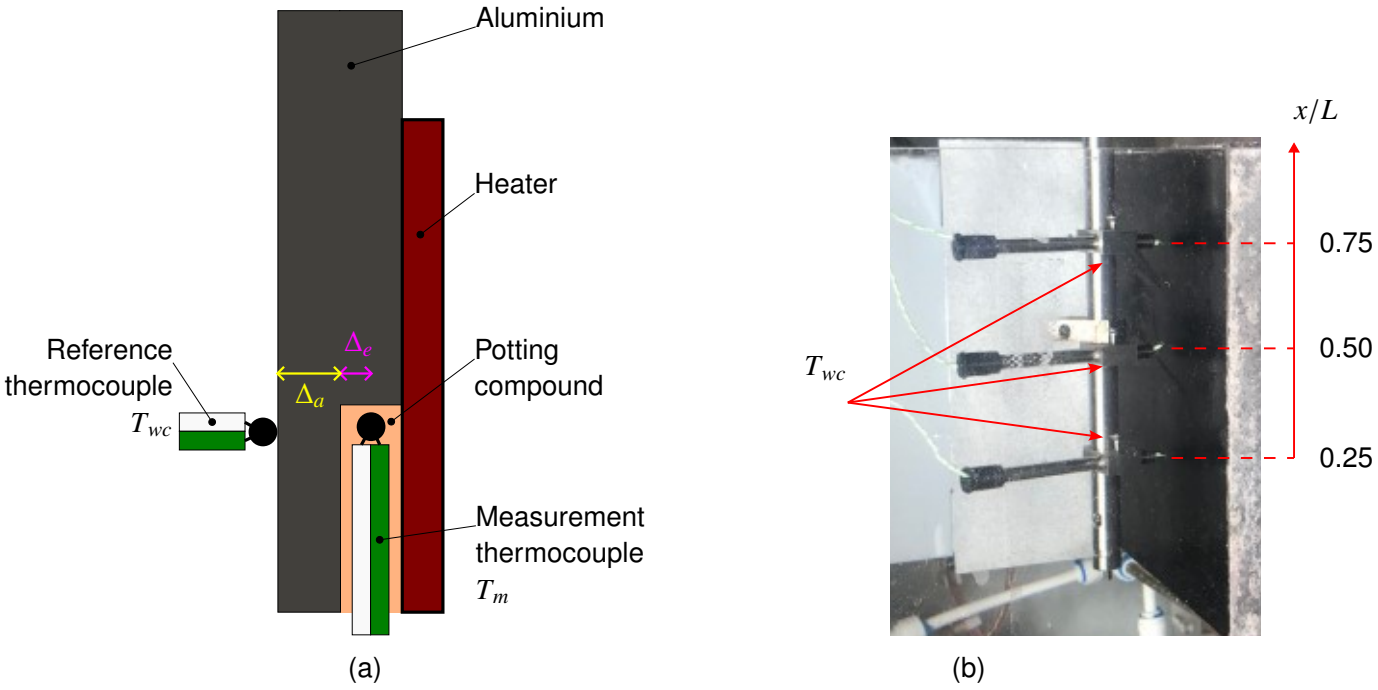

Figure 3.17: Calibration of potted thermocouples (T_m i.e. TH1t, TH1m and TH1b from Table 3.6) with a reference (T_{wc}). (a) Illustration of the heater cross section and (b) photograph of reference thermocouples suspended in the place and pressed against the heating surface.

in Figure 3.17) of the slot to the tip of the thermocouple. k_a and k_e are the thermal conductivity of the aluminium substrate and the epoxy, respectively. The alternative presentation of the equation introduces a thermal resistance R.

Values for q'' and Δ_a can be determined with relatively low uncertainty. However, the remaining terms are not easily determined. It is therefore necessary to experimentally determine a value for R.

To do so the surface temperature T_w must be measured directly such that R may be determined by

$$R = \frac{T_{mc} - T_{wc}}{q''_c} \tag{3.17}$$

where $T_{mc} - T_{wc}$ is the measured temperature difference between surface and thermocouple location. Thus, all the terms on the right hand side are measured enabling R to be determined with some associated uncertainty. The subscript 'c' in eqn (3.17) refers to a calibration measurement to differentiate it from an experimental measurement.

The temperature variation of the thermal conductivities k_a and k_e may be neglected if R is determined at conditions not too different to the experimental conditions. Since each potted thermocouple may have a slightly different Δ_e, each location will need to be calibrated.

A contact measurement is necessary as the Biot number would differ substantially if the reservoir were drained to allow IR measurement of the surface. Hence, reference thermocouples are introduced and precisely aligned with the embedded thermocouples as depicted in Figure 3.17.

The relative error between the thermocouples measuring T_{wc} and T_{mc} was calibrated by first

taking a set of adiabatic measurements and the difference subtracted from T_{mc}. Next, a steady state condition is achieved with measurements of R taken over a prolonged period as shown in Figure 3.18. It may be seen that R takes a different value at the $x/L = 0.75, 0.5$ and 0.25 locations as denoted by Rt, Rm, and Rb, respectively. The values are relatively stable with a random uncertainty of only $b = 1.33\%, 0.66\%$ and 0.33% at each x/L position. Nevertheless, the uncertainty for R is inclusive of the random uncertainty as per eqn (3.4).

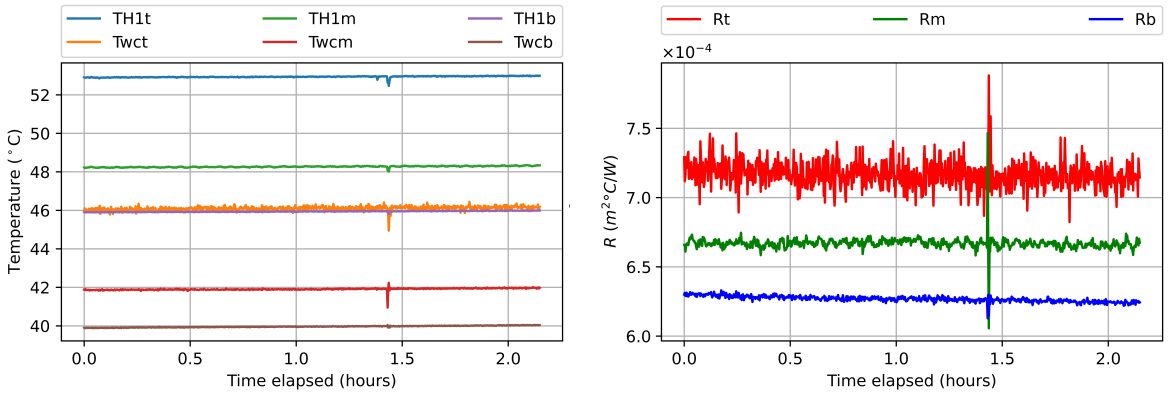

(a) (b)

Figure 3.18: R calibration conditions (spike at ≈ 1.4 hr is due to data logging glitch). Time traces of measurement thermocouples (TH1t, TH1m, TH1b), reference thermocouples (Twct, Twcm, Twcb) and the resulting thermal resistances (Rt, Rm, Rb). Names containing t, m and b refer to x/L = 0.75, 0.5, 0.25, respectively.

With R determined the wall surface temperature may be estimated from the thermocouple measurements with a rearrangement of eqn (3.17)

$$T_w = T_m - q''R \tag{3.18}$$

Thus it is necessary to first determine the uncertainty for R and then use this in the determination of the uncertainty in T_w. These analyses will be presented together.

The sensitivity coefficients and nominal values are detailed in Table 3.13 and Table 3.14, respectively.

Table 3.13: Surface temperature sensitivity coefficients

Var.	Sensitivity coefficient
T_{mc}	$\theta_{Tmc} = \frac{1}{q''_c}$
T_{wc}	$\theta_{Twc} = -\frac{1}{q''_c}$
q''_c	$\theta_{qc} = -\frac{T_{wc}-T_{mc}}{(q''_c)^2}$
T_m	$\theta_{Tm} = 1$
R	$\theta_R = -q''$
q''	$\theta_q = -R$

The average temperature difference observed during the calibration were $6.83\,^{\circ}$C, $6.36\,^{\circ}$C and

Table 3.14: Values used in the detailed uncertainty analysis of R and T_w. X are average values, b_X uncertainty, and, δ relative uncertainty.

Var.	X	b_X	b_X/X	(X) source	$(b_X, b_X/X)$ source
q_c''	8.21 kW/m2	-	9.32%	Measured	Table 3.12
q''	8.21 kW/m2	-	10.1%	Measured	Table 3.12
T_{wc}	319.26 K $x/L = 0.75$	-	0.75%	Measured	K-type standard
	315.06 K $x/L = 0.50$	-	0.75%	Measured	K-type standard
	313.11 K $x/L = 0.25$	-	0.75%	Measured	K-type standard
T_{mc}	326.09 K $x/L = 0.75$	-	0.75%	Measured	K-type standard
	321.42 K $x/L = 0.50$	-	0.75%	Measured	K-type standard
	319.09 K $x/L = 0.25$	-	0.75%	Measured	K-type standard
T_m	319.6 K $x/L = 0.75$	-	0.75%	Measured	K-type standard
	315.2 K $x/L = 0.50$	-	0.75%	Measured	K-type standard
	313.1 K $x/L = 0.25$	-	0.75%	Measured	K-type standard

$5.98\,^\circ$C, at $x/L = 0.75, 0.5$ and 0.25, respectively. The resulting R, T_w, and the associated uncertainty is presented in Table 3.15. The UPCs are shown in Figure 3.19.

Table 3.15: Resulting R, T_w, and, uncertainty at various locations.

x/L	R	b_X/X
0.75	7.166×10^{-4} Km^2/W	50.98%
0.50	6.669×10^{-4} Km^2/W	53.90%
0.25	6.268×10^{-4} Km^2/W	56.88%
	T_w	b_X
0.75	40.57 °C	3.88 °C
0.50	40.16 °C	3.77 °C
0.25	34.77 °C	3.79 °C

It may be seen that R both has a high relative uncertainty and has the highest UPC value in the determination of T_w. The overall uncertainty in T_w is almost doubled when compared to a standard K-type uncertainty. On the one hand this is not ideal as the surface temperature is a major contributor to Nusselt number uncertainties. However, on the other hand, the calibration method has substantially reduced the uncertainty due to the several unknown factors.

There is an interesting relationship between R, $T_m - T_w$ and δ_R. If the thermal resistance were relatively small i.e. $R \to 0$ due to increased thermal conductivity or thinner substrate, then eqn (3.18) would simplify to $T_w \approx T_m$. Thus, as $R \to 0$ the error in the surface temperature measurement tends to zero. However, as $R \to 0$ the temperature difference produced in the calibration would become vanishingly small and thus δ_R would become increasingly large. Thus, as $R \to 0$ there comes a point where the application of the calibration introduces more uncertainty than it corrects. Here, the relatively small difference in temperature during the calibration leads to a relatively large uncertainty for R. This is in part due to the relatively high thermal conductivity of the aluminium heater and also due to the relative uncertainty of the K-type thermocouples used to perform the measurements. Despite this, performing the calibration slightly reduced the

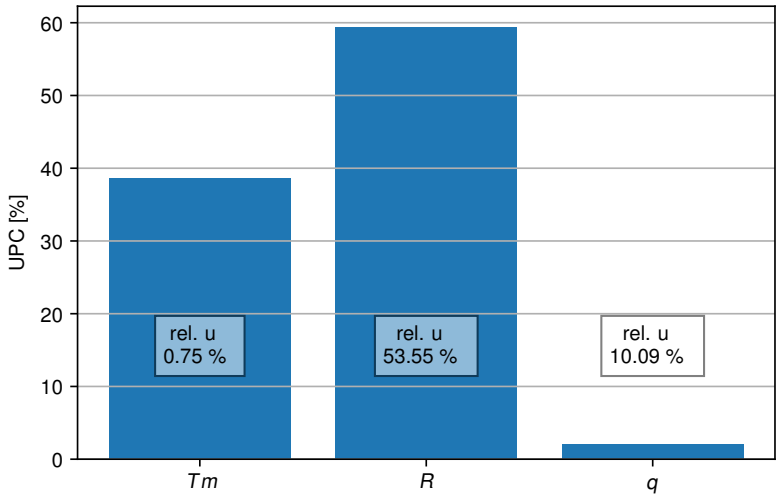

Figure 3.19: UPCs for T_w at $x/L = 0.50$, the relative uncertainty for each variable is annotated.

overall uncertainty in the surface temperature measurement compared to simply estimating the uncertainty of eqn (3.16).

Measurement of the surface temperature is certainly a prime candidate for improvement if less uncertainty in the experimental conditions were required. This could most readily be achieved by measuring the surface temperature much closer to the surface such that the thermal resistance is reduced. Alternatively, further calibration of the thermocouples beyond the supplied calibration would also make a significant contribution to improve the measurement of R and T_w.

3.5.4 Rayleigh number

The experimental condition is primarily described by the modified Rayleigh number (2.4) which is repeated here

$$Ra_x^* = \frac{g\beta q'' x^4}{k\nu\alpha} \tag{3.19}$$

where $g = 9.81\,\mathrm{m/s^2}$ is the gravitational constant and is assumed to have negligible uncertainty. Several other terms, β, k, ν and α, are thermodynamic properties which depend on temperature.

In keeping with tradition[5], the thermodynamic properties are evaluated at the film temperature i.e.

$$T_f = \frac{T_{\infty,L/2} + T_{w,L/2}}{2} \approxeq \frac{(T_{in} + T_{out})/2 + T_{H1m} + q''R}{2} \tag{3.20}$$

where T_{in}, T_{out} and T_{H1m} are thermocouple measurements as defined in Table 3.6 and the evaluation of the heat flux, quiescent, and surface temperature has been performed in the preceding sections.

The sensitivity coefficients and nominal values are detailed in Table 3.16 and Table 3.17, respectively.

Table 3.16: Rayleigh number sensitivity coefficients

Var.	Sensitivity coefficient
g	$\theta_g = \frac{\beta q'' x^4}{k\alpha\nu}$
β	$\theta_\beta = \frac{g q'' x^4}{k\alpha\nu}$
q''	$\theta_q = \frac{g\beta x^4}{k\alpha\nu}$
x	$\theta_x = 4x^3 \frac{g\beta q''}{k\alpha\nu}$
k	$\theta_k = -\frac{g\beta q'' x^4}{k^2\alpha\nu}$
α	$\theta_\alpha = -\frac{g\beta q'' x^4}{k\alpha^2\nu}$
ν	$\theta_\nu = -\frac{g\beta q'' x^4}{k\alpha\nu^2}$

Table 3.17: Values used in the uncertainty analysis of Ra_x^*. X are average values, b_X the systematic uncertainty.

Var.	X	b_X	b_X/X	(X) source	$(b_X, b_X/X)$ source
g	$9.81\,\mathrm{m/s^2}$	-	-	-	Negligible
β	$0.000\,31\,\mathrm{K^{-1}}$	-	-	python iapws module	Negligible
q''	$8206\,\mathrm{W/m^2}$	-	10.09%	Measured	Calculated
x	$0 \leq x \leq L(= 187\,\mathrm{mm})$	$0.1\,\mathrm{mm}$	-	Measured	Instrument scale
k	$0.616\,\mathrm{W/mK}$	-	1.5%	python iapws module	From[71]
ν	$7.838 \times 10^{-7}\,\mathrm{m^2/s}$	-	1%	python iapws module	Derived from[71]
α	$1.481 \times 10^{-7}\,\mathrm{m^2/s}$	-	1.513%	python iapws module	Derived from[71]

It may be seen that the thermodynamic properties are obtained from a python module based on the guidance provided by the international association for the properties of water and steam (IAPWS)[71]. The IAPWS provide empirical solutions to the fundamental thermodynamics equations to enable a variety of properties to be determined where two thermodynamic properties are known. The thermodynamic properties are generally correlated with small relative uncertainty i.e. $\delta \leq 1.6\%$. Some properties, such as β, are not provided directly by the IAPWS and may instead be derived from their correlations. Thus, the uncertainty of these properties is not defined. However, the volumetric thermal expansion coefficient is proportional to the specific volume as

$$\beta \propto \frac{\partial v}{\partial T} \tag{3.21}$$

The specific volume v has an exceptionally low relative uncertainty of $u_v/v \approx 0.0001\%$ and over a small difference in temperature i.e. the wall excess temperature, the variation is small. Hence the uncertainty in β is assumed negligible.

The resulting Ra_x^* and the associated uncertainty is presented in Table 3.18 and the UPCs are shown in Figure 3.20.

As may be seen the UPCs are dominated by q'' to the extent that the relative uncertainty of Ra_x^* is almost equal to that of q''. A reduction in uncertainty could be achieved by reducing the relative uncertainty of the heat flux as described previously in section 3.5.2.

Table 3.18: Resulting Ra and the associated relative uncertainty at various locations.

x/L	Ra_x^*	b_X/X
0.75	1.359×10^{11}	10.36%
0.50	2.684×10^{10}	10.37%
0.25	1.677×10^{9}	10.39%

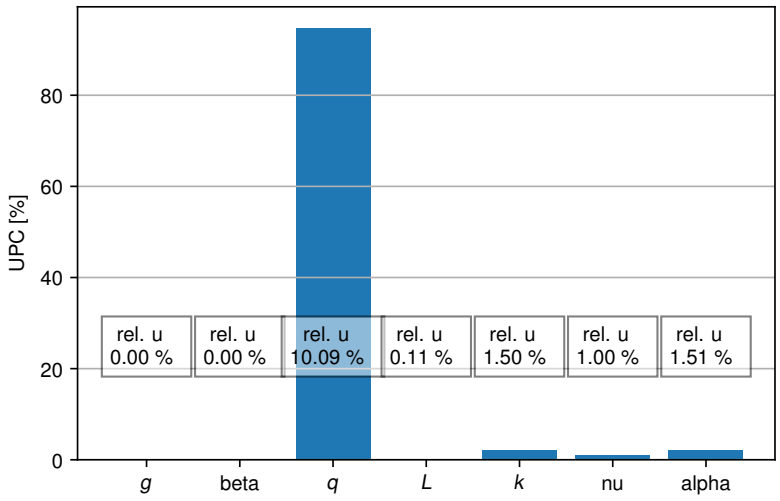

Figure 3.20: UPCs for Ra^* at $x/L = 0.50$, the relative uncertainty for each variable is annotated.

3.5.5 Nusselt number

Most generally the Nusselt number may be defined as

$$Nu_\ell = \frac{h\ell}{k} \tag{3.22}$$

where h, ℓ and k are the convective heat transfer coefficient, characteristic dimension, and thermal conductivity, respectively. For a vertical natural convection surface it is convention to let $\ell \equiv x$.

Since h can not be directly measured, it is substituted using Newton's law of cooling

$$q'' = h(T_w - T_\infty) \tag{3.23}$$

where T_w and T_∞ are the wall and fluid temperatures, respectively. Thus, the Nusselt number may be rewritten as

$$Nu_x = \frac{q''x}{(T_w - T_\infty)k} = \frac{q''x}{(\theta_{w,x})k} \tag{3.24}$$

where $\theta_{w,x}$ is the local wall excess temperature. In this form, the local Nusselt number may be determined from measured variables already discussed in the preceding sections. The thermal conductivity is determined at the film temperature. For clarity $\theta_{w,x}$ is evaluated separately.

The sensitivity coefficients and nominal values are detailed in Table 3.19 and Table 3.20, respectively.

Table 3.19: Nusselt number sensitivity coefficients

Var.	Sensitivity coefficient
q''	$\theta_q = \frac{x}{\theta_{\infty,x}k}$
x	$\theta_x = \frac{q''}{\theta_{\infty,x}k}$
$\theta_{\infty x}$	$\theta_\theta = -\frac{q''x}{\theta^2_{\infty,x}k}$
k	$\theta_k = -\frac{q''x}{\theta_{\infty,x}k^2}$
T_w	$\theta_{Tw} = 1$
T_∞	$\theta_{T_\infty} = -1$

Table 3.20: Values used in the detailed uncertainty analysis of $\theta_{w,x}$ and Nu_x. X are average values and b_X the systematic uncertainty.

Var.	X	b_X	b_X/X	(X) source	$(b_X, b_X/X)$ source
T_∞	26.91 °C ($x/L = 0.75$)	1.79 °C	-	Measured	Calculated
	25.03 °C ($x/L = 0.50$)	1.58 °C	-	Measured	Calculated
	23.14 °C ($x/L = 0.25$)	1.75 °C	-	Measured	Calculated
T_w	40.57 °C ($x/L = 0.75$)	3.88 °C	-	Measured	Calculated
	40.16 °C ($x/L = 0.50$)	3.77 °C	-	Measured	Calculated
	34.77 °C ($x/L = 0.25$)	3.79 °C	-	Measured	Calculated
k	0.618 W/m^{2}K		1.5%	python iapws module	From[71]
q''	8.21 kW/m^2	-	10.09%	Measured	Calculated

The supplied values are almost entirely those which have been determined in the preceding sections. The resulting $\theta_{w,x}$, Nu_x, and, the associated uncertainty is presented in Table 3.21 and the UPCs are shown in Figure 3.22.

Table 3.21: Resulting $\theta_{w,x}$, Nu_x, and uncertainty b_X

x/L	$\theta_{w,x}$	b_X
0.75	13.66 K	4.27 K
0.50	15.13 K	4.09 K
0.25	11.63 K	4.17 K
	Nu_x	b_X/X
0.75	135.9	32.91%
0.50	82.0	28.88%
0.25	53.9	37.31%

It may be seen that for $\theta_{w,x}$ the UPCs are dominated by the wall temperature measurement as to be expected.

Upon inspection of Table 3.20, the uncertainty for $\theta_{w,x}$ doesn't seem much different to a standard K-type thermocouple measurement (typically 2.2 K or 0.75%, whichever the greater). For

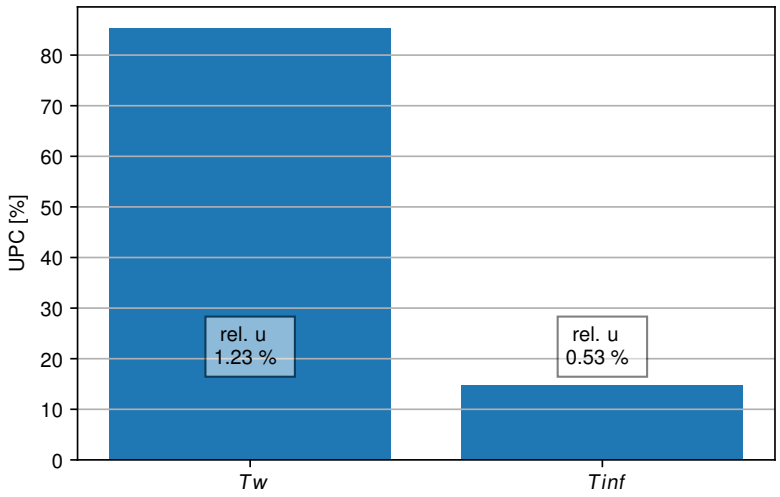

Figure 3.21: UPCs for $\theta_{w,x}$ at $x/L = 0.50$, the relative uncertainty for each variable is annotated.

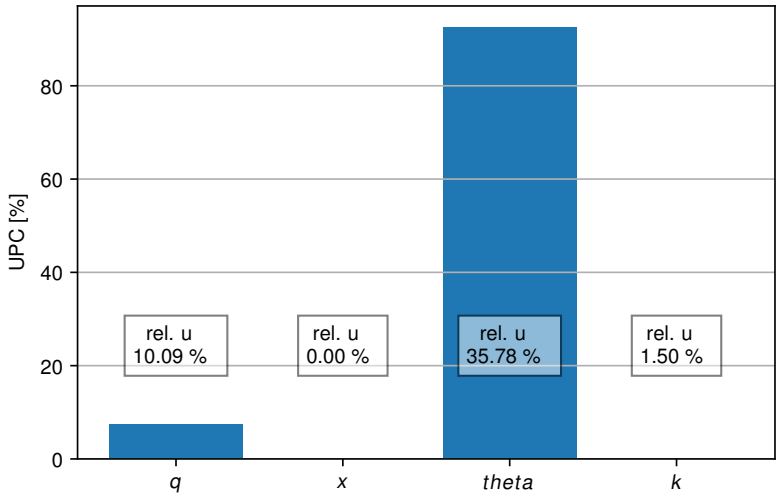

Figure 3.22: UPCs for Nu_x at $x/L = 0.50$, the relative uncertainty for each variable is annotated.

a temperature *difference* the relative uncertainty will be much greater. This is because $\theta_{w,x}$ and its systematic uncertainty are close in value. For Nu_x, it is therefore unsurprising that the UPCs are dominated by $\theta_{w,x}$. Efforts to reduce the uncertainty should focus on the surface temperature measurement in the first instance.

A similar formulation of average Nusselt number is also of use;

$$\overline{Nu}_L = \frac{q'' L}{(\theta_{\infty,L/2})k} \tag{3.25}$$

where $\theta_{\infty,L/2}$ is the wall excess temperature at the mid height. The uncertainty from this formulation is negligibly different from that for Nu_x as both equations have equal dependence on the wall temperature measurement.

3.5.6 Verification

In this section the experimental conditions are compared against the correlations for a vertical heated surface introduced in section 2.1. The local modified Rayleigh number Ra_x^* and local Nusselt number Nu_x are plotted alongside correlations for laminar and turbulent flow in Figure 3.23.

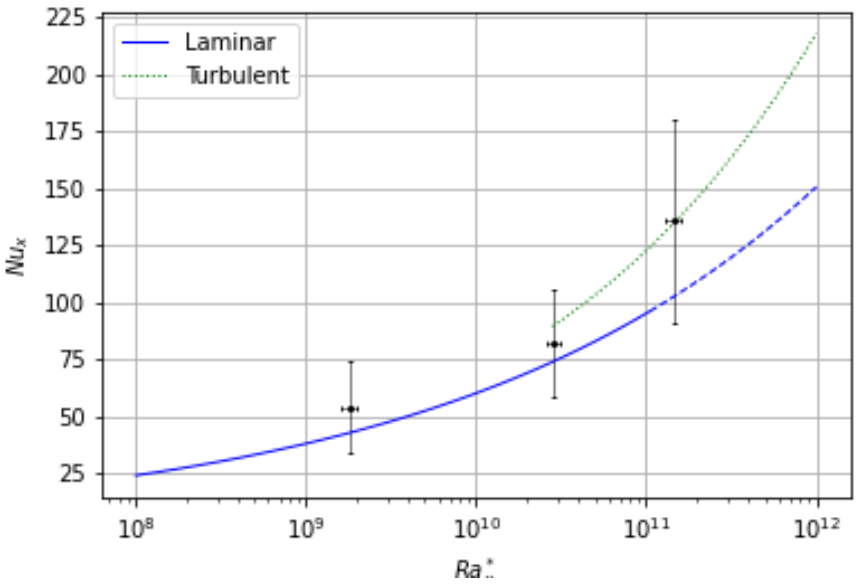

Figure 3.23: Plot of the experimentally measured local modified Rayleigh number Ra_x^* (eqn (3.19)) and local Nusselt number Nu_x (eqn (3.24)). The laminar correlation is given by eqn (2.15) and the turbulent by eqn (2.16). The turbulent correlation is used entirely outside of its reported range. The dashed blue line represents the use of the laminar correlation beyond its reported range.

The laminar correlation is reportedly only valid upto $Ra_x^* \approx 10^{11}$ and an extension beyond this range is shown by the blue dashed line. Thus, the first two data points should be expected to be in broad agreement. The relatively large uncertainty in the local Nusselt number makes it difficult to be definitive, but there appears to be general agreement with the correlated values lying within

the range of uncertainty. There are several explanations for a discrepancy between the measured and correlated values beyond measurement error. The two most likely being:

1. The leading edge of the heater is a sharp corner which may induce flow disturbances and result in increased, or the early onset of, turbulence. An increasingly turbulent flow would be expected to yield an increased local Nusselt number due to the improvement in heat transfer performance. This increase is typically localised to the entrance region re-laminarisation at some distance down stream.
2. The thermal stratification in the present experiment is reasonably large at $\approx 7.5\,^{\circ}\text{C}$. The presence of thermal stratification is also known to increase the heat transfer performance[25]. Here this would manifest as a reduced wall excess temperature and thus a larger local Nusselt number.

The rightmost data point falls outside the reported ranges of the correlations given by equation (2.15) and (2.16). The lack of available correlation is likely due to the flow transitioning to turbulence in this region. For comparison, a plot (green dotted line) for a turbulent correlation (extended beyond its reported range) is shown which has excellent agreement with the nominal value. Since the flow is likely transitioning to turbulence, rather than turbulent, the correlation is not strictly valid. Despite this one would expect the value to be indicative.

In Figure 3.24 the channel averaged Rayleigh number Ra_L is compared to a correlation by Churchill and Chu[16], as reported in Hewitt[7]. The correlation is reported without a range of applicability except to say it is applicable to laminar and turbulent conditions. Here the uncertainty is much reduced and excellent agreement is shown. The Ra_L is greater than 10^9 where transition is thought to begin; thereby supporting the conclusion that the experimental conditions are not laminar.

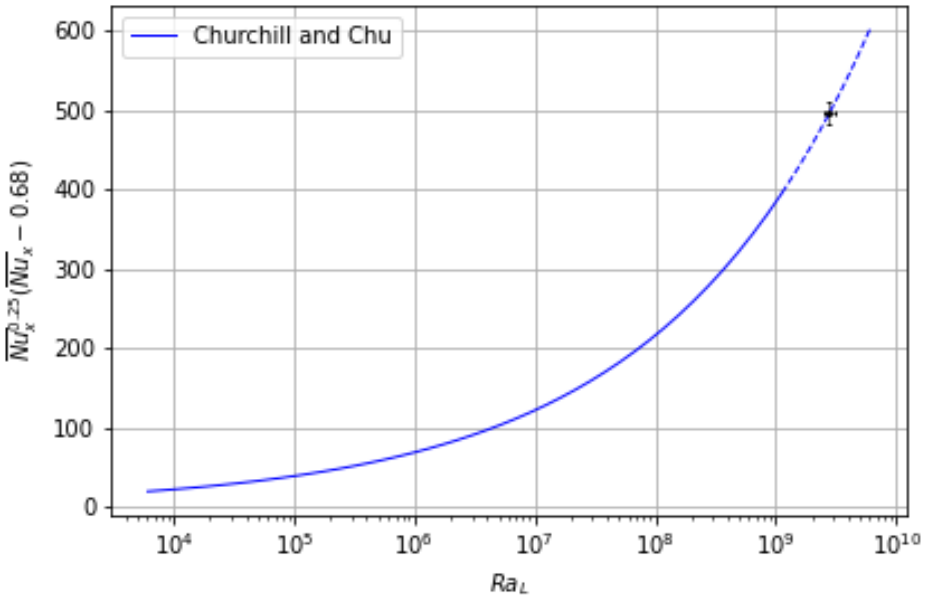

Figure 3.24: Comparison of the measured channel Rayleigh number Ra_L and Churchill and Chu [16] correlation eqn (2.17). The dotted line shows where the correlation is assumed to be beyond the range of applicability.

3.6 Experimental conditions

The apparatus is capable of producing a range of experimental conditions dependent upon the supplied power and the configuration; surface or channel, open or closed. For the surface geometry considered here the nominal experimental conditions are presented in Table 3.22.

With regards to the ability to reproduce the experimental flow conditions and determination of the random uncertainty, Figure 3.25 shows the variation in Rayleigh and Nusselt numbers. The variation (r') is calculated using

$$r' = 100 \times \frac{r - \bar{r}}{\bar{r}}$$

where r is the time variant quantity e.g. Ra_x^*. It may be seen that the flow conditions typically had $< \pm 1\%$ variation over both measurements and are thus assumed to maintain a steady state through both measurements.

Table 3.23 shows the nominal conditions averaged over the PIV+BOS and BOS@PIV measurements inclusive of the random uncertainty contribution i.e. the overall uncertainty. It may be seen that the uncertainty is negligibly increased for the Rayleigh number, and is increased by $\approxeq 3\%$ for the Nusselt number as compared to those shown in Table Table 3.22.

Table 3.22: Nominal experimental conditions and the corresponding systematic uncertainty

Property	Nominal value
q''	$8.21\,\mathrm{kW/m^2} \pm 10.1\%$
ΔT_{strat}	$7.76\,^{\circ}\mathrm{C}$
T_{in}	$21.1\,^{\circ}\mathrm{C} \pm 2.2\,^{\circ}\mathrm{C}$
$T_{\infty,x}$	$T_{in} + (x/L)\Delta T_{strat}$
Pr_{∞} at $x/L = 0.50$	6.13
$Ra_L = Ra_L^*/\overline{Nu}_L$	$1.884 \times 10^9 \pm 10.36\%$
Ra_L^*	$4.211 \times 10^{11} \pm 10.36\%$
Ra_x^* at $x/L = 0.75$	$1.359 \times 10^{11} \pm 10.36\%$
Ra_x^* at $x/L = 0.50$	$2.684 \times 10^{10} \pm 10.37\%$
Ra_x^* at $x/L = 0.25$	$1.677 \times 10^9 \pm 10.39\%$
$\overline{Nu}_L$	$223.6 \pm 38.79\%$
Nu_x at $x/L = 0.75$	$135.9 \pm 32.91\%$
Nu_x at $x/L = 0.50$	$82.0 \pm 28.88\%$
Nu_x at $x/L = 0.25$	$53.9 \pm 37.31\%$

Table 3.23: Nominal experimental conditions and the corresponding overall uncertainty

Property	Nominal value
q''	$8.21\,\mathrm{kW/m^2} \pm 10.19\%$
ΔT_{strat}	$7.76\,^{\circ}\mathrm{C}$
T_{in}	$21.1\,^{\circ}\mathrm{C} \pm 2.2\,^{\circ}\mathrm{C}$
$T_{\infty,x}$	$T_{in} + (x/L)\Delta T_{strat}$
Pr_{∞} at $x/L = 0.50$	6.13
$Ra_L = Ra_L^*/\overline{Nu}_L$	$1.884 \times 10^9 \pm 10.36\%$
Ra_L^*	$4.211 \times 10^{11} \pm 10.36\%$
Ra_x^* at $x/L = 0.75$	$1.519 \times 10^{11} \pm 10.37\%$
Ra_x^* at $x/L = 0.50$	$2.632 \times 10^{10} \pm 10.37\%$
Ra_x^* at $x/L = 0.25$	$1.496 \times 10^9 \pm 10.40\%$
$\overline{Nu}_L$	$223.6 \pm 38.79\%$
Nu_x at $x/L = 0.75$	$137.2 \pm 33.19\%$
Nu_x at $x/L = 0.50$	$111.8 \pm 38.79\%$
Nu_x at $x/L = 0.25$	$57.7 \pm 40.27\%$

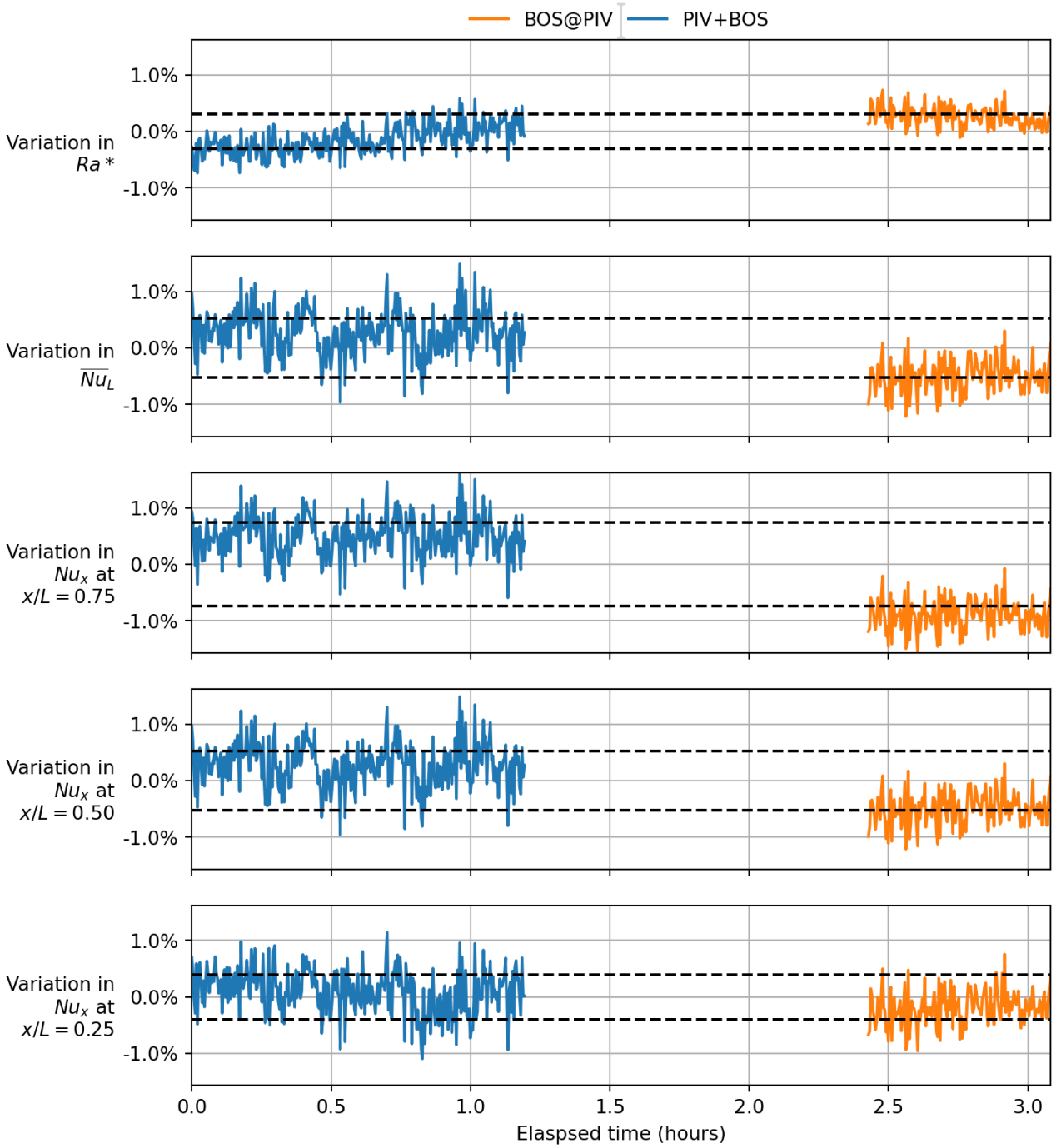

Figure 3.25: Variation in Rayleigh and Nusselt numbers during measurements of PIV+BOS and PIV@BOS. The Rayleigh number shown is Ra^*_L and the dashed lines show one standard deviation.

3.7 Summary

In this chapter the apparatus and ancillary equipment have been described. The typical experimental conditions have been summarised in Table 3.22 and the ancillary instrumentation is tabulated in Table 3.6.

A detailed uncertainty analysis has found that the local modified Rayleigh number and channel Rayleigh are achieved with relative uncertainty in the vicinity of 10%. The conditions are verified by determination of the Nusselt number where it is shown that the flow conditions are consistent with a surface transitioning to turbulence.

Uncertainty in the measurement of the experimental conditions is primarily the result of uncertainty in the determination of the surface heat flux and temperature. The uncertainty could be reduced through the use of a higher resolution DAQ module for voltage measurements and calibration of thermocouples against a standard reference measurement.

A thermal stratification is present and of the order $7.5\,^{\circ}$C. The effect of this may be causing a delayed transition to turbulence and increased heat transfer performance than would be expected from an isothermal quiescent region.

Chapter 4

Methodology

Thermally induced refractive distortion occurs due to gradients in the refractive index (n) i.e. ∇n. The PIV+BOS apparatus is illustrated in Figure 4.1. In Figure 4.1a the refractive index gradient due to thermal stratification is shown in red/blue i.e. $\frac{\partial n}{\partial x}$. Similarly, in Figure 4.1b the refractive index gradient due to a wall-normal heat transfer induced thermal gradient is shown in orange i.e. $\frac{\partial n}{\partial y}$. It may be seen that the red/blue gradient also varies in opacity in the wall-normal direction. This is to represent the combined effects of thermal stratification and heating on the refractive index.

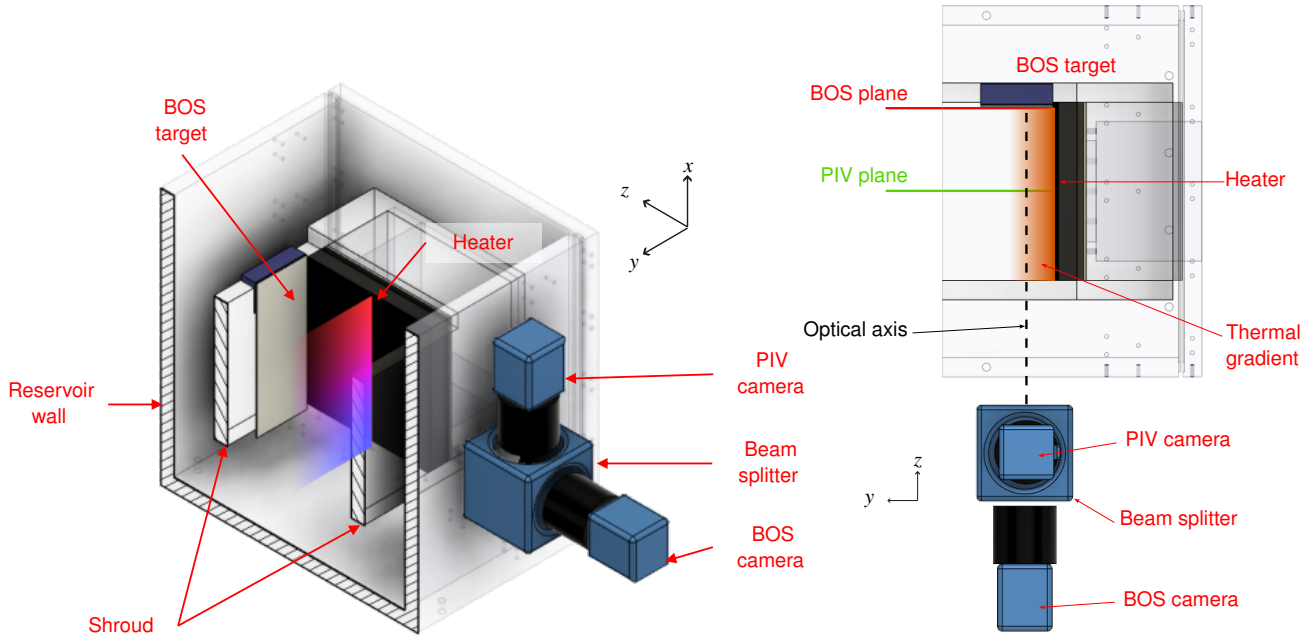

(a) (b)

Figure 4.1: PIV+BOS apparatus, (a) perspective view, (b) top-down view. The red/blue gradient in (a) represents the density gradient due to thermal stratification. The orange gradient in (b) adjacent to the heater represents the density gradient due to heat transfer.

Unprocessed BOS and PIV images are shown in Figure 4.2. Figure 4.2a shows an image of a BOS target located at the BOS plane with no heating applied i.e adiabatic conditions. The same

target is shown in Figure 4.2b at the experimental conditions with heating applied. Similarly, Figure 4.2c shows a PIV measurement with heating applied. Both measurements with heating applied exhibit similar features i.e. streaks. These streaks are caused by, and characteristic of, refractive distortion. The streaks are caused by extreme astigmatism which results from light being refractive in a variable refractive index region i.e. the fluid within the thermal boundary layer. The orientation of the streaks is related to the gradient of the refractive index. In the present application the streaks appear predominantly horizontal. This is due to the relatively high heat flux ($q'' \cong 8.21\,\mathrm{kW/m^2}$). Hence, the thermal gradient due to heating yields a more significant refractive distortion than that from the thermal stratification i.e.

$$\frac{\partial n}{\partial y} >> \frac{\partial n}{\partial x} \tag{4.1}$$

The effects of blur are quite apparent in Figure 4.2 but it is difficult to see the displacement by eye. The determined reader can observe the apparent position of the edge of the BOS target appears shifted leftward and towards the top of the image and even appears very slightly curved. Also apparent on Figure 4.2b, about two thirds up the image, is a dark region which under closer inspection can be recognised as a bubble sat on the target. Bubbles such as these are caused by non-condensible gases which nucleate when the fluid is warmed. If the bubble remains in the same location during a measurement it will result in a region of very high distortion (since it wasn't present in the reference image). The approach to determining the scaling factor is actually quite tolerant to such bubbles but they can result in localised data loss and are ideally avoided.

Upon first inspection of Figure 4.2c one might suspect inhomogeneous seeding. However, this is not the case and the relatively dark region in the upper right portion of the image is the result of refraction. Figure 4.3 shows a zoomed portion of a typical raw PIV image near to a heated surface (located to the left in this image). Several features may be seen. Starting rightmost in the image, the seeding particles appear slightly larger due to a magnification of the image caused by the distortion forming a pseudo liquid lens. Moving leftward, closer to the heater and thus with greater distortion, particle astigmatism may be observed. Here a normally circular particle image is observed as an ellipse with the semi major axis in the direction of the density gradient i.e. normal to the heating surface. Immediately adjacent to the surface (leftmost in the image) the particles image become increasingly blurred.

In the highly blurred region it becomes impossible to distinguish a blurred particle image from the noise of the blurring and reflections (which are also distorted). An important finding of these observations is that the very near wall flow is actually distorted towards the surface to the point that it is located in a position which would appear to be inside the surface. The implication is that any processing masks (which would typically be employed to remove reflected particle images) must cover some arbitrary amount of the heater surface if the near wall fluid is to be recovered by correction. A further implication is a lack of certainty as to where the heating surface is located which will be seen in chapter 5.

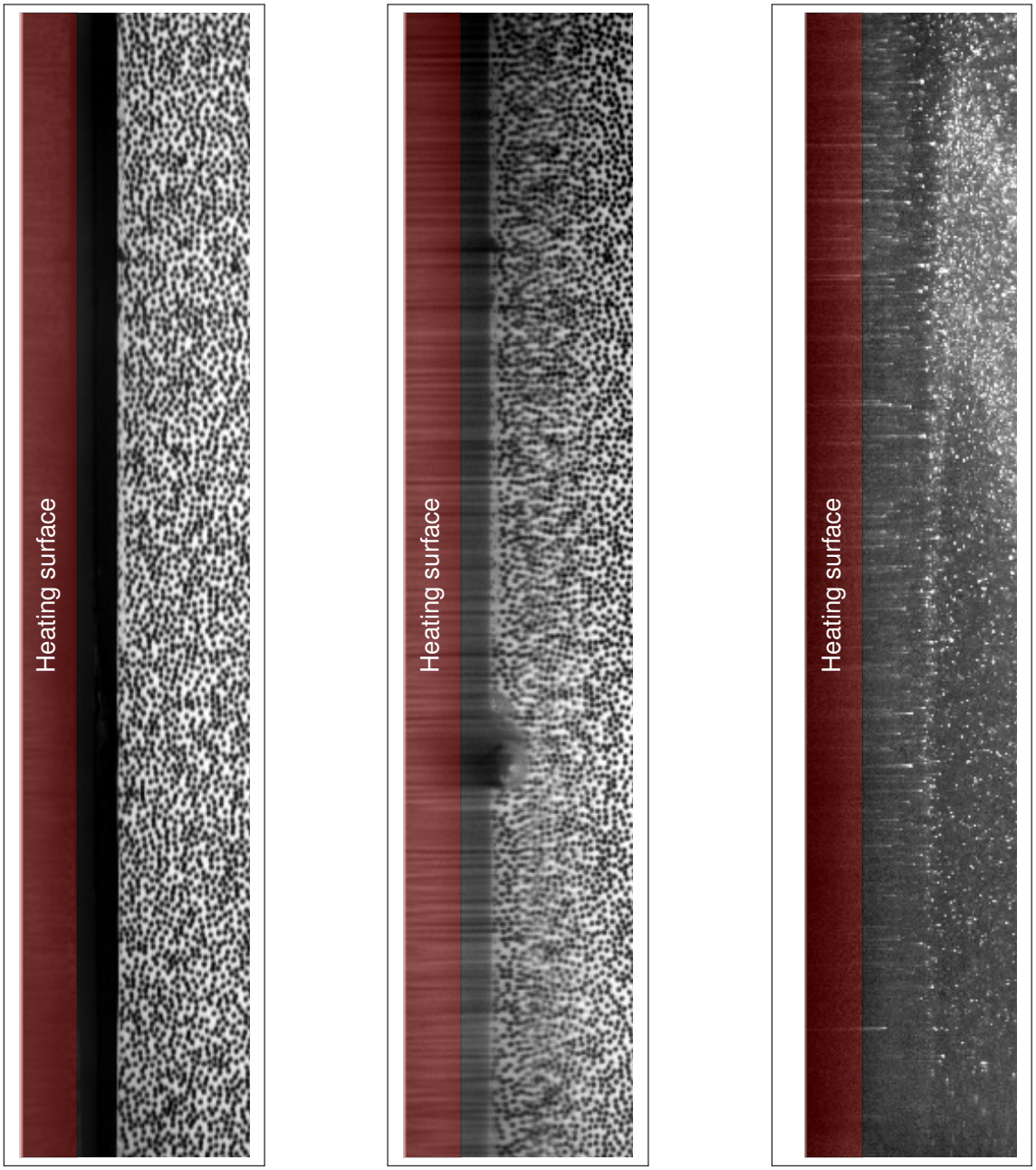

(a) (b) (c)

Figure 4.2: Raw (a) BOS reference, (b) BOS measurement, and (c) PIV measurement images. The heating surface is to the left.

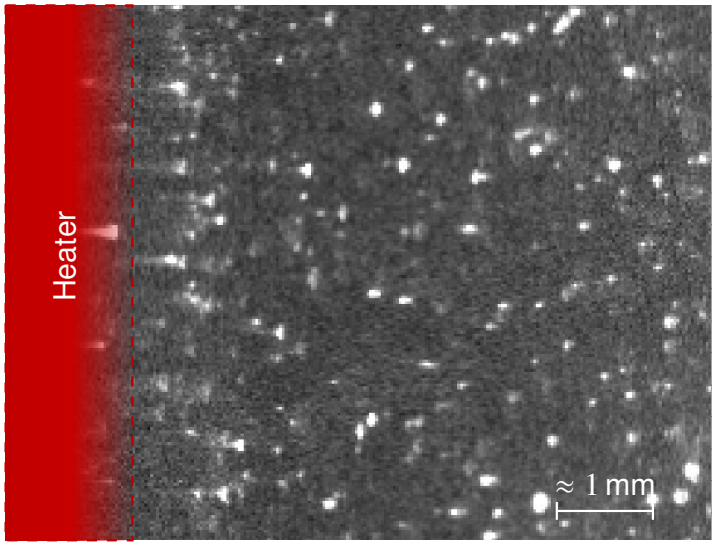

Figure 4.3: Astigmatism of raw seeding particle images. The heater is located to the left with the approximate atrue surface location defined by the dashed line.

A fundamental assumption of the methods to be developed in this chapter is that the refractive index does not vary in the z-direction i.e. $\frac{\partial n}{\partial z} \approx 0$ and hence

$$\nabla n \cong \frac{\partial n}{\partial x} + \frac{\partial n}{\partial y} \tag{4.2}$$

This assumption is based on producing a pseudo 2D flow (which the apparatus is designed to do). This is important because it implies the thermal boundary layer thickness remains approximately constant in the z-direction for a uniformly heated surface. As the geometry, heating arrangement and flow (i.e. turbulence) become more complex the methodology developed becomes less applicable since $\frac{\partial n}{\partial z} \neq 0$ in those cases.

There are three considerations to address:

1. How the resulting measurements of distortion should be applied i.e. the BOS correction process.
2. How to account for differences in optical path length in the refracted fluid between the PIV and BOS plane i.e. defining a scaling factor.
3. How to account for differences in calibration conditions for PIV and BOS.

Each of these will be discussed in turn within this chapter. The pertinent equations to describe optical distortion are developed in Appendix A.

4.1 BOS correction process

Optical distortions, aside from the specific case of thermally induced refractive distortion, are commonly encountered when performing optical measurements. These can originate from many

sources, for example:

- The optical path between camera and plane of interest may include several different transparent media. If the viewing angle is oblique the image will be refracted. The severity of the resulting distortion is dependent on the refractive indices of adjacent media.
- A further distortion introduced by oblique viewing is the magnification of objects nearer to the lens. This is typically called parallax or perspective distortion.
- If the plane of interest is viewed through a surface that is not perfectly flat then the image will be distorted due to refraction and the curvature of the surface.
- Due to their shape, lenses can also introduce distortion towards the outer edges of the image. This is typically called cushion or barrel distortion.
- Optical components between the image sensor and the plane of interest such as lenses and filters etc may not be perfectly aligned and thus introduce distortion.

The listed sources of distortion differ from the thermally induced refractive distortion considered in this work in two significant attributes:

1. The listed sources of distortion are time-independent
2. The listed sources of distortion are reasonably well approximated by a 3rd order polynomial surface.

It is instructive to briefly summarise how the time-independent distortions are corrected as there is some similarity to the method proposed for the correction of the thermally induced refractive distortion.

A standard activity when performing PIV measurements is to perform an optical calibration[29]. This is usually performed only once and occurs after the instrumentation and apparatus have been set up[1]. The calibration is performed by imaging a precisely patterned target with known spacings which is located at the PIV plane, as shown in Figure 4.4. The conditions for the calibration should be similar to the experimental conditions with the correct fluids and interfaces present, and at similar temperatures. The calibration images are then used to perform two functions:

1. To enable determination of the real world to image sensor mapping such that the velocity may be reported in scaled units such as mm/s rather than px/s, for example.
2. To map any time-independent distortion.

When the PIV images are post-processed usually one of the first operations to be applied is the transformation of the raw images using the mapping function determined by optical calibration.

The method for correcting the thermally induced refractive distortion is akin to performing an optical calibration of each instantaneous PIV image. As each PIV image is recorded a corresponding BOS image is recorded simultaneously. Unlike the optical calibration, the post-processed BOS measurements produce a vector field of distortion, rather than a mapping function. This distortion

[1] In principle the calibration can occur at any time during an experimental campaign.

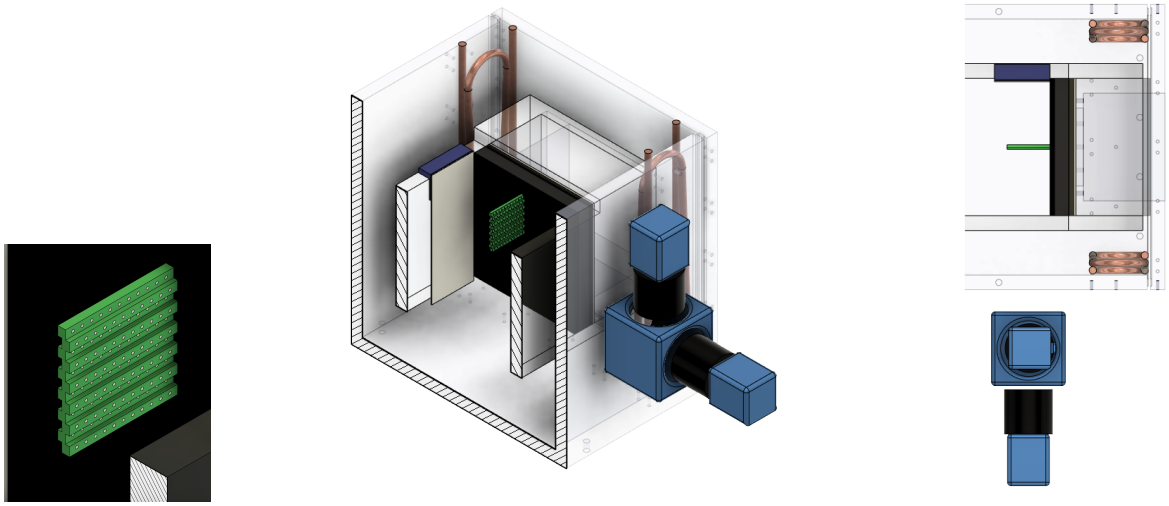

(a) (b) (c)

Figure 4.4: Illustration of a calibration target located in the PIV plane. (a) Calibration target (green), (b) perspective view, (c) top-down view

field is not constrained to a polynomial fit and can be processed to have the same, or similar, spatial discretisation as the post processed PIV vector field. One complicating factor is that the BOS target, unlike the calibration target used in an optical calibration, is not coincident with the PIV plane. Thus, the measured distortion must be appropriately scaled before it can be used to transform the PIV images. A final consideration is the order of operations with respect to the optical calibration and the BOS correction. If no optical calibration were performed the BOS correction could conceivably correct for the time-independent distortions. However, the optical calibration is still required to provide the real world to image sensor mapping. The PIV processing software, DaVis 10.2, combines the real world mapping and correction of time-independent distortion, it is necessary to apply an optical calibration to the PIV and BOS images first, and then apply the BOS correction.

For clarity the major stages of the BOS correction method are listed as follows:

1. Gather optical calibration images.
2. Simultaneously gather PIV and BOS images.
3. Apply mapping function to PIV and BOS images.
4. Post-process the BOS images to yield the distortion vector field.
5. Scale the distortion vector field.
6. Correct the optically calibrated PIV images.
7. Post-process the PIV images to yield velocity and turbulence vector fields.

4.2 Scaling factor

In concept the scaling factor represents the relationship between refractive distortion at the BOS and PIV planes. In the previous work of Elsinga et al.[52], the scaling factor was defined as a function of the relative distance travelled through the variable refractive index field to the BOS and PIV planes; W_{BOS} and W_{PIV}, respectively. These are shown on Figure 4.5.

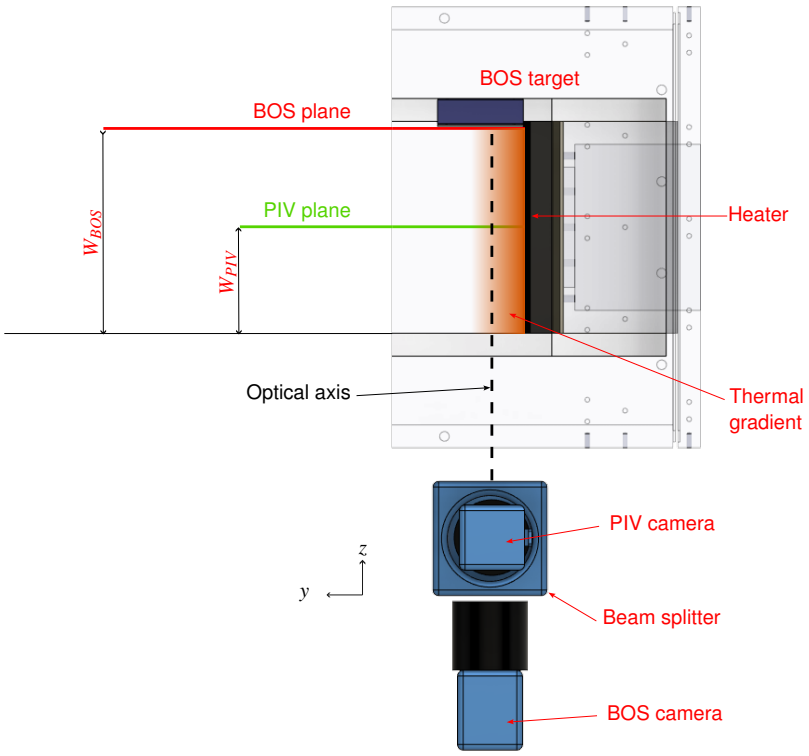

Figure 4.5: Illustration of W_{PIV} and W_{BOS}

The authors defined an analytical scaling factor by derivation of equations for the displacement of a light ray due to the presence of a gradient in refractive index to yield:

$$\xi_e = \xi_0 + \left[\frac{W^2}{2}\right]\frac{1}{n_0}\frac{\partial n}{\partial x} \tag{4.3}$$

$$\zeta_e = \zeta_0 + \left[\frac{W^2}{2}\right]\frac{1}{n_0}\frac{\partial n}{\partial y} \tag{4.4}$$

$$\Delta\xi = \left[\frac{W^2}{2}\right]\frac{1}{n_0}\frac{\partial n}{\partial x} \tag{4.5}$$

$$\Delta\zeta = \left[\frac{W^2}{2}\right]\frac{1}{n_0}\frac{\partial n}{\partial y} \tag{4.6}$$

The displacement in the x and y directions are ξ and ζ, respectively. The subscript 0 e.g. ξ_0 refers to displacement of light upon entry to the region of variable refractive index i.e. a location on the BOS target. The subscript e e.g. ξ_e refers to the displacement upon emerging from this region i.e. what the camera will see. Since the difference is the property of interest these are replaced

with $\Delta\xi$ and $\Delta\zeta$. They defined a scaling factor as

$$A = \frac{W_{PIV}^2}{W_{BOS}^2} \tag{4.7}$$

and assume that $W_{PIV} = W_{BOS}/2$ to yield a scaling factor of $A = 0.25$. In the derivation of these equations the authors assume perfectly perpendicular alignment of camera and target, perfect camera alignment between PIV and BOS images, perfect alignment of the PIV plane at $W_{PIV} = W_{BOS}/2$. In practice, achieving such perfection is difficult as demonstrated in earlier work by the same authors; Elsinga et al.[72], whereby systematic errors in each of those assumptions resulted in systematic errors in the BOS results.

In this work a novel experimental approach is used to determine the scaling factor. In addition to the BOS recordings performed at the PIV plane for the simultaneous PIV+BOS measurements, a separate set of BOS recordings are taken at the PIV plane (as seen previously in Figure 3.3). For clarity, these measurements are referred to as BOS conducted at the BOS plane (BOS@BOS) and BOS conducted at the PIV plane (BOS@PIV). These recordings are performed under the same experimental conditions and with the same camera (with the focus adjusted to the PIV plane). There are two major assumptions for this approach.

1. The introduction of a BOS target at the PIV plane does not substantially alter the refractive distortion.
2. Aspects relating to scaling between the two planes are not time dependent.

The first assumption seems reasonable due to the target being located at $W_{PIV} \cong W_{BOS}/2$ and the heating surface being sufficiently wide to produce a pseudo 2D flow either side of the BOS target. The benefit of the second assumption is that the scaling factor may be determined by comparing the time averaged distortion fields from the BOS and PIV planes.

The scaling factor in this work is intended to be *summative* rather than multiplicative as was the case in Elsinga et al.[52]. This is to account for the effect of imperfect alignment between the camera and BOS targets. If such a misalignment were included in the displacement equations derived by Elsinga et al.[52] then eqns (4.5) and (4.6) would include an additional term: (adapted from eqn (A.24) in Appendix A)

$$\Delta\xi = W \tan\phi_0 + \left[\frac{W^2}{2}\right]\frac{1}{n_0}\frac{\partial n}{\partial x} \tag{4.8}$$

$$\Delta\zeta = W \tan\psi_0 + \left[\frac{W^2}{2}\right]\frac{1}{n_0}\frac{\partial n}{\partial x} \tag{4.9}$$

where the angles ϕ_0 and ψ_0 relate to the misalignment of the optical axis with the z-direction (defined as perpendicular to the BOS target and parallel to the heating surface).

In order to distinguish from the multiplicative scaling factor; A, defined by Elsinga et al.[52], the summative scaling factor defined herein uses the symbol κ. Similarly, to simplify notation the

vector field of displacements $\vec{\xi}$ and $\vec{\zeta}$ are described by a single variable λ which refers to a single post-processed BOS vector field. Since BOS measurements are performed at the PIV and BOS planes, the displacement vector fields at these planes are defined as λ_{PIV} and λ_{BOS}, respectively.

Fluctuations in the thermal boundary layer require that the BOS measurements at the PIV plane be recorded over a long period to determine a reasonable approximation of the time averaged distortion. The recording parameters were used for BOS measurements at the PIV and BOS planes i.e. 5000 images over 333.33 s. The time averaged distortion fields; $\overline{\lambda}_{BOS}$ and $\overline{\lambda}_{BOS}$, are thus single vector fields defined by

$$\overline{\lambda} = \frac{1}{N}\sum_{i=1}^{N}\lambda_i \tag{4.10}$$

where N is the number of instantaneous images and λ_i is an instantaneous distortion field of the set $\{\lambda_1, \lambda_2, ..., \lambda_N\}$. A plot of $\overline{\lambda}_{PIV}$) and $\overline{\lambda}_{BOS}$ is shown in Figure 4.6. It may be seen that the distortion is qualitatively similar but the magnitude of displacement is quite different. Also apparent is that no singular constant value could be applied to the field at the BOS plane Figure 4.6b to yield that at the PIV plane Figure 4.6a.

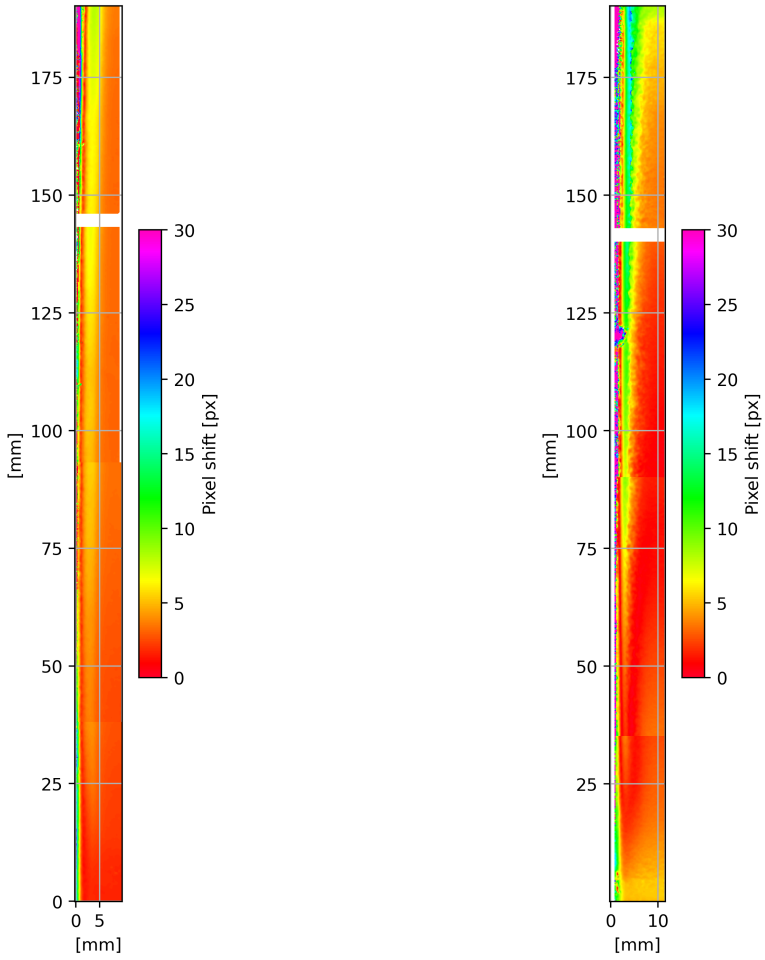

Figure 4.6: Time averaged distortion fields at the (a) PIV plane ($\overline{\lambda}_{PIV}$) and (b) BOS plane ($\overline{\lambda}_{BOS}$)

Since the distortion fields are vector fields, the scaling and subsequent correction of these fields

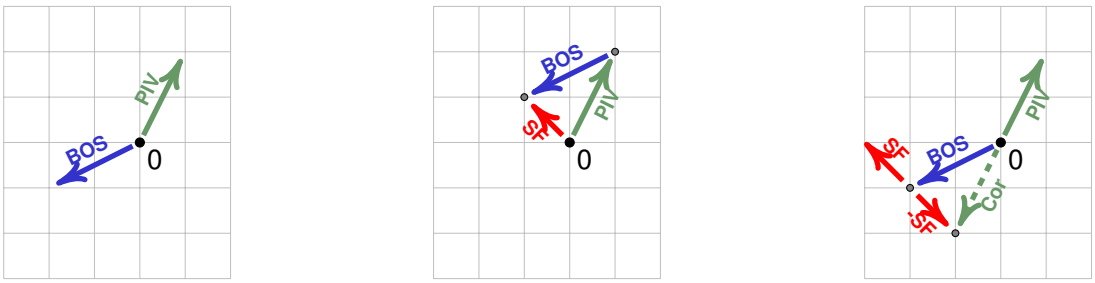

(a) (b) (c)

Figure 4.7: The labels BOS, PIV, SF, Cor and 0 refer to $\overline{\lambda}_{BOS}$, $\overline{\lambda}_{PIV}$, κ, λ^*_{BOS} and the origin, respectively. Illustrated in (a) a single vector from $\overline{\lambda}_{BOS}$ and $\overline{\lambda}_{PIV}$, (b) the determination of the scaling factor as per eqn. (4.11), and (c) the correction vector as per eqn. (4.12)

must be performed accordingly. For simplicity the vectors relating to a single location are depicted in Figure 4.7. Figure 4.7a shows the comparison of a single vector at equivalent locations in the time averaged PIV and BOS distortion fields, $\overline{\lambda}_{PIV}$) and $\overline{\lambda}_{BOS}$. The scaling factor (labelled SF) in Figure 4.7b is shown to be the sum of the time averaged PIV and BOS distortion fields, i.e.

$$\kappa = \overline{\lambda}_{PIV} + \overline{\lambda}_{BOS} \tag{4.11}$$

This definition is not immediately intuitive until it is shown in context in Figure 4.7c. Here it may be seen that the scaling factor is subtracted from a BOS vector. In doing so one defines the correction vector that must be applied to the PIV image to correct for distortion. The *scaled instantaneous* distortion field, with symbol λ^*_{BOS}, is defined as

$$-\lambda^*_{BOS} = \lambda_{BOS} - \kappa \tag{4.12}$$

It must be noted that λ^*_{BOS} represents the distortion in the PIV imagery and thus its conjugate is the correction that must be applied. Hence the correction field, required to deform the PIV imagery, is given by $-\lambda^*_{BOS}$, as depicted by the vector labelled *cor* in Figure 4.7c.

4.2.1 Processing

The processing of PIV and BOS images was primarily conducted using DaVis 10.2 software[30] with additional calculations made in python scripts. The BOS process diagram is shown in Figure 4.8.

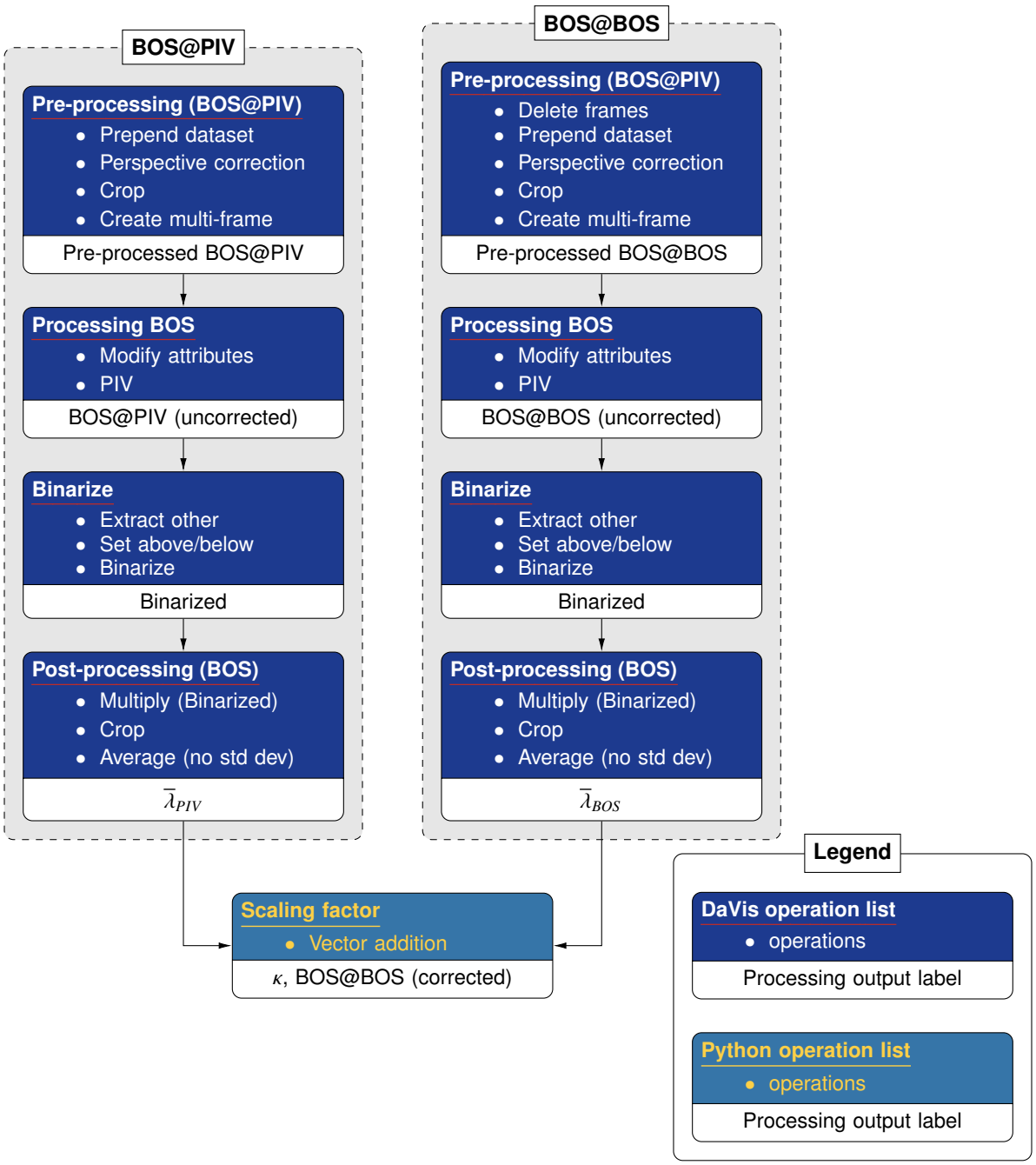

Figure 4.8: BOS processing diagram

A DaVis operation list is a user defined group of operations that are available in the software[30]. The processing was divided into such groupings in part because, without performing coding in the native DaVis programming language, it was necessary to first calculate some result (e.g. the binarized output) which would then be used in the next operations. Conceptually, with the correct internal programming, there is no need to produce an output from any of these intermediary steps. However, having such intermediary information is quite useful in that it allows for easier debugging, natural break points to trial different processing strategies, and the potential for verification.

The BOS calculations were performed using the PIV processing algorithms in DaVis. To accomplish this the BOS images have to be presented in a way which is compatible with how PIV data

would be presented. This was achieved with the following operations (as they are named in the software):

Delete frames - (BOS@BOS only) This is used to remove the simultaneously gathered PIV image from the dataset.

Prepend dataset - The BOS reference image is prepended to the dataset

Perspective correction - Here the optical calibration is applied and the images are scaled from pixels to mm. Due to the mounting of the calibration target this has the undesired effect of rotating the field of view by $180°$. It was later discovered that this could be corrected by rotating the calibration result, but much of the data had been processed by this point.

Crop - The field of view is reduced to speed up calculation. This reduction makes a considerable difference to the total processing time. The image is cropped back to approximately just beyond the apparent boundary layer thickness which is determined from previous measurements. Since the position of the heating surface is highly distorted and obscured by blur, the image is cropped conservatively near to the surface such that some reflection is present and will need to be removed subsequently.

Create multi-frame - Re-order the dataset such that the prepended reference image is paired with an instantaneous BOS image. Thus the reference image will act as the initial PIV image and the BOS image the second in a double frame PIV calculation. Hence the resulting vectors will represent the distortion with respect to the reference. As a note, changing the order of these image pairs would reverse the direction of the vector field which can easily be corrected by a scalar multiplication of the field by a constant -1.

The output is a set of BOS data ready for input into a PIV algorithm.

This is subsequently used as input for BOS processing, which comprises:

Modify attirbutes - DaVis uses the image timestamp meta data imprinted during data collection as part of the PIV algorithm. The difference in time between each image timestamp is used alongside the determined displacement to calculate a velocity. Whilst this is appropriate for PIV calculations it is problematic here. This is because the BOS reference and measurement images were recorded several days apart. When converted to a velocity this would yield extremely slow velocities which, if uncorrected, causes issues with other processing operations. Thus, this step modifies the time stamps to have a value of 0 and 1 for the reference and instantaneous image, respectively. Despite making this modification some operations such as basic vector algebra exhibited strange behaviour which is why python is used to perform some of these functions.

PIV - This is the operation which defines the parameters for the PIV algorithm e.g. mode, window size, passes etc as described in previous sections.

The output is λ; a set of vector fields representing the distortion of the BOS target. This dataset is later corrected once the scaling factor has been determined but is also used in its determination.

The calculated vector field includes erroneous vectors near to the heated surface due to blurring

and reflection. It is thus necessary to attempt to identify and omit these erroneous vectors. In addition, this process identified and omitted erroneous vectors due to the presence of bubbles and debris. Identifying erroneous vectors is a common post process for PIV results and often uses some measure of the peak map to decide which vectors are good or bad. Here, best qualitative performance was achieved by using the calculated particle size. This is a feature intended to estimate the size of particles in a PIV image. Since the BOS target is a printed dot pattern similar to particle images the operation also performs well here. Where the image became increasingly blurred the particle size would tend to zero, similarly in the presence of bubbles. Thus a filter based on particle size which omitted increasingly larger values would be more conservative. Here a value of 2 px was used which was a compromise erring on the side of conservatism. Thus the binarize operation list comprised:

Extract other - This operation extracts the particle size scalar field from the calculated BOS dataset.

Set above/below - This sets locations with a particle size below the cut off to 0 and above to 1. However the output in some regions is not integer

Binarize - explicitly sets all regions to either 0 or the integer value 1

The BOS post-processing is a preparation for calculating the scaling factor and comprises:

Multiply (Binarized) - This operation multiplies the λ dataset with the binarized output to omit vectors. Ideally this operation would've been a masking operation but that option was not available.

Crop - With a better idea of where the surface was located the image could be cropped back a little further. This was also necessary for the vector algebra which followed that requires both the BOS@PIV and BOS@BOS data have the same number of vectors i.e. field of view.

Average (no std dev) - This process determines an average vector field based on the now filtered and cropped λ dataset.

The output of BOS post-processing is $\overline{\lambda}$; the time averaged distortion field for either the PIV or BOS planes as defined by the subscript.

The calculation of the scaling factor (κ) and the corrected distortion field (λ^*_{BOS}) is a simple vector addition. As previously mentioned some of these basic functions did not perform well either through the internal use of metadata by DaVis or due to encountering niche bugs that would occur during normal processing of PIV.

It was therefore easier to perform the determination of the scaling factor and correct λ in python. This was made possible by the recent release of a python module which allows native DaVis file types for images and vector fields to be parsed into masked *numpy*[2] arrays. Similarly, the reverse process of converting a masked array into the native file format is provided such that the python results can be put back into the DaVis software to make use of the more advanced processing

[2]Numpy is a python package dedicated to numerical and mathematical operations.

features provided therein.

The PIV process diagram is shown in Figure 4.9.

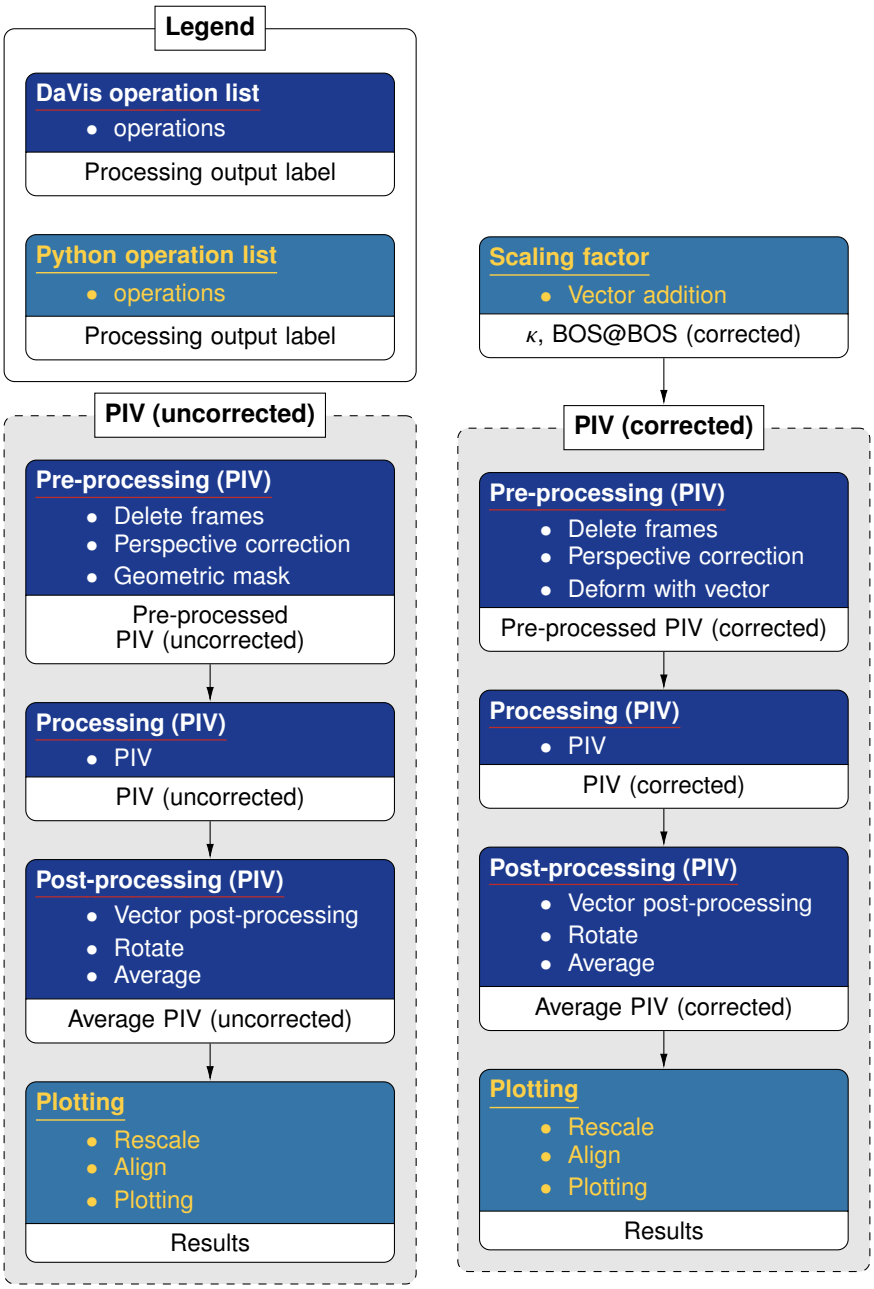

Figure 4.9: PIV processing diagram

The *PIV (uncorrected)* flow process refers to the case where BOS correction is not applied and PIV is performed without consideration of the distortion and thus takes as input the raw PIV images. The *PIV (corrected)* flow process takes the same raw images and also λ^*_{BOS}. As may be seen the processing is almost identical with the exception of the pre-processing steps. These comprise:

Delete frames - As in the BOS processing the raw images contain both PIV and BOS frames. Thus, the BOS frames are now deleted.

Perspective correction - The optical calibration is applied.

Geometric mask - (Uncorrected only) The mask is used to reduce the size of the field of view to one similar to that defined in the crop process in the BOS processing.

Deform with vector - (Corrected only) This is where the correction of PIV imagery is performed. The operation takes the λ^*_{BOS} vector fields as input and uses these to deform the corresponding PIV image. The result is a PIV image which has had the position error from refractive distortion removed. In addition, the vector field inherits the mask of the BOS process. This ensures that only regions which were suitably corrected contribute to the PIV calculation.

The remaining processing steps are typical PIV processing which yields instantaneous velocity vector fields and time averaging to yield velocity and turbulence vector and scalar fields. A rotate operation can be seen as one of the final steps to correct the rotation applied by the perspective correction.

Whilst DaVis provides plotting capabilities, stitching and aligning the time averaged vector fields from each of the four positions was most easily achieved in python. It is in these python scripts that an estimation of the surface position is made.

4.3 Calibration of the BOS correction method

The experimental campaign consists of calibrations and measurements. Since the refractive index is temperature dependent, each of these measurements would ideally be conducted under the same conditions. Since refraction would distort any calibration measurements it is necessary for these to be performed under adiabatic conditions. Furthermore, the BOS calibration would ideally be conducted with no thermal stratification, i.e. isothermal, such that all sources of distortion in the measurement conditions is accounted for. Thus, the conditions are divided into two groups:

1. Experimental measurement conditions
2. Calibration conditions

The thermal conditions of the experimental and calibration measurements are shown in Table 4.1.

It may be seen that the experimental conditions were able to be reproduced almost exactly with

Table 4.1: Reservoir and ambient conditions for experimental and calibration measurements

Measurement	ΔT_{strat}	$T_{\infty m}$	T_{amb}	Condition
PIV+BOS	$7.88\,^{\circ}$C	$T = 24.98\,^{\circ}$C	$T' = 27.36\,^{\circ}$C	Experimental
BOS@PIV	$7.54\,^{\circ}$C	$T + 0.05\,^{\circ}$C	$T' - 0.82\,^{\circ}$C	Experimental
BOS@PIV reference	$0.19\,^{\circ}$C	$T - 1.56\,^{\circ}$C	$T' - 1.24\,^{\circ}$C	Calibration
BOS@BOS reference	$0.40\,^{\circ}$C	$T - 1.09\,^{\circ}$C	$T' - 3.10\,^{\circ}$C	Calibration
Optical calibration	$0.50\,^{\circ}$C	$T - 2.84\,^{\circ}$C	$T' - 3.07\,^{\circ}$C	Calibration

very little difference between the PIV+BOS and BOS@PIV measurements. However, the calibration condition was not reproduced with the same precision. The differences in the BOS@PIV, BOS@BOS and optical calibration conditions have two causes. The first is due to differences in the ambient temperature; T_{amb}, which in turn affected the average reservoir temperature; $T_{\infty m}$. It may be seen that the calibration conditions were typically conducted at lower temperatures than the experimental measurements, and each calibration occurred at slightly different temperatures. The second difference is due to a pump failure. In order to achieve the isothermal calibration condition, a pump was used to circulate the reservoir fluid. Over time the performance of the pump decreased which is observed as an increase in the ΔT_{strat} for the calibration measurements (which are tabulated in chronological order).

This resulted in two errors, but more importantly the development of a novel correction method which is described herein. An erroneous displacement vector field for BOS@BOS at the top of the heating surface (position 4) is shown in 4.10a. This is prior to the scaling factor being applied but should still faithfully represent the mostly horizontal distortion shown previously in Figure 4.2. For comparison, the same vector field is shown after calibration in 4.10b and the resulting correction vector field λ^*_{BOS} is shown in 4.10c.

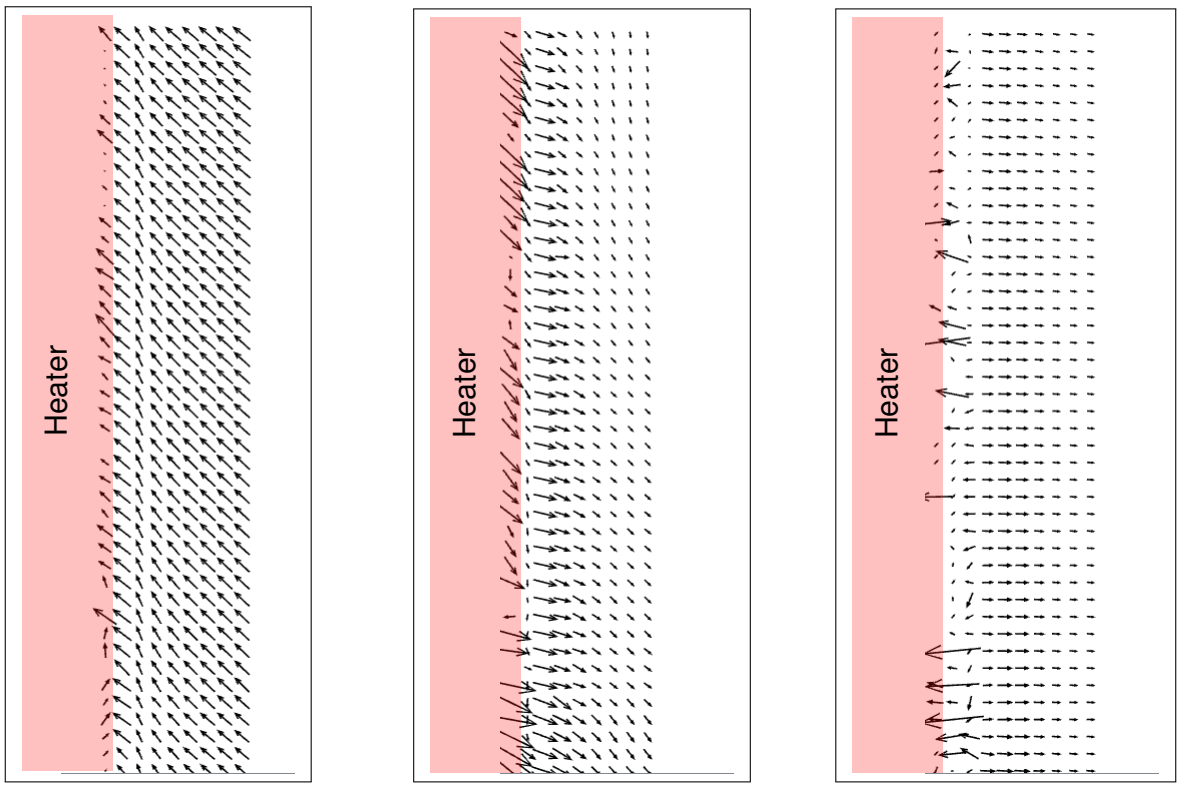

(a) (b) (c)

Figure 4.10: Vector field plots of (a) erroneous $\overline{\lambda}_{BOS}$, (b) calibrated $\overline{\lambda}_{BOS}$, and, (c) $\overline{\lambda^*}$. The heating surface is to the left.

It is immediately apparent that the non-calibrated vector field is substantially different to the expectation of horizontal displacement. Furthermore, the suggested displacement in all regions (even the noisy blurred region near the heating surface) is almost uniformly towards the surface. Since in a refractive index gradient light is distorted towards the higher refractive index; which should be towards the cooler quiescent fluid, the vector field is clearly erroneous and the error is caused by an artefact, rather than a phenomenon. By far the biggest contribution to this error arises from the experimental and reference images being conducted at different temperatures. Second to this is the effect of different thermal stratification.

The BOS camera views the BOS plane through several interfaces between air/acrylic/isothermal water/acrylic/non isothermal water, and likewise for the PIV camera (as shown in Figure 3.1b). The isothermal and non isothermal water refers to that which is in the periphery of the reservoir and not experiencing a thermal gradient from the heater and that which is adjacent to the heating surface, respectively. Due to the mounting arrangements, neither the BOS or PIV camera are perfectly perpendicular to these interfaces and thus from Snell's law it is clear that some amount of refraction can be expected to occur. Since the refractive index of all the constituent materials are temperature dependent, observing the same reference image at different ambient and/or experimental conditions would yield an apparent displacement which is dependent upon the view angle of the camera.

Similarly, if there is a thermal stratification in the ambient/experiment present during collection of

the reference image then this would cause an apparent displacement with respect to the gravity vector as the refractive index varies with height. Due to the number of interfaces, unknown temperatures and viewing angles this would be difficult to approximate entirely analytically. However, since the difference in temperature and thermal stratification is known then a formulation is developed to correct for this error using the extant data.

4.3.1 Calibration of the correction method

In order to calibrate the BOS measurements it is necessary to consider the optical equations (developed in Appendix A) which describe the effect of distortion on the light rays. For the purpose of discussion a simplified viewing arrangement is considered which considers only two regions; the region with a variable refractive index fluid, and the region upto the camera. In reality the latter region comprises the shroud, reservoir fluid, reservoir wall, and surrounding air. Here these are considered one homogeneous layer with an effective refractive index n_a.

The resulting equations for the displacement in the x and y directions are thus

$$\xi = W\frac{n_a}{n_f}\tan\phi_{ax} + \left(\frac{W^2}{2}\right)\frac{1}{n}\frac{\partial n}{\partial x} \tag{4.13}$$

$$\zeta = W\frac{n_a}{n_f}\tan\phi_{ay} + \left(\frac{W^2}{2}\right)\frac{1}{n}\frac{\partial n}{\partial y} \tag{4.14}$$

where n_a and n_f are the refractive indices of the ambient and fluid, respectively. The angles ϕ_{ax} and ϕ_{ay} are the refraction angles in the xz- and yz-planes, respectively. Having a single interface between ambient and fluid is clearly a simplification and the term n_a/n_f can be replaced with a more appropriate term by repeated application of Snell's law through all interfaces. However, the purpose here is to highlight how temperature influences the displacement of a light ray. It may be seen this is achieved via the refractive indices which are a property of a given material and heavily dependent upon the density and thus the temperature of that material.

Thus, if one considers the displacement of a light ray through a given refractive index gradient at two different temperatures then the displacements will differ. This is the principle upon which a BOS measurement is made and the goal is typically to measure the refractive index gradient and relate it to some quantity of interest such as the temperature or density. Thus, the tangent terms represent a displacement related to a difference in measurement conditions, rather than due to the quantity of interest and may be considered an error which can be corrected via calibration.

Hence, eqn (4.13) may be used to identify a suitable region in which to correct the error due. For heat transfer problems the refractive index gradient is zero in the quiescent region and hence the error can be measured directly. For the present data the quiescent region is within the field of view for positions 1 to 3, but in position 4 the thermal boundary layer extends beyond the available data. However, due to the asymptotic nature of the temperature profile the temperature

towards the edge of the thermal boundary layer is negligibly different from that within the quiescent region. Hence, the vectors furthest from the surface are used as a calibration set ξ_{cal} and the displacement there is assumed to occur only through difference in conditions between the BOS and reference measurements.

Next the measured error must be appropriately corrected. To do so consider that at a single location the displacement can be written as

$$\xi_m = \xi_0 + \xi_e \tag{4.15}$$

where ξ_m, ξ_0 and ξ_e are the measured, error free and erroneous displacements, respectively. The BOS measurements are in essence the difference between the displacement of a light ray recorded at a reference condition and one at another condition. Thus the measurement can be divided into

$$\xi_m \equiv \xi_b - \xi_r \tag{4.16}$$

where ξ_b and ξ_r are the displacements during the recording of the BOS experimental image and the reference image, respectively. Note that ξ_0 and ξ_e can be similarly subdivided. The measured displacement can be expected to vary with temperature and location due to the combined effects of different temperatures between experimental recording and reference and different thermal stratifications i.e. $\xi_e(x, T)$.

It is convenient to represent the error with a McLaurin series[73] truncated to the first order since the thermal stratification is assumed to be linear in this case. Hence,

$$\xi_e = \xi(x, T)_{cal} = \xi(x_0, T_0) + x\frac{\partial \xi}{\partial x} + T\frac{\partial \xi}{\partial T} \tag{4.17}$$

If x_0 and T_0 are selected to be the values at the mid height of the heater then it follows that $\xi(x_0, T_0) \equiv \overline{\xi}_{cal}$ where $\overline{\xi}_{cal}$ is the spatial average of the calibration data. Also, given the x-direction is parallel to the gravity vector, the variation in displacement with x i.e. $\partial\xi/\partial x$ is the result of thermal stratification which may be introduced by use of the chain rule to yield:

$$\xi_e = \xi(x, T)_{cal} = \overline{\xi}_{cal} + x\frac{\partial \xi}{\partial T}\frac{\partial T}{\partial x} + T\frac{\partial \xi}{\partial T} \tag{4.18}$$

$$\xi(x, T)_{cal} = \overline{\xi}_{cal} + \frac{\partial \xi}{\partial T}\left[x\frac{\partial T}{\partial x} + T\right] \tag{4.19}$$

Given the calibration displacement ξ_{cal} is the result of a BOS measurement, equation (4.16) may be used to substitute for the measurement and reference displacement, and more importantly their temperature and thermal stratification to yield:

$$\xi(x, T)_{cal} = \overline{\xi}_{cal} + \frac{\partial \xi}{\partial T}\left[x\left(\frac{\partial T}{\partial x}\right)_b - x\left(\frac{\partial T}{\partial x}\right)_r + T_b - T_r\right] \tag{4.20}$$

where the subscript b and r refer to the measurement and reference conditions, respectively. The temperatures and thermal stratification also refer to the values at x_0 and T_0, hence the temperature is equal to the temperature at mid height which is equivalent to the average temperature. Since the thermal stratification is assumed linear it has a constant value.

The only unknown in eqn (4.20) is $(\partial\xi/\partial T)$ which will depend on the ratio of refractive indices as may be seen from eqn (4.13). In principle this could be estimated analytically if the temperature, size and material composition of each interface was known. Alternatively, the value can be determined from the calibration data ξ_{cal} by simply rearranging eqn (4.20).

For clarity, the terms in eqn (4.20) have a physical interpretation. The $\overline{\xi}_{cal}$ term represents the uniform difference between the measurement and reference displacement which is caused by the difference in temperature conditions in each case. The $\partial T/\partial x$ along with $\partial\xi/\partial T$ combine to form the gradient with respect to the x location. Hence, this represents an error in the gradient of the displacement vector i.e. $\partial\xi_m/\partial x$. It should be realised that the true measurement should contain a gradient due to measuring the thermal stratification induced refractive distortion i.e. $\partial\xi_0/\partial x \neq 0$.

The correction is applied to the vector field, hence eqn (4.20) is rewritten in vector form as

$$\vec{\xi}_e = \overline{\xi}_{cal}\vec{I} + \frac{\partial\xi}{\partial T}\left[\vec{x}\left(\frac{\partial T}{\partial x}\right)_b - \vec{x}\left(\frac{\partial T}{\partial x}\right)_r + T_b - T_r\right] \tag{4.21}$$

where $\vec{I}$ is the identity vector and an equivalent formulation may be written for $\vec{\zeta}_e$. The result is a relatively easily produced and applied correction to account for different reference and measurement conditions.

For the difference in conditions experienced in this study the difference in temperature dominated the error such that eqn (4.21) was simplified to

$$\vec{\xi}_e \approx \overline{\xi}_{cal}\vec{I}$$

and this was the correction applied to the BOS measurements.

The method to account for differences in thermal stratification was not developed until after the data was processed. As discussed at the start of the chapter the thermal stratification results in less refractive distortion due to $\frac{\partial n}{\partial y} >> \frac{\partial n}{\partial x}$. Hence, despite the method being capable, the error introduced by differences in thermal stratification was corrected for the results presented in 5. Thus, a prudent piece of further work would be to investigate the impact the correction of the thermal stratification has on the PIV+BOS results and for the calibration to be conducted further into the quiescent region.

Similarly, the error introduced by calibrating the PIV and BOS measurements at different thermal conditions is not corrected. The PIV data is located in real world coordinates by an optical calibration which also corrects for apparent distortions present in reference images of a calibration target (as described in section 4.1). Thus, similar to the BOS measurements, if this perspective

correction is performed at different thermal conditions to the PIV measurements then the PIV images will be displaced accordingly. Thus, to best match the PIV and BOS results one could further correct the BOS results to account for the difference in the thermal conditions fossilised in the PIV results.

The final comment on this error is to note that eqn (4.21) shows that the error is minimised when the thermal conditions of the reference and measurement images are identical. If one wishes to observe the displacement due to thermal stratification then it is necessary to use an isothermal reference image.

4.4 PIV+BOS uncertainty and verification

As the BOS calculation uses a PIV processing algorithm and a dot pattern, the uncertainty of the BOS calculation is readily determined. However, analysing the contribution to uncertainty from the scaling and deformation process remains a topic for further investigation.

Confidence in the deformation process can be achieved by using the measured λ_{BOS} to correct the BOS, rather than PIV, images. A successful application would see the BOS target appear stationary and aligned with the reference image in spite of fluctuations and distortion. For the present study there is some apparent motion in the BOS dot pattern after correction. However, the displacements are typically only one or two pixels, and, located in the vicinity of the blurred region. One could implement a particle tracking velocimetry (PTV) type refinement to address these regions, or similarly use them to estimate the residual error in the BOS measurements. However, the magnitude is very small and localised to the region very close to the surface. Hence, the improvement gained is likely negligible.

The scaling factor does not yield so easily to verification. The ideal approach to verification would be to simultaneously measure the distortion at both the BOS and PIV planes. Thus, one might then compare the scaled distortion field λ^*_{BOS} with the measured λ_{PIV}, which should be in agreement.

4.5 Summary

1. The effects of thermally induced refractive distortion have been illustrated.
2. The working principle of a BOS-correction method has been introduced.
3. A new experimental approach to determine the scaling factor has been introduced.
4. The importance of achieving highly repeatable thermal conditions is demonstrated and a method for accounting for difference in condition is proposed. It is shown that if the experimental conditions and the BOS reference images are taken at isothermal conditions the error will be minimised.
5. This method will prove particularly useful for experiments where an isothermal condition is difficult to achieve such as large experimental facilities which may be unable to completely negate the effect of thermal stratification. A further potential use for this method is to enable high resolution stereoscopic and tomographic measurements which by definition cannot meet the requirement for a perpendicular viewing angle.

Chapter 5

Results and discussion

In this chapter, the BOS measurements and the resulting scaling factor are first reported. Prior to the discussion of the PIV+BOS results the main features of the flow are quantified from the uncorrected PIV measurements. Finally the PIV+BOS results are reported and compared to the uncorrected PIV measurements.

The reader is reminded that measurements are taken at four positions along the x-direction. These locations are illustrated in Figure 5.1 and were previously defined in Table 3.5. Thus, the upper portion of the measurement plane is recorded at position 3 and 4 and lower portion at 1 and 2. Where appropriate the time averaged results of each position have been combined to provide a composite plot of the entire measurement plane.

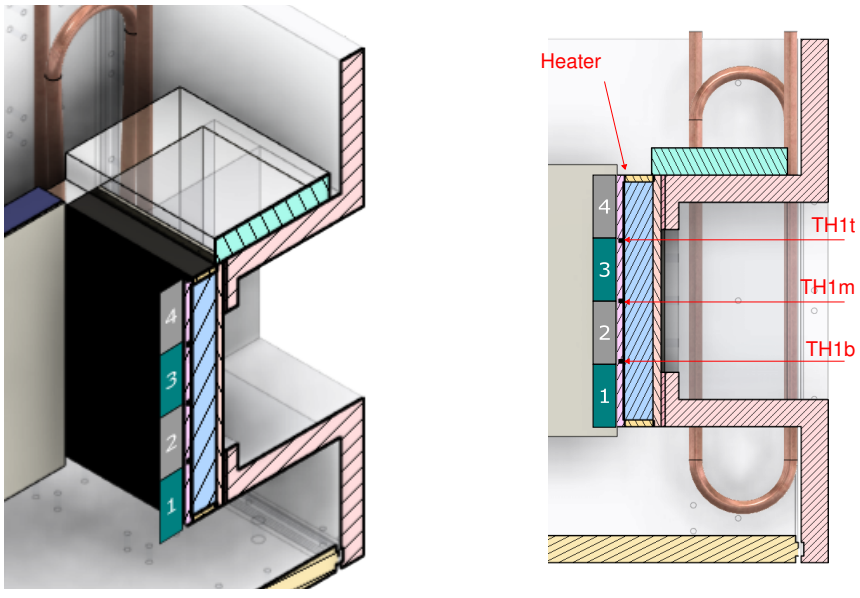

(a) (b)

Figure 5.1: Positions 4 (top) to 1 (bottom) are shown. In (a) perspective view sectioned along the measurement plane and (b) section view.

A consistent challenge throughout this chapter is defining the precise location of the heated surface boundary. This is due to the refraction of measurements in the region immediately adjacent to the surface not being entirely corrected by the BOS-correction method. The true $y = 0$ position of the heating surface is estimated throughout this chapter. To address the uncertainty of heater location the majority of plots include orange and yellow regions, an example of which can be seen in Figure 5.2.

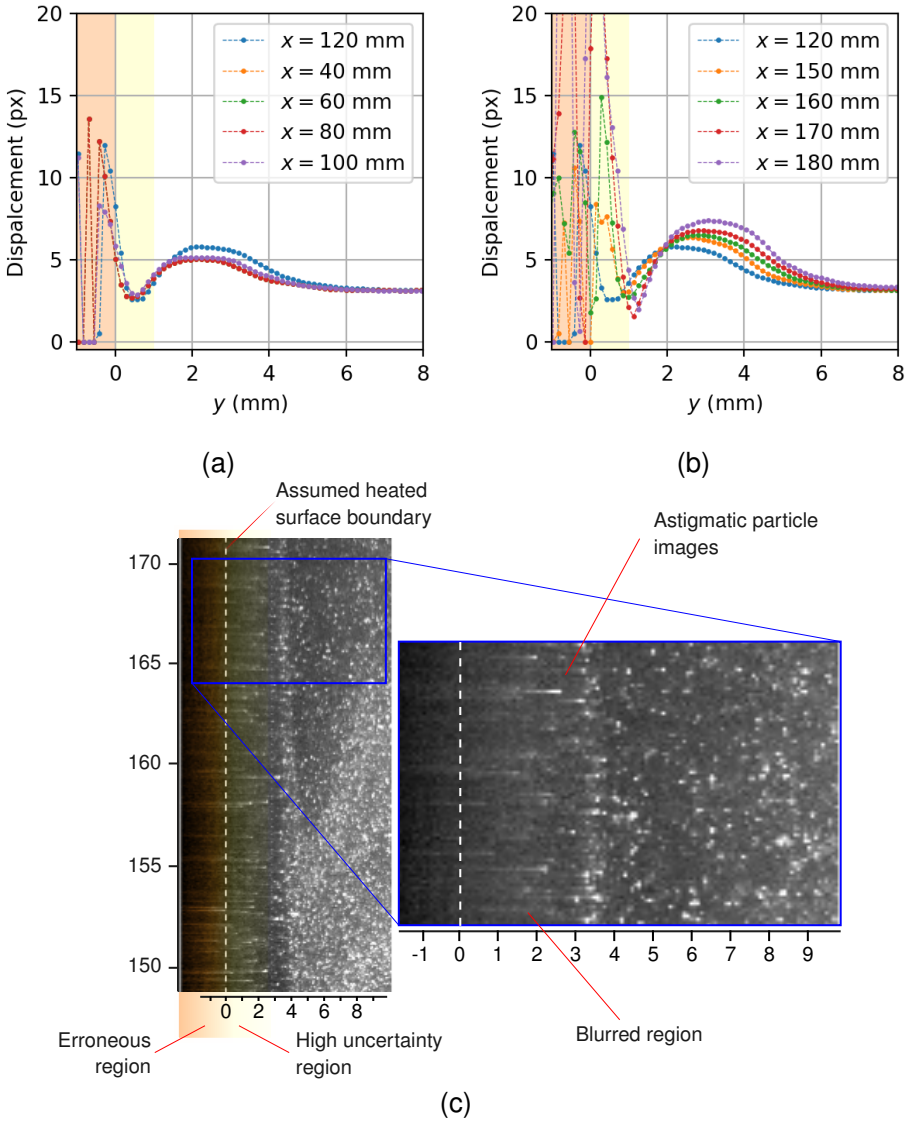

Figure 5.2: Profiles of displacement at the PIV plane $\overline{\lambda}_{PIV}$ for the (a) lower and (b) upper portions of the heater. (c) Annotated raw PIV image with approximate surface location indicated with a dashed line. The regions coloured orange are assumed erroneous and those coloured yellow are expected to have high uncertainty.

As may be seen in Figure 5.2a, and 5.2b, flow measurements are apparent at wall-normal distances of $y < 0$. This is caused by the light rays emitted from the measurement planes toward the camera being refracted toward the heating surface. Such measurements are considered erroneous since the assumed surface location is defined as $y = 0$. Thus, the region of assumed erroneous measurements are coloured in orange as annotated on Figure 5.2c. It may be seen annotated on Figure 5.2c that immediately adjacent to the surface is a blurred region. In this

region the BOS correction method is assumed to be less accurate due to a combination of the highly blurred and astigmatic images and the gap between the BOS target and heating surface. The gap is caused by the curvature of the heating surface (previously shown in Figure 3.8) and is approximately 1 mm wide. The blurring in this region makes it difficult to define a clear boundary between the data which has been corrected and that which has not. Hence, measurements in the region $0 \leq y \leq 1$ are considered uncorrected and the region is coloured yellow. Beyond the blurred region is a small band of seemingly non-displaced region which corresponds with where local magnification occurs due to the water acting as a liquid lens. Beyond this a large displacement is apparent which reduces non uniformly as the temperature gradient tends to zero at the extent of the thermal boundary layer.

Looking again at time averaged displacement at the PIV plane shown in Figure 5.2a, one can see up to approximately $x \cong 100$ mm the distortion is consistent in shape and magnitude. However beyond this the shape and magnitude continually evolve up to the trailing edge ($x = 187$ mm). Since the refractive index gradient is the result of thermal gradients, this means that the temperature profile experiences the same evolution.

The values for transition to turbulence reported in the literature are shown in Figure 5.3. It may be seen that at $x \cong 110$ mm the thermal transition is reported to begin. This appears to be in agreement with the evolution of the displacement profiles shown in Figure 5.2a. However, as will be shown in 5.3, the hydrodynamic and thermal transitions appear to be co-located in this work.

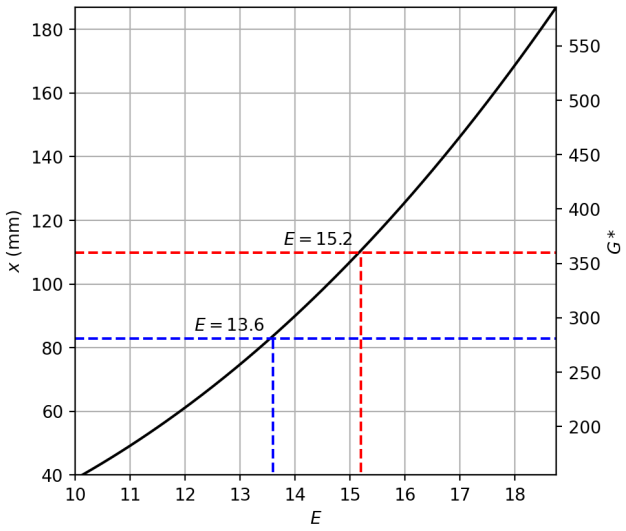

Figure 5.3: A plot (solid black line) of the transition variable E (defined in eqn (2.24)). Annotated are the hydrodynamic (blue dashed) and thermal (red dashed) transition limits from Jaluria and Gebhart[20]. The axis label G^* is defined by eqn (2.25).

5.1 Refractive distortion

The time averaged distortion fields at the BOS ($\overline{\lambda}_{BOS}$) and PIV ($\overline{\lambda}_{PIV}$) planes are shown in Figure 5.4. These show the magnitude of the displacement at each plane as measured using BOS.

It may be seen that there is a gap in the data approximately between $142\,\text{mm} \lesssim x \lesssim 148\,\text{mm}$ which is due to a processing error which does not influence the surrounding data.

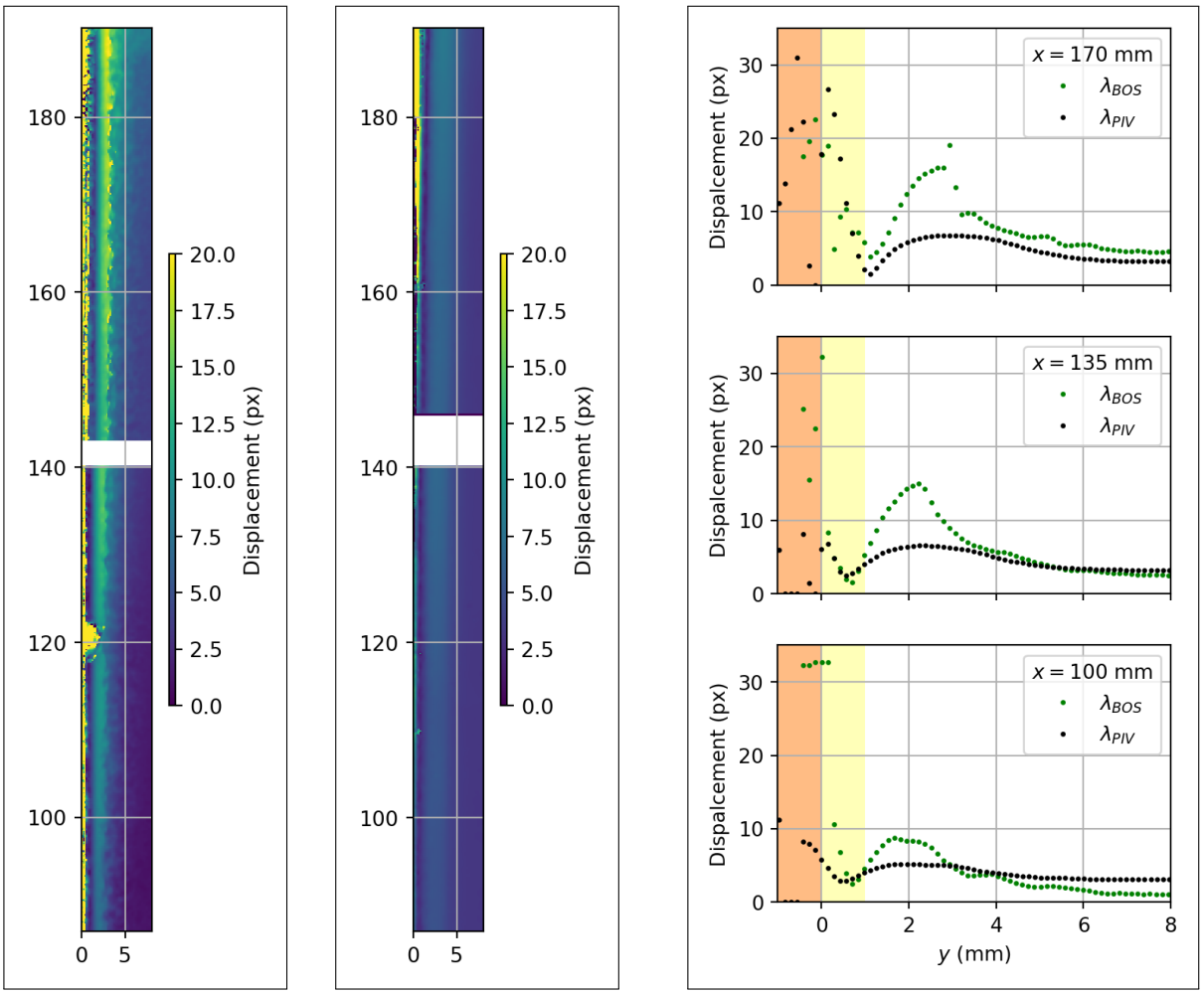

Figure 5.4: Composite stitched images of the time averaged distortion at the (a) BOS and (b) PIV plane for the upper half of the heated surface. (c) Shows a comparison of the displacement in two planes (note that $\lambda_{BOS}\overline{\lambda}_{BOS}$ and $\lambda_{PIV} \equiv \overline{\lambda}_{PIV}$). The heating surface is to the left i.e. $y \leq 0$.

Comparing the two fields Figure 5.4a and 5.4b it may be seen that displacement is qualitatively similar but with a difference in magnitude. This is to be expected due to the difference in optical path length to the BOS and PIV plane. The reader is reminded that the BOS plane is located at the far extent of the variable refractive index field and the PIV plane is located half way across, hence the two regions are expected to incur different amounts of refractive distortion.

The difference between the two fields is seen more clearly in the comparative profiles of displacement shown in Figure 5.4c. The differing profile shapes confirm that a *singular* multiplicative scaling value would be inappropriate as this would simply alter the magnitude of the λ_bos profile.

There are two further noticeable differences between the two fields:

1. In Figure 5.4a there is a region of high displacement (yellow blob) apparent at $x \approx 120\,\text{mm}$ which isn't present in Figure 5.4b. This is caused by the presence of a bubble on the BOS@BOS target during the PIV+BOS measurements. The bubble wasn't present on the reference BOS@BOS image and thus is correctly detected as a region of high displacement. It will be shown in subsection 5.1.1 that the novel approach to producing a scaling factor (reported in chapter 4) can account for the presence of bubbles and other errors well.

2. Comparing the quiescent regions (i.e. $y \gtrsim 5\,\text{mm}$) in Figure 5.4a and Figure 5.4b, one can see an obvious gradient from the bottom to the top of the image in $\overline{\lambda}_{BOS}$ which is not apparent in $\overline{\lambda}_{PIV}$. The cause of the gradient is thermal stratification and the disparity is due to different amounts of thermal stratification being present in the BOS@BOS and BOS@PIV reference images as considered in section 4.3.1. Once again, the novel approach to producing a scaling factor will partially (as discussed in section 4.3.1) account for this.

Finally it should be noted that the $\overline{\lambda}_{BOS}$ field shown in Figure 5.4a appears turbid. Since this is a time averaged result one would expect the field to be smooth and continuous (like that of $\overline{\lambda}_{PIV}$ in Figure 5.4b). This may indicate that either an insufficient number of images or duration was used for the measurement.

5.1.1 Scaling factor

As discussed in section 4.2, the scaling factor (κ) as defined in this work is different to that used by other authors, notably Elsinga et al.[52]. For the purposes of comparison, conversion between the definition of scaling defined in this work (κ) and that in Elsinga et al.[52] (A) is achieved with

$$A = \frac{\kappa}{\overline{\lambda}_{BOS}} - 1 \tag{5.1}$$

A plot of the scaling factor used in this work and the equivalent definition by Elsinga et al.[52] is shown in Figure 5.5. The equivalent scaling factor seen in Figure 5.5b is surprisingly different from the constant value reported by Elsinga et al.[52]. The plot shows that for the data collected here the scaling factor is certainly not constant and has a much wider range of magnitude. This means the scaling factor κ used in this work is not just scaling the data but accounts for other differences that are not accounted for in the analytical derivation.

Some of the differences have intuitive origins and can be explained (i.e. bubbles and thermal stratification) whereas the origin of others is less clear.

There also appears to be a wall-normal gradient apparent at each position. This could have several explanations. The direct temperature dependence of the refractive index for water may play a more significant role than anticipated. In the study by Elsinga et al.[52] the fluid was air and the

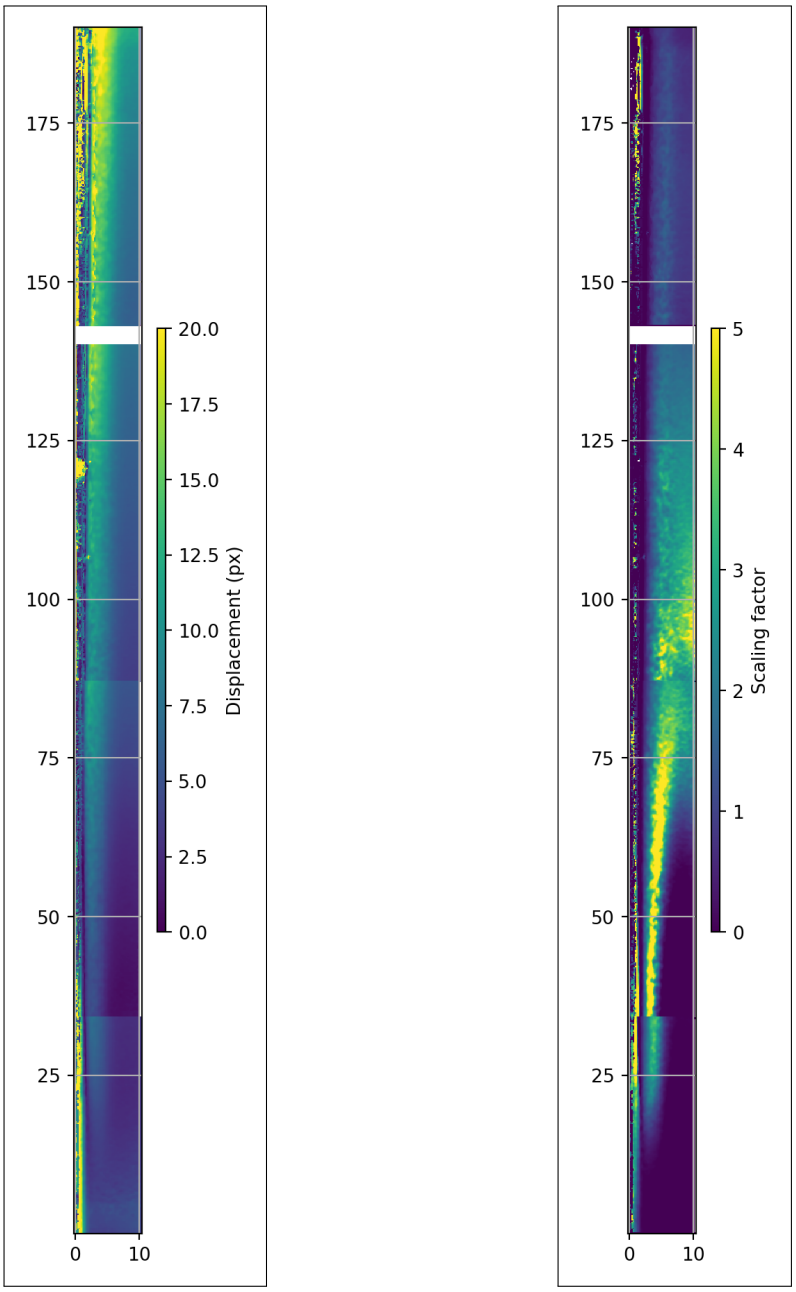

Figure 5.5: Composite stitched image of the scaling factor (a) defined in this work as κ eqn (4.11), and, (b) defined by Elsinga et al.[52] as A eqn (5.1).

change in refractive index was purely due to density gradients. Whereas in the present results there is both a temperature and density gradient. Since the scaling factor here is experimentally determined, no simplifying assumption has been implied on its dependence. If it could be shown that the temperature dependence of the refractive index for water made a substantial contribution to the displacement then this would indicate that the summative, experimentally determined scaling factor as defined in this work is more appropriate for water based experiments than the formulation by Elsinga et al.[52]. The validity of this statement could be determined as an activity for further work. An alternative explanation is that the slight angle at which the planes are observed may cause different amounts of localised magnification and blurring when observing the BOS and PIV planes. The scaling factor derived by Elsinga et al.[52] is formed on the assumption that the optical axis is perpendicular to the measurement plane and that light rays are paraxial.

Whilst the difference discussed so far may have intuitive origins, they are also minor by comparison to the large differences seen at position 2 and 3 where the scaling factor defined in eqn (5.1) approaches a value of $A \rightarrow 5$. The regions of high scaling factor correlate with regions of very little displacement in the $\overline{\lambda}_{BOS}$ field. The $\overline{\lambda}_{PIV}$ field appears much more uniform by comparison and not to show any regions of near zero displacement. Hence the scaling factor which relates the two will naturally be larger when multiplying a near zero value in the BOS field to match the value in the PIV field. Thus, the resulting scaling factor would appear to be calculated correctly which suggests the differences are due to the effect of residual error in the BOS measurements, some other unidentified difference between the measurements, or most likely a combination of the two.

One cause might be the slight misalignment of the PIV and BOS cameras from which $\overline{\lambda}_{PIV}$ and $\overline{\lambda}_{BOS}$ are measured, respectively. The camera images are very slightly offset and rotated from one another. This misalignment is addressed by an optical calibration which corrects perspective distortion i.e. offset, rotation and magnification. The perspective correction was conducted at slightly different thermal conditions to the BOS measurement and reference recordings (see Table 4.1), hence this difference in condition may result in an apparent displacement. Since the rotation was one of the components of this correction it may be the cause of the slightly diagonal high valued scaling factor seen prominently around a quarter of the way up the surface in Figure 5.5. However, given this is a systematic error one would expect similar features to be apparent at all positions and thus the presence of four similar diagonal trends, which are not apparent in the results.

Another cause might be expansion or distortion of the acrylic reservoir at different thermal conditions. The acrylic structure of the apparatus, through which the BOS and PIV measurements are made, is constrained at the bottom by a perpendicular acrylic section forming the bottom of the reservoir. Towards the top i.e. at the waterline, the hydrostatic load on the structure reduces to zero. Thus, deflection of the surface would have the greatest magnitude at the mid height. Similarly, the mid height, due to it's lesser mechanical constraint, is more able to thermally expand. This expansion could potentially explain why the scaling factor appears to have larger values

around the mid height and lesser towards the top and bottom.

Despite the unclear origin of some of the differences, the results demonstrate that an analytical scaling factor (A) is suited to an experiment with very little error, but the experimentally determined scaling factor (κ) may be better suited to heat transfer type experiments due to the additional complexity of variable thermal conditions.

5.2 Uncorrected PIV results

The natural convection flow exhibits a number of features which are observable in the results. Some of these features are previously reported phenomena and some are artefacts of distortion and the BOS-correction method. In this section these features will be discussed and the respective origin hypothesised. The flow features thought to be related to distortion are:

- Alignment of time averaged data
- Non-zero velocity at the heater surface boundary

The flow features thought to be unrelated to distortion are:

- Turbulence near the leading edge
- Flow reversal
- Transition to turbulence

5.2.1 Flow features related to distortion

Alignment of time averaged data - As discussed at the start of the chapter, the location of the heating surface is not known precisely due to blurring. To produce composite time averaged fields (e.g. Figure 5.5) a common reference point must be identifiable in the overlapped field of view of each adjacent position. The x location is readily determined using a ruler as described in section 3.1. However, the y location is more challenging due to the curvature of the heating surface and the inability to identify its location in measurement images due to blurring.

Here a flow feature is used as an alternative reference. The velocity profile achieves a maxima a short distance from the surface (as shown in Figure 2.5). In the overlapped fields of view this velocity maxima should appear at identical locations in the time averaged data of two adjacent positions and thus may be used to correct for misalignment. Position 1 has the least blur due to the relatively small thermal boundary layer and thus the position of the surface is known with the greatest accuracy, hence the surface location at position 1 is assumed correct and the other composite images are adjusted respectively. Given the lack of overlap (due to a processing error) position 4 is not adjusted.

The process of aligning the peaks is shown in Figure 5.6 and Figure 5.7. Two sets of four images

are shown corresponding to the correction of the position 3 and 2 data. For each, the *raw* or misaligned velocity and first derivative of velocity profiles are shown. The derivative is used to identify the peak velocity and the upper dataset is shifted to match the lower. This is depicted on the two right hand plots. It may be seen that this aligns the profiles well but there is still slight disagreement in the magnitude. The reason for the difference in magnitude is most likely due to the effect of thermal stratification induced refractive distortion. The difference is clearly quite small and in a typical PIV study would be blended or simply accepted without correction as the difference is almost negligible.

To appreciate the following discussion the reader is reminded that, from the literature introduced in chapter 2, the thermal boundary layer for water will extend to roughly in line with the peak velocity. Hence, refractive distortion induced by the thermal boundary layer can be expected to dominate in this region. Outside of this, refractive distortion, if present, is due to thermal stratification.

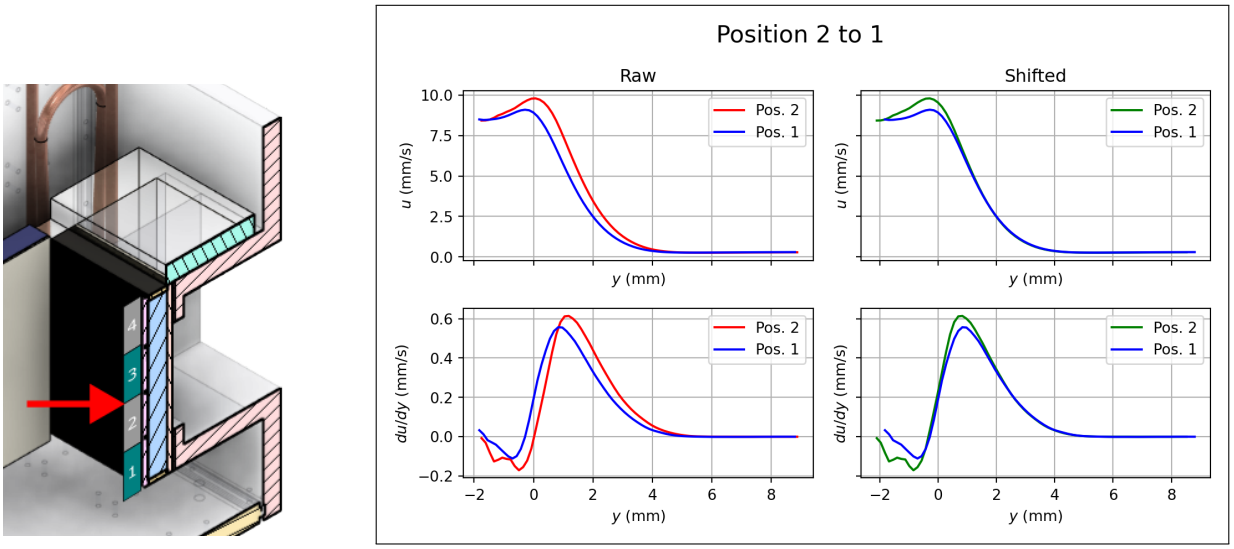

(a)

Figure 5.6: Comparison of the raw and aligned velocity and first derivative aligning positions 3 to 2. The heater is to the left.

Non-zero velocity at the heater surface boundary - Looking once again at the shifted velocity profiles in Figure 5.6 and Figure 5.7, it may be seen that the velocity does not tend to zero at the apparent surface location (indicated by $y = 0$) or even for $y < 0$. This has two causes;

1. As discussed at the start of the chapter, the surface location is almost certainly incorrect due to the effects of refraction which tends to distort the seeding particles towards the surface and beyond the apparent surface position i.e. to $y < 0$.
2. The second reason is the combined effect of reflection and blurring. The reflected particle images will appear to move at a similar velocity to the particles they are reflecting with blurring tending to magnify and smear the region between valid particle images and reflections. Finally, in the $y < 0$ region the profiles seem unrelated and unphysical. This is

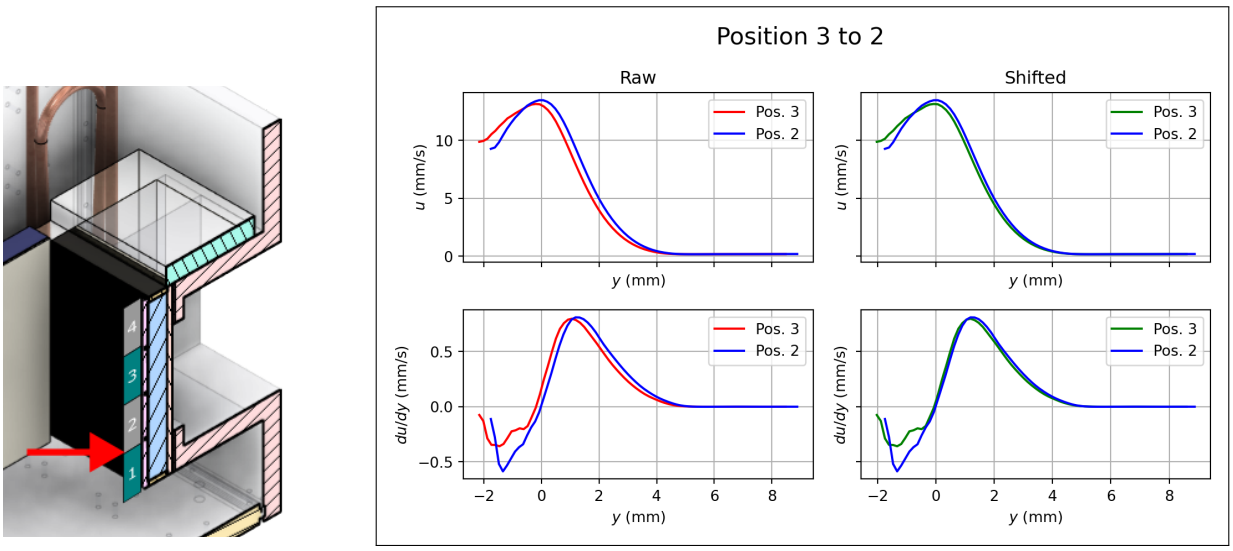

(a)

Figure 5.7: Comparison of the raw and aligned velocity and first derivative aligning positions 2 to 1. The heater is to the left.

because these vectors are determined purely from reflection and blurring and are simply noise.

From these profiles the expectation of the correction process can be set. The region of the velocity profile which extends from the quiescent to (and even beyond) the surface appears qualitatively correct but with some amount of distortion, increasingly so nearer to the surface. Correction of this distortion is the aim of the correction.

The lack of a zero velocity near to the surface suggests that the noise introduced by blurring is substantial (as shown in Figure 5.2c). Thus, there exists a region immediately adjacent to the surface which is so substantially blurred that a successful correction will not be achievable with the method employed here. The goal is therefore to *recover* as much of the profile as possible and minimise the amount of data lost to blurring.

5.2.2 Flow features unrelated to distortion

The uncorrected time averaged velocity fields, and corresponding profiles, are shown in Figure 5.8. These images will be used to discuss some of the main features of the flow.

The flow in the x-direction (i.e. the u component of velocity) is shown in Figure 5.8a and similarly for the y-direction (v component) in Figure 5.8c. Comparing the scales, it may be seen that the u component of velocity is dominant and the wall-normal flow (v component) is approximately zero everywhere except near the leading and trailing edges.

There are three prominent flow features which are recognisable as phenomena previously discussed in chapter 2.

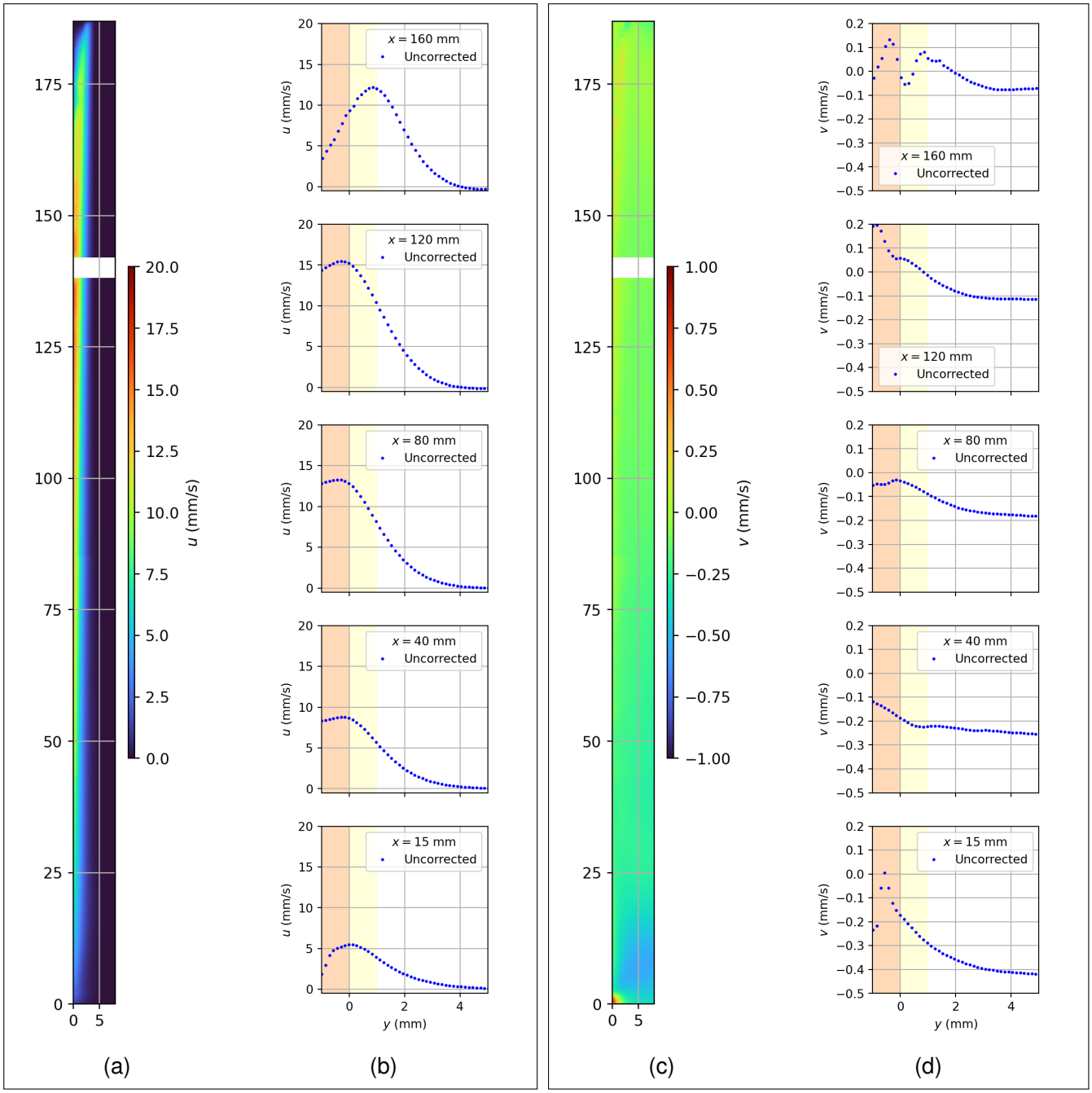

Figure 5.8: Composite stitched image of the uncorrected time averaged u-component of velocity (a) field and (b) profiles at several x locations. Similarly, the uncorrected time averaged v-component of velocity (c) field and (d) profiles at several x locations. The heater is to the left.

Turbulence near the leading edge - The sharp corner of the leading edge of the heater is known to result in a disturbance to the development of the velocity boundary layer. This can be seen in Figure 5.8c as the blue region towards the bottom. This is shown more clearly in Figure 5.8d where the negative value refers to a flow moving towards the surface.

Flow reversal - Figure 5.9 shows a plot of the u component of velocity. The scale is set such that reversed flow is visible and the (positive) upwards flow is set to zero. This is accompanied with plots of the streamlines. The reversed flow can be seen to occur away from the surface and is most prominent near the trailing edge of the heater. Comparing the velocity scale, it can be seen that this flow is two orders of magnitude lesser than the upward flow shown in Figure 5.8a.

The flow reversal is assumed to be caused by a temperature deficit as defined by Tanny and Cohen[26] i.e. where the fluid in the outer portion of the boundary layer is cooler than the quiescent fluid at a given x position. The outer boundary layer fluid is cooler since it is advected. However, due to thermal stratification the quiescent temperature upstream is warmer and thus the cooler boundary layer fluid becomes negatively buoyant. The temperature deficit is the difference in temperature between the outer regions of the boundary layer and the quiescent fluid. The effect of the temperature deficit can be seen to extend almost the entire length of the surface. However, in the lower half the velocity of the reversed flow is nearly zero with a more substantial reversed flow becoming clearly apparent between $100\,\text{mm} \leq x \leq 125\,\text{mm}$.

Transition to turbulence - Figure 5.10 and Figure 5.11 show the uncorrected and corrected time averaged velocity profiles, respectively. The velocity is scaled by the local maxima and the distance from the wall is generalised by the use of a similarity variable η given by:

$$\eta = \frac{y}{5x/G^*} \qquad \text{(defined in eqn (2.27))}$$

The profiles are labelled with the local kinetic energy flux E (as defined in eqn (2.24)) which is used to quantify the transition to turbulence. As shown on Figure 5.3, Jaluria and Gebhart[20] found that the onset of transition occurred at $E = 13.6$ and thermal transition began at $E = 15.2$.

In Figure 5.10a the laminar profiles are shown. It may be seen that the profiles display very similar behaviour. There are two significant observations:

1. There is no apparent change in character of the profiles despite exceeding the values for the onset of transition defined by Jaluria and Gebhart[20]. This is consistent with their later findings[25], where they state that thermal stratification tends to delay the onset of transition.
2. There is a slight variation for the profile at $x = 40\,\text{mm}$ i.e. nearest the leading edge. This difference is assumed to be a leading edge effect, caused by the sharp edges of the heater which disrupt the flow as it is drawn to the surface. It may be seen that the profile gradually trends towards the profile at $x = 120\,\text{mm}$.

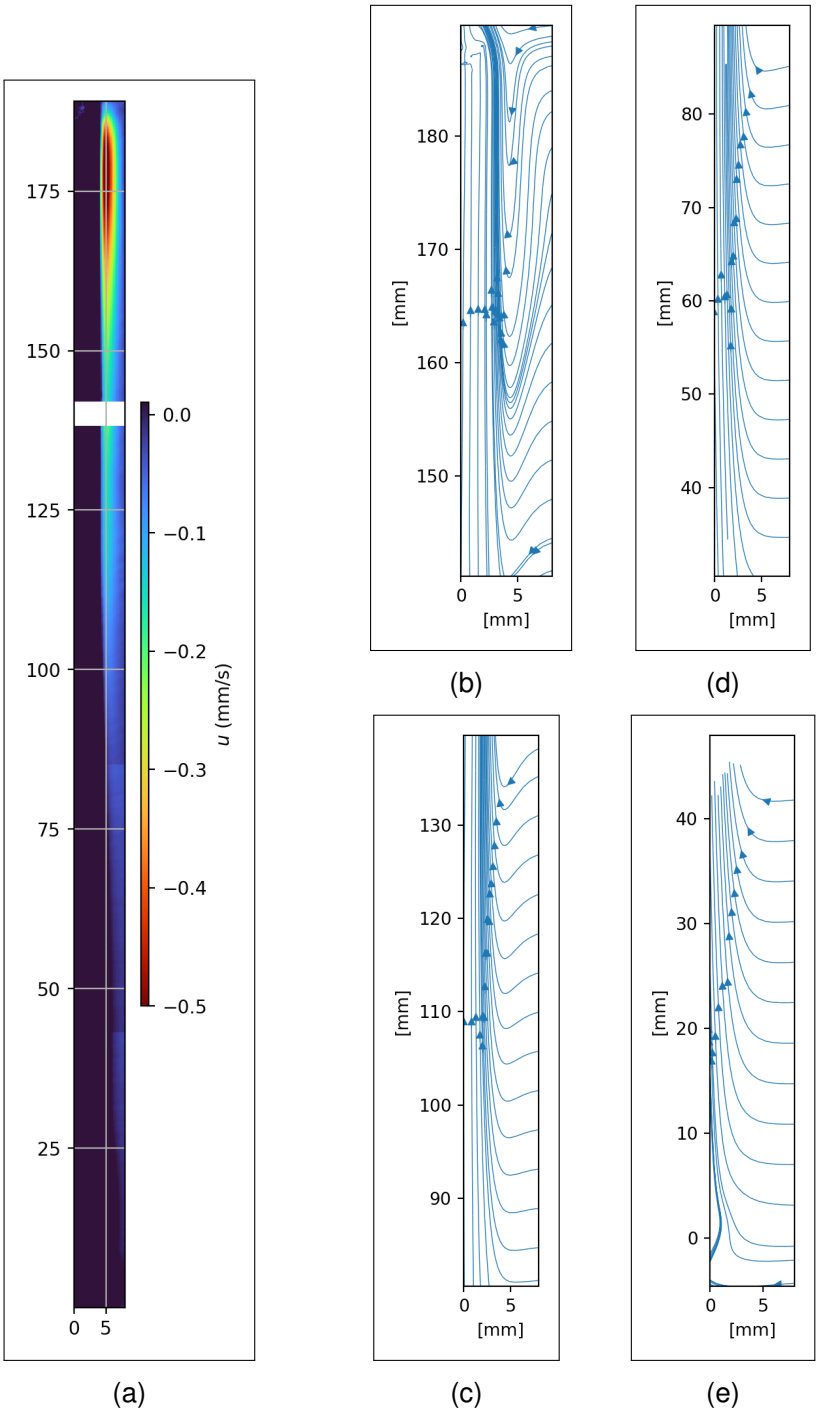

Figure 5.9: (a) Composite stitched images of the uncorrected time averaged u component of velocity. The colour scale is adjusted such that the reversed flow is apparent. Streamlines are plotted for (b) pos. 4, (c) pos. 3, (d) pos. 2, and, (e) pos. 1. The heater is to the left.

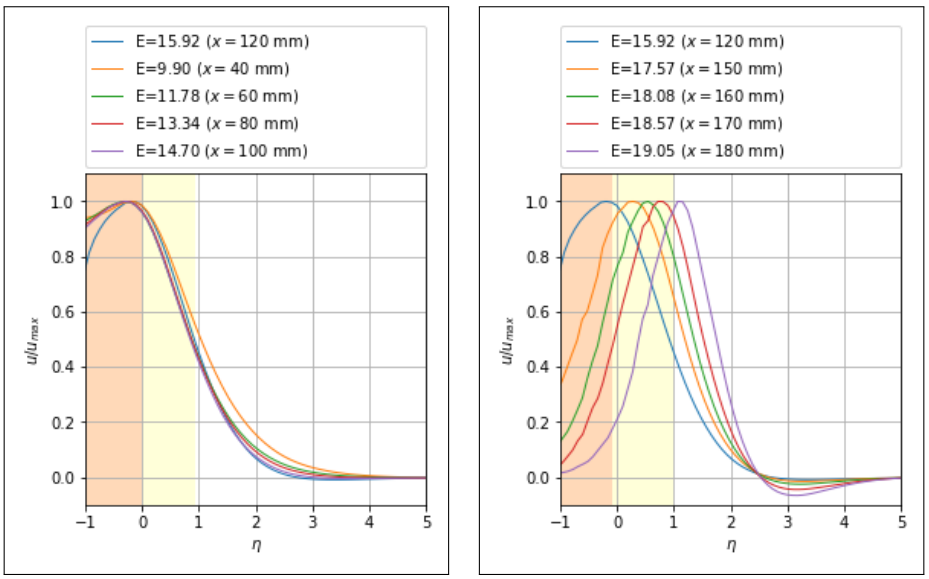

(a) (b)

Figure 5.10: Uncorrected time averaged velocity profiles in the (a) laminar, and (b) transitioning flow. The heater is to the left.

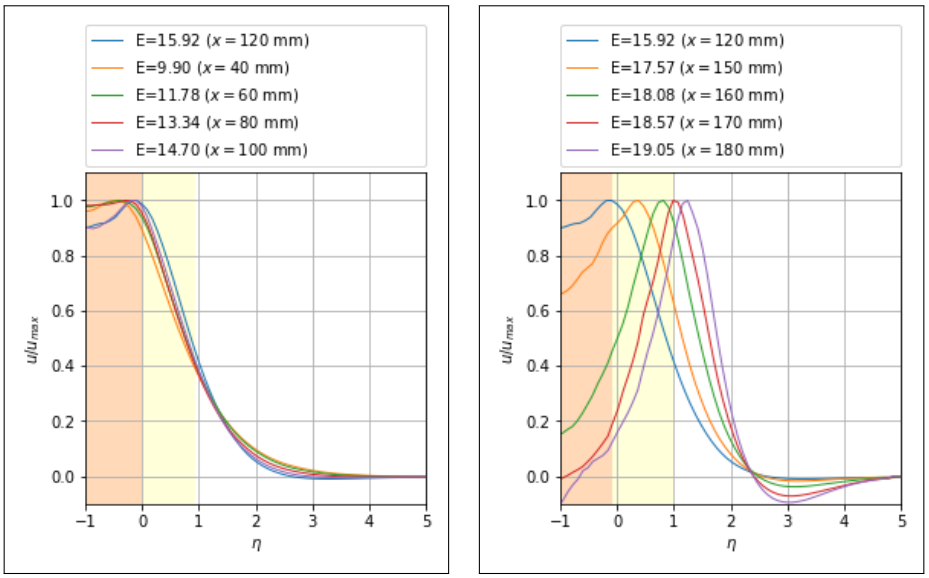

(a) (b)

Figure 5.11: Corrected time averaged velocity profiles in the (a) laminar, and (b) transitioning flow. The heater is to the left.

The velocity profiles for the upper portion of the surface are shown in Figure 5.10b. Again, several observations can be made:

1. It is clearly apparent that the velocity profile evolves in character with increasing distance along the surface.
2. From $x \cong 120$ mm or $E \cong 15.92$, the non-dimensional profile changes substantially. It may be seen that for increasing location x the velocity maxima occurs further from the surface i.e. thickening of the hydrodynamic boundary layer. This indicates a departure from the laminar flow observed in the lower portion of the flow.
3. In Jaluria and Gebhart[20], where there was no thermal stratification, as the flow transitioned to turbulence the velocity profile evolved in character but the maximal velocity remained at $\eta \approx 0.8$ (shown in Figure 2.5).
4. In Jaluria and Gebhart[25], where thermal stratification was present, as the level of stratification was increased the peak velocity tended toward the surface.
5. Hence the apparent trend of the maximal velocity away from the heated surface is not consistent with the findings of either Jaluria and Gebhart[25] or Jaluria and Gebhart[20]. Thus, this feature can't be fully explained by a transition to turbulence or thermal stratification.
6. The velocity profiles do not achieve a new similarity i.e. they continue to evolve up to the trailing edge of the heater.

For the purposes of discussion, the equivalent corrected velocity profiles are shown in Figure 5.11. It may be seen that even after correction for distortion the same trends are apparent. This was an unexpected finding and suggests the cause of this evolution is not the result of refraction but some other mechanism.

There are several possible causes, three of which seem most likely:

1. The heating surface used in this work is known to be concave with a maximum deflection estimated to be $\delta y \approx 1.5$ mm. Thus, over the surface one might expect the velocity profile to shift due to the error in the assumed $y = 0$ position. However, one would expect to see this in both the laminar and turbulent profiles in somewhat equal measure, which isn't the case.
2. Alternatively, the shift in the peak may be the result of the flow reversal which was not observed in either of the publications by Jaluria and Gebhart[20,25].
3. Finally, due to the relatively short length of the heating surface it is conceivable this variation is due to a trailing edge effect that would not have been apparent in the taller heaters used by Jaluria and Gebhart[20,25].

The exact cause cannot be identified with the combined effects of thermal stratification and a curved surface which are currently present in the apparatus. However, introducing a flat heater or reducing the amount of thermal stratification would allow greater clarity on the origin of this flow feature.

5.3 BOS-corrected PIV results

5.3.1 Comparison of corrected and uncorrected results

A comparison of the corrected and uncorrected u component of velocity is shown in Figure 5.12. Comparing Figure 5.12a and Figure 5.12b, the effect of correction is most apparent as a change in velocity magnitude as the flow transitions to turbulence. This observation is further illustrated in Figure 5.12c where it may be seen that in the lower half of the heater, where the flow is laminar, the corrected and uncorrected velocities are negligibly different. However, as the boundary layer transitions to turbulence a more appreciable difference in velocity is observed. In the velocity profile at $x = 160$ mm a significant difference in velocity is clearly apparent and the location of the peak velocity is also shifted. Surprisingly, even at $x = 120$ mm where the recirculation in the quiescent region has just begun to form, the difference in magnitude is apparent.

Intuitively this makes sense, since at the leading edge the thermal boundary layer will be constrained to very near the surface and thus will minimally distort the PIV images. Whereas, at the trailing edge the thermal boundary layer will be larger and hence a greater portion of the image is distorted by refraction.

Whilst the velocity profiles differ in the near wall region the boundary layer appears to have the same thickness for both the corrected and uncorrected results, suggesting the effect of refractive distortion is confined to within the boundary layer. Whilst this seems reasonable, more generally i.e. for scenarios where the quiescent region is not stationary such as a channel flow, this is not possible to confirm from this work. Furthermore, the effects of stratification induced refractive distortion on a flow with a mobile quiescent region may be more significant than demonstrated here. Therefore, application of the BOS correction method to a channel geometry could provide further insight.

Figure 5.13 shows the corrected time averaged turbulent and average kinetic energy in the upper portion of the heater with accompanying profiles at several x locations. For both turbulent (Figure 5.13b) and average (Figure 5.13d) kinetic energy the corrected and uncorrected profiles are in reasonable agreement until around $x = 125$ mm where transition to turbulence is assumed to begin. From this point onwards the average kinetic energy can be seen to decrease and the turbulent kinetic energy increase. Also apparent during this transition is an increase in the difference between the corrected and uncorrected results.

This increasing disparity is thought to be due to the fluctuation of temperature within the thermal boundary layer occurring at a different frequency to the turbulent fluid motion. This was previously reported by Jaluria and Gebhart[25] and shown in Figure 2.6. The differences in frequency are hypothesised to give the appearance of increased turbulence due to apparent motion from refraction rather than actual fluid motion. The reduction in magnitude of turbulent and average kinetic energy would seem to support this hypothesis.

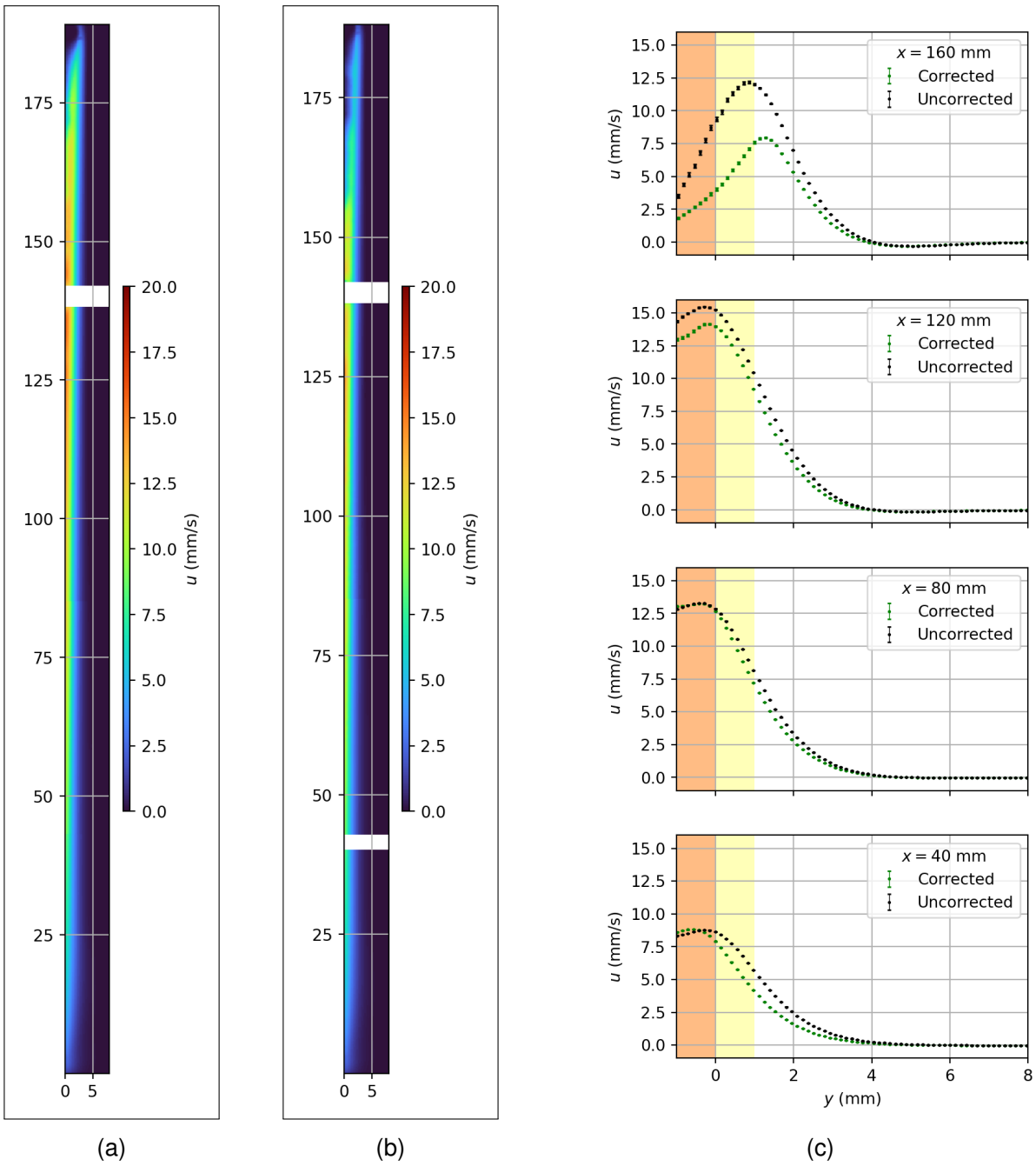

Figure 5.12: Composite stitched images of the (a) uncorrected, and, (b) corrected u component of velocity. (c) shows the u component of velocity profile at several x locations for corrected and uncorrected results. The heater is to the left.

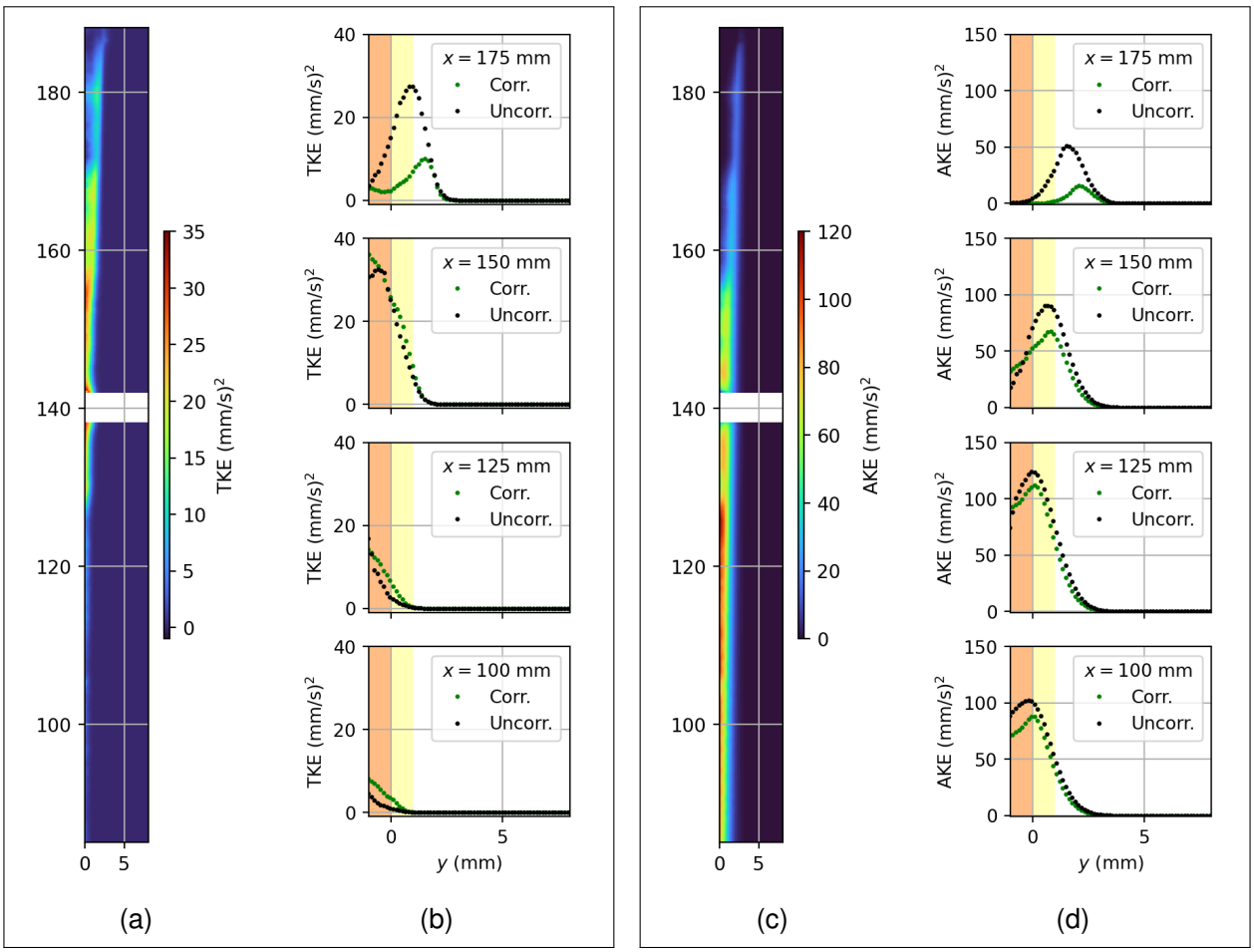

Figure 5.13: Plots of the corrected turbulent kinetic energy (a) composite stitched image, and, (b) comparison profiles at several x locations. Similarly, plots of the corrected average kinetic energy (c) composite stitched image, and, (d) comparison profiles at several x locations. The heater is to the left.

5.3.2 Transition to turbulence

Figure 5.14 shows profiles of the displacement from the time averaged scaled and corrected BOS measurement; $\overline{\lambda^*}$. The similarity parameter η (defined in eqn (2.27)) is used to show how the profiles evolve along the surface. Since the displacement is related only to temperature, any transitions in the displacement profiles is assumed to imply a transition in temperature also.

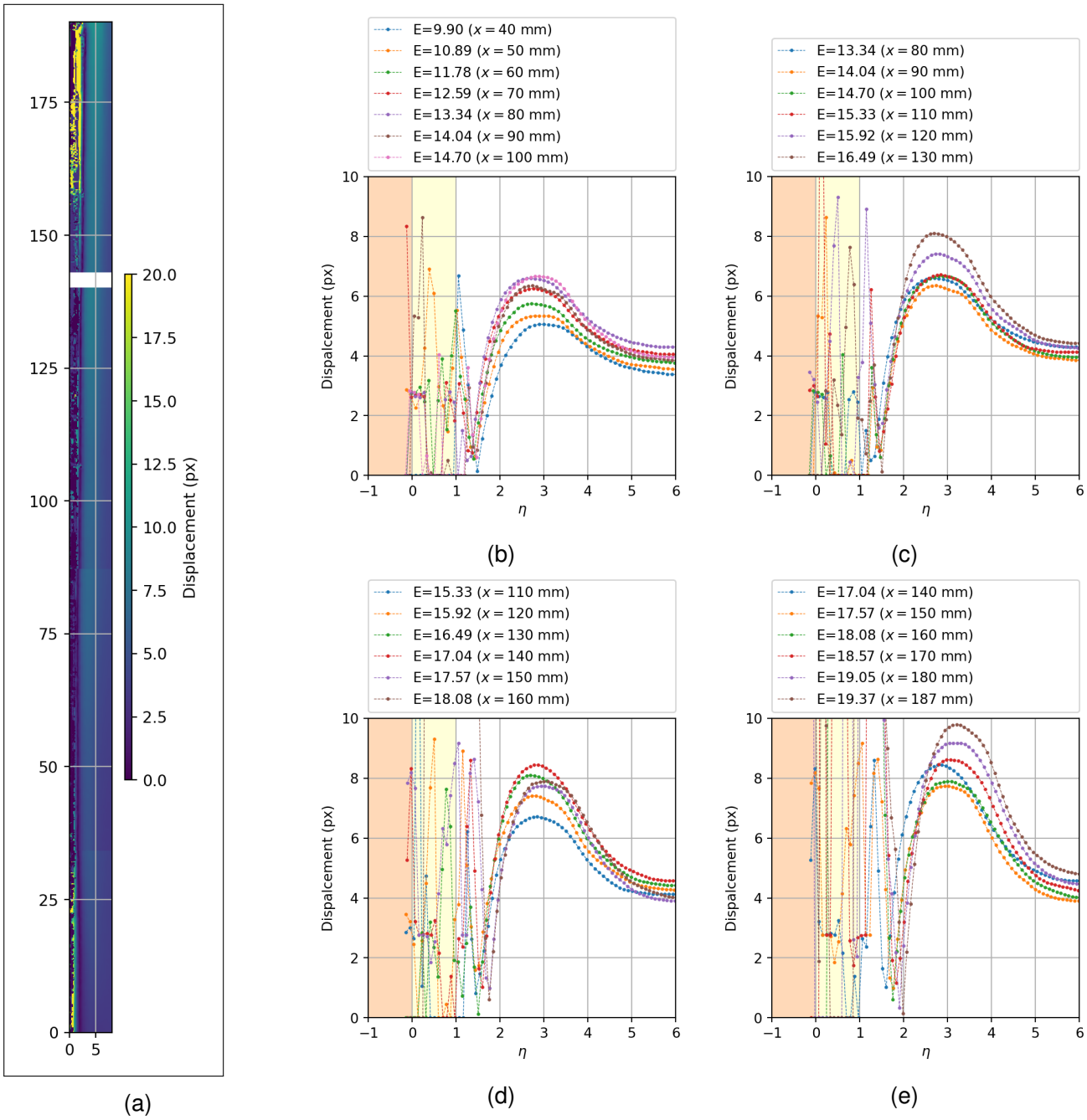

Figure 5.14: Displacement from the time averaged scaled and corrected BOS measurement; $\overline{\lambda^*}$. Regions shown are (a) the full field, (b) re-laminarisation of leading edge, (c) first transition, (d) second transition, and (e) trailing edge. The similarity parameter η is defined in eqn (2.27) and the heated surface to the left.

Each sub figure shows a portion of the heated surface:

- Figure 5.14b shows the region $40\,\text{mm} \leq x \leq 100\,\text{mm}$. This corresponds with the region near the leading edge. It may be seen that the maxima and quiescent values increase with x. The maxima at $x = 40\,\text{mm}$ appears at a greater η value. The η position of the maxima gradually reduces as x increases. The evolution in maxima η position is interpreted as the re-laminarisation of flow following the production of turbulence by leading edge effect.
- Figure 5.14c shows the region $80\,\text{mm} \leq x \leq 130\,\text{mm}$. This covers the region where transition to turbulence was suggested to occur. It may be seen that the $x = 80, 90, 100, 110\,\text{mm}$ profiles appear to overlap reasonably closely. However, the maxima of the $x = 120\,\text{mm}$ profile appears much larger; thereby indicating a change in behaviour which originates in the region $110\,\text{mm} \leq x \leq 120\,\text{mm}$. This approximately coincides with the transition earlier identified in Figure 5.11. Hence this transition is observable for both hydrodynamic and thermal boundary layer.
- Figure 5.14d shows the region $110\,\text{mm} \leq x \leq 160\,\text{mm}$. This covers the region downstream from the onset of transition to turbulence up to the location where flow reversal was observed. It may be seen that the $x = 110, 120, 130, 140\,\text{mm}$ profiles exhibit a continuous evolution of the profile with the maxima occurring at approximately the same η location. Given the spacing of the maxima between the maxima of these profiles the evolution appears to occur more rapidly than seen in either Figure 5.14b or 5.14c. However, the maxima of the $x = 150, 160\,\text{mm}$ profiles are lower in value and occur at a larger η position. This is interpreted as a sudden thickening of the thermal boundary layer which roughly coincides with the peak in reversed flow previously shown in Figure 5.9. Given that this transition occurs near to the trailing edge it is difficult to identify what is responsible for this behaviour. Nonetheless a transition of some kind is observed.
- Figure 5.14e shows the region $80\,\text{mm} \leq x \leq 130\,\text{mm}$. This covers the remainder of the heating surface downstream of the reversed flow. It may be seen that following the transition around $x \cong 150\,\text{mm}$ the profiles appear to evolve all the way to the trailing edge at a similar rate to that seen in Figure 5.14d. In addition, the peak about the maxima appears to get broader i.e. increases in η with x. Thus, this is interpreted as the thermal boundary layer continuing to transition.

Thus there appears to be two distinct transitions observable in the displacement, and thus thermal profiles. As shown in Figure 5.3, for a simpler flow i.e. without thermal stratification, a curved surface, and leading effect, one would expect the hydrodynamic onset of transition and the thermal transition to occur at distinct locations. However, for the complex flow observed here the transition in the region $110\,\text{mm} \leq x \leq 120\,\text{mm}$ is apparent in both the velocity and displacement results.

To better understand the hydrodynamic transition a plot of the corrected and uncorrected vorticity field is shown in Figure 5.15a, along with profiles in Figure 5.15b through to 5.15e.

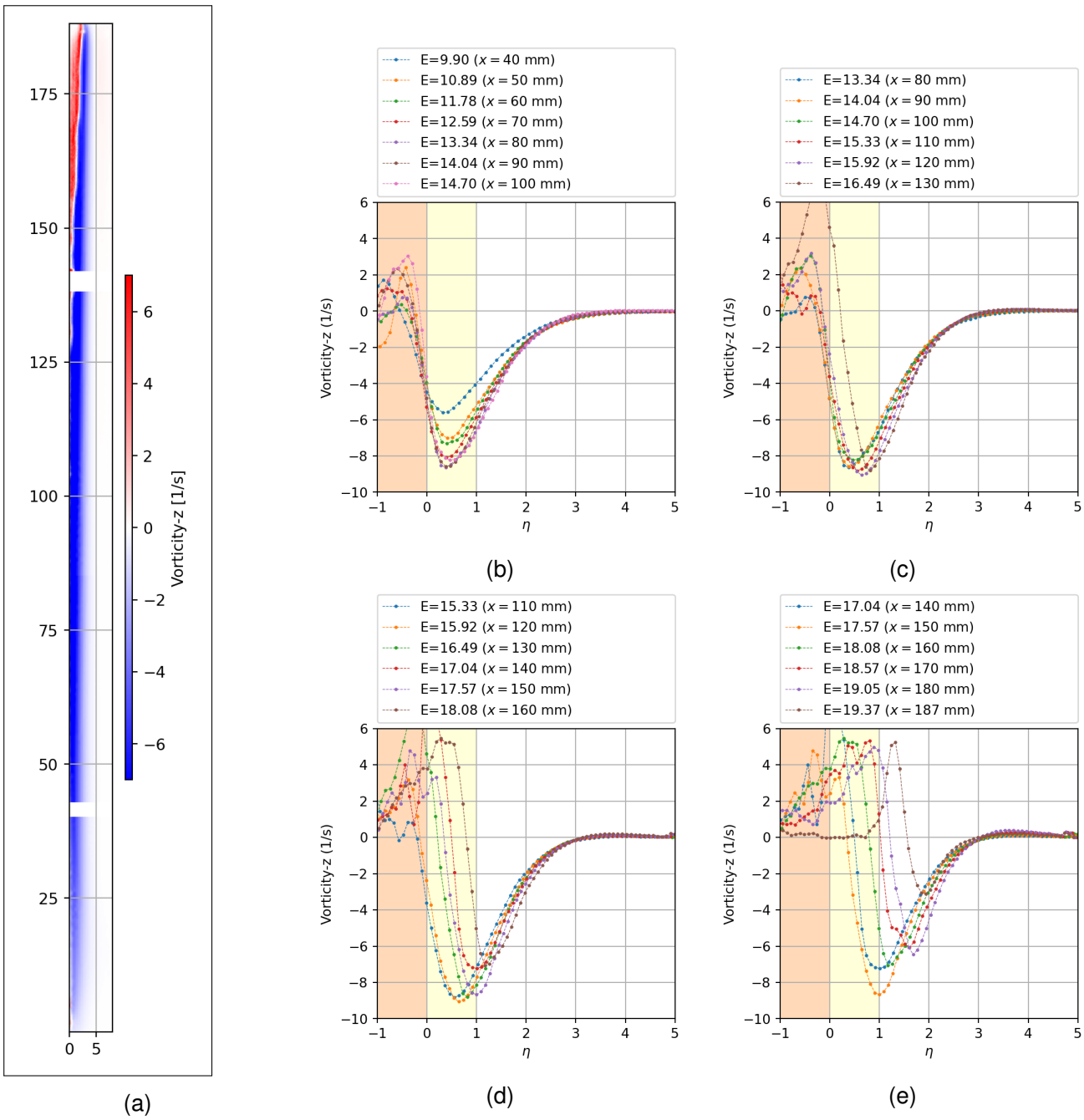

Figure 5.15: Plots of the corrected z component of vorticity. Regions shown are (a) the full field, (b) re-laminarisation of leading edge, (c) first transition, (d) second transition, and (e) trailing edge. The similarity parameter η is defined in eqn (2.27) and the heated surface to the left.

As for the displacement profiles, each region is discussed:

- Figure 5.15b shows the region $40\,\text{mm} \leq x \leq 100\,\text{mm}$. Similar to the displacement profiles the vorticity evolves from the leading edge. From Figure 5.3 one might expect to see a distinct evolution of the vorticity profile in the region $80\,\text{mm} \leq x \leq 90\,\text{mm}$ where the onset of hydrodynamic transition was predicted to occur. However, there is no such obvious evolution and it is assumed the hydrodynamic transition is delayed due to thermal stratification.
- Figure 5.15c shows the region $80\,\text{mm} \leq x \leq 130\,\text{mm}$. This covers the region where transition to turbulence was suggested to occur. It may be seen that the $x = 80, 90, 100\,\text{mm}$

profiles appear similar with the *magnitude* of the minima slightly reducing with x but the η location of the minima is approximately constant. One can see that from $x \geq 110$ mm the η location of the minima appears to increase with x thus indicating a transition.

- Figure 5.15d shows the region $110\,\text{mm} \leq x \leq 160\,\text{mm}$. This covers the region downstream from the onset of transition to turbulence up to the location where flow reversal was observed. It may be seen that the $x = 110, 120, 130$ mm profiles exhibit a continuous evolution of the profile with the minima occurring at increasing η locations with x. This is different to that observed in the displacement profiles and may indicate a growth in the hydrodynamic boundary layer independent of the thermal boundary layer. The profile at $x = 140$ mm has a reduction in magnitude which is then increased by $x = 150$ mm and then again reduced by $x = 160$ mm. Confusingly, the η location of the minima appears to increase for $x = 140$ mm, decrease slightly for $x = 150$ mm and then increase more substantially for $x = 160$ mm. Whilst the increase between profiles at $x = 150, 160$ mm might be related to the region of flow reversal, it is difficult to explain the behaviour at $x = 140$ mm. One possible explanation is that the duration of recordings were insufficient and thus the results don't truly represent a time averaged result. Another explanation is that this occurs at approximately the same position that the thermally refractive distortion increases and thus may be related to error in the BOS-correction method. Given much of this change occurs in the blurred, and thus low confidence, region this seems a reasonable conclusion. Nonetheless, as with the displacement results, a transition is observed to occur around $x \cong 150$ mm.
- Figure 5.15e shows the region $80\,\text{mm} \leq x \leq 130\,\text{mm}$. This covers the remainder of the heating surface downstream of the reversed flow. Unlike the displacement results, an additional potential transition may be seen (most easily in Figure 5.15a) to occur around $x = 170$ mm. The origin of this potential transition is difficult to identify. It may be due to a flow feature, insufficient recording duration, or a product of the flow becoming increasingly three dimensional. Thus, the assumption of a 2D refractive index field, upon which the BOS-correction method is determined, becomes invalid i.e. $\frac{\partial n}{\partial z} \neq 0$. Given the discrete nature of the transition the latter of these explanations is least likely.

Thus, the vorticity results appear to show the transitions occurring at the same locations as the displacement results. However, the second transition at $x \cong 150$ mm appears to have a different behaviour which is explained by the independent growth of the hydrodynamic boundary layer.

Identifying the exact location of transition is not the purpose of this work. Nevertheless it is clear a transition occurs and the flow undoubtedly starts to transition in the upper portion of the heater. Of particular interest is how different approaches to correction perform in the presence of such turbulence.

5.3.3 Comparison of instantaneous and time averaged correction methods

In the instantaneous correction, each individual PIV image is corrected by a corresponding BOS measurement. For the time averaged correction, each PIV image is corrected by the time averaged BOS measurement. The latter is akin to performing the PIV and BOS measurements separately and correcting them later (as performed by Elsinga et al.[52]).

Figure 5.16 shows the velocity and turbulent kinetic energy profiles toward the top of the heater where the flow is most turbulent. Compared are the profiles from the uncorrected and instantaneously corrected results in addition to results corrected by a time averaged distortion field. The time averaged distortion field is simply $\overline{\lambda^*}$. Since the flow is in a pseudo steady state, one would expect the time averaged velocity profiles to be in broad agreement for both the instantaneous and time averaged corrections. The corrected profiles appear to be in agreement up to $x = 150\,\text{mm}$ and then slightly disagree at $x \geq 160\,\text{mm}$. A similar, but more pronounced trend, is observed in the turbulent kinetic energy profiles shown in Figure 5.16b. Since the turbulent kinetic energy is proportional to the square of the instantaneous velocity, it is not surprising the effect is more apparent in those results.

It is quite apparent that the effect of the instantaneous and time averaged BOS-correction methods are dependent upon the amount of turbulence. In the results presented here the instantaneous correction method shows slightly higher values of velocity and turbulent kinetic energy. Furthermore, it may be seen that as the flow becomes increasingly turbulent the effect of the instantaneous and time averaged BOS-correction method becomes more disparate.

An explanation for this disparity is as follows. As the flow becomes increasingly turbulent there are expected to be turbulent fluctuations in the thermal boundary layer. This will result in thermal gradients that vary continuously with time due to turbulent motion and therefore result in a time dependent refractive distortion. The use of a time averaged correction method effectively decouples the time evolution of the thermal field from the hydrodynamic. Whereas in reality it is the turbulent motion which produces the thermal fluctuations via mass transport. One can picture this by considering a fixed location in the flow at a given instant and comparing the effect of the instantaneous and time averaged correction methods. At a given instant a turbulent fluctuation results in a local increase in mass flux as fluid is entrained from the near wall region. The time averaged corrected result would treat this fluid as moving through a time independent refraction field and distort the image of particles in this parcel of fluid accordingly. The instantaneous correction method would see the same fluid move but would also account for the instantaneous change in refraction which may see the particle images be more or less distorted. Whether the effect of refraction appeared to increase or decrease the distortion it would result in a correction that was further from the time average i.e. the particle images when corrected and processed would yield a faster or slower result. Since the result is further from the average, if this were repeated over time one would expect a different standard deviation of predicted velocities for that

location. This would explain the difference between instantaneous and time averaged turbulent kinetic energy.

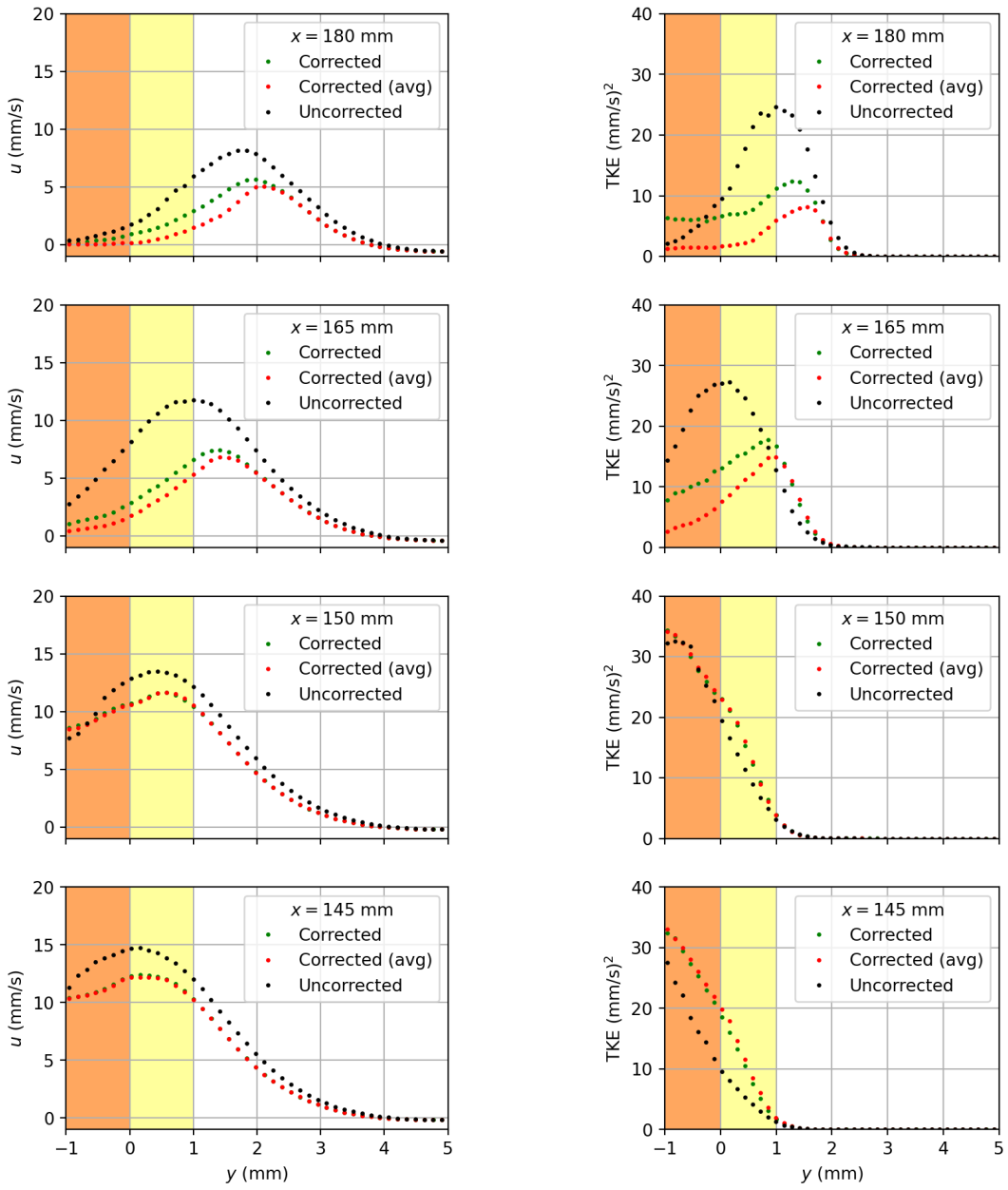

Figure 5.16: Comparison of (a) u component velocity, and, (b) turbulent kinetic energy profiles from the uncorrected, instantaneously corrected, and, time averaged corrected results. The heater is to the left.

5.4 Summary

5.4.1 BOS conclusions

- A method to experimentally determine the scaling factor is demonstrated.
- Comparison of an experimentally and analytically derived scaling factor highlight a benefit of the experimentally derived scaling factor; . This is suggested to be because the simplifying assumptions of an analytical solution do not match always faithfully represent the real world conditions. The experimental result trades the error due to simplifying assumptions for the errors and uncertainties in the measurements.
- It is noted that there currently exists no method to account for a variable scaling factor which one may expect to encounter in a stereoscopic or tomographic measurement of a transient thermo-convective flow phenomena.

5.4.2 PIV+BOS conclusions

It was shown that the necessity and applicability of the BOS-correction method may be divided into three regions;

1. A strictly laminar flow region where the effects of refractive distortion are negligible and correction may be unnecessary.
2. A weakly turbulent or transitioning flow where refractive distortion is non-negligible but may be corrected by an instantaneous or time averaged BOS measurement.
3. A more turbulent flow where the refractive distortion is most appropriately corrected by an instantaneous BOS measurement

5.4.3 Flow features

1. The onset of hydrodynamic and thermal transition to turbulence was observed to occur at $E \approx 15.92$ and $E \approx 17.87$, respectively.
2. A flow reversal was observed in the outer reaches of the hydrodynamic boundary layer which spanned upstream from in line with the trailing edge for the majority of the heating surface.
3. The velocity profiles in the turbulent region showed an unexpected trend which may be caused by curvature of the surface, flow reversal, trailing edge effect, or some combination thereof. Whilst the cause could not be definitively identified, it was confirmed not to be the result of refractive distortion.

Chapter 6

Conclusions and further work

6.1 Conclusions

The objectives of the work documented in this thesis are:

- Design an experimental apparatus and procedure to measure the effect of thermally induced refractive distortion on flow quantities measured using state-of-the-art flow visualisation techniques.
- Develop a correction method to account for the effects of thermally induced refractive distortion.
- Investigate the extent to which the effects of thermally induced refractive distortion can be considered negligible.

Design an experimental apparatus and procedure to measure the effect of thermally induced refractive distortion on flow quantities measured using state-of-the-art flow visualisation techniques - An experimental apparatus was produced that enabled simultaneous PIV and BOS measurements to be conducted. A psuedo 2D transitional flow was produced with local Rayleigh number in the range $0 < Ra_x^* < 4.211 \times 10^{11}$ with a relative uncertainty of $\pm 10.47\%$. This condition was achieved from a relatively small 187 mm square heater and a uniform high heat flux of $q'' = 8.21\,\text{kW/m}^2$.

The high heat flux and high refractivity of water resulted in substantial thermally induced refractive distortion in PIV. In addition thermal stratification of the reservoir fluid resulted in stratification induced distortion in the PIV images. Of the two contributions, the thermally induced refractive distortion was by far the greatest contributor. The distortions were observed to produce blurring, magnification and apparent displacement in the vicinity of the heated surface due to the variable refractive index field.

Develop a correction method to account for the effects of thermally induced refractive distortion - Measurements of displacement due to refractive distortion have been recorded using BOS. The BOS measurements are recorded simultaneously with the PIV measurements which are referred to as PIV+BOS. A novel feature of this work is the development of a method to correct the *instantaneous* distortion in the PIV measurements with the corresponding BOS measurement.

The BOS-correction method has been developed to correct for thermally induced refractive index resulting from both high thermal gradients and thermal stratification. The method is limited to pseudo 2D flow.

A novel experimental approach to determination of a scaling factor, which relates the distortion present in the BOS measurement to that in the PIV, has been developed. This results in a vector scaling factor rather than a singular value. The vector scaling factor is more tolerant of camera misalignment, slight variation from perpendicular viewing, and, misalignment of the PIV and BOS measurement planes.

A novel calibration procedure was produced to account for differences in the thermal conditions between calibration and experimental measurement conditions. This included difference in temperature and thermal stratification conditions.

Investigate the extent to which the effects of thermally induced refractive distortion can be considered negligible - It was found that for strictly laminar flows the effect of an instantaneous or time averaged correction made negligible difference to the velocity and turbulent measurements.

As the flow transitions to turbulence a correction is necessary. For very slightly turbulent flows correction by an instantaneous or time averaged approach yields similar results. However, very rapidly the two approaches yield different results. In general the application of the instantaneous correction method yielded slightly higher velocity and turbulent kinetic energy measurements than a time averaged correction. Both correction methods substantially reduced the velocity and turbulent kinetic energy measurements as compared with the uncorrected PIV results.

6.2 Further work

Recommendations are divided into applications, improvements and extensions of the BOS correction method:

New applications - The BOS correction technique enables water based PIV measurements to be conducted with greater certainty and in increasingly turbulent and challenging applications.

The application of the BOS correction in this work is to a case with relatively little time dependent behaviour. Whilst this was suitable for demonstrating the effect of correction for various levels of turbulence it is not a case which would most benefit from an instantaneous correction.

The BOS correction technique, when combined with the proposed calibration method, is probably best suited to correcting transient natural or forced convection problems. In such a problem the refractive distortion would vary continuously due to evolving thermal conditions which could not be corrected by a time averaged approach. One example observed, but not reported, in this work was the case for heater start up and the initiation of natural convection. In such a case the distortion is seen to develop continuously over time as the near wall thermal behaviour evolves and thermal stratification is established. In such a case the BOS correction performed much more substantial correction with excellent qualitative performance. The ability to perform measurements over longer time periods in a water based experiment may enable greater insight into the flow physics as the duration of the transient need no longer be constrained by the onset of thermal stratification and the stratification induced refractive distortion that accompanies it.

An alternative application is in the measurement of flow within a natural circulation loop, which is of significant interest to the nuclear industry. The stability of a natural circulation loop is such that the flow is frequently transient for extended periods of time and in some cases may never reach a steady state. Furthermore, the scaling restrictions for producing similar conditions to a reactor design are limiting for the choice of fluid and will prefer the use of water.

A further alternative is the study of stratification induced flows such as those encountered in thermal energy storage systems. In a recent publication by Otto and Cierpka[74] a water based PIV measurement was performed in the presence of, and driven by, thermal stratification. The flow was reported to have a turbulent behaviour in some locations. Whilst there was no mention of the characteristic smearing or blurring from refraction evident in the present work, it would be pertinent to ensure if, and to what extent, refraction is influencing the resultant velocity and turbulent fields as a fossilised error.

Improvements - A key shortcoming of the new methodology is the lack of quantitative verification and uncertainty quantification. Quantitative verification was not achieved in part due to the combination of several unintended phenomena which resulted in a complex flow for which a reasonable comparison could not be found in the literature. The unintended phenomena include

a concave heating surface due to manufacturing error, uncontrollable thermal stratification, and sharp leading and trailing edges.

A further iteration of the design of apparatus would see the following changes made:

- A stainless steel substrate for the plate heater would be specified to avoid corrosion and a ground surface mandated.
- Sharp edges on the heater would be replaced with rounded corners of known radius.
- The heater would be larger, with fewer joints and seals to simplify assembling and better guarantee a watertight seal.
- Thermocouples would be mounted into the surface in greater number, of improved calibration and located closer to the water.
- The lower portion of the reservoir would contain a trough or trap for deposited seeding particles and debris.
- The reservoir would feature replaceable glass viewing windows to avoid the damage experienced with acrylic.
- Improved measurement of the thermal stratification either by thermocouples or another method such as from BOS/LIF measurements.
- Improved and reconfigurable distribution of cooling to enable a variety of stratification conditions to be achieved.
- The use of a temperature controlled water circulating system to enable precise reproduction of calibration conditions. Similarly, intentionally different conditions could be produced to verify the calibration method, calibrate thermocouples in situ, and provide an easier means of temperature calibration for LIF measurements. Furthermore, this could be used to supply seeding material at or near the experimental conditions to ensure minimal disruption to the flow.
- For channel measurements the use of tin-doped indium oxide (ITO) heaters should be once again investigated to avoid the refraction of a light sheet illuminated from below.

With these unintended phenomena minimised, identification of a suitable verification case is more likely and more easily enables a companion analytical or computational study.

Alternatively, The current apparatus could remain in use and a supplementary non optical measurement of velocity could be performed simultaneously with the PIV+BOS. Thus, the uncertainty of the combined corrections could be reduced to that of the non optical method.

The BOS measurements could be improved through the use of a new BOS target which has improved contrast, reduced dot size and sharper dot images. The noise from the BOS target in PIV and LIF measurements can be reduced if a white on black, rather than black on white, BOS target is used. One way to achieve this would be to have a backlit BOS target where the dot pattern is a black non reflecting plate with precisely produced hole, rather than dot, pattern via lithography or a similar technique.

In this work recommendations for where a correction method is required and of what type were

made. The generality of these recommendations can be verified by performing a similar analysis to that perform in this work but for alternative geometries of varying size, alternative fluids and levels of turbulence. Due to the integral nature of the BOS measurement there is almost certainly a limitation on the level of turbulence to which the correction method can be applied. It is posited that a highly turbulent flow will result in 3D mixing of hot and cold fluid and therefore a 3D temperature gradient. Under such circumstances a light ray will become highly refracted along its path which may result in blurring, or the failing of one of the founding assumptions; that the displacement observed at the BOS plane is related to that at the PIV plane.

Extension of the BOS-correction method - The most obvious extension to the BOS-correction method is to determine the temperature field from the distortion field. For BOS measurements in air this is somewhat routine due to the applicability of the Gladstone-Dale equation. However, the more complex temperature dependence of refractive index in water makes this prospect less straight forward. Tokgoz et al.[56] demonstrated the determination of the temperature field in water from BOS measurements. However, this was for exceptionally small differences in temperature over which the refractive index may be considered constant. Over larger variations in temperature such an assumption is less applicable.

A further extension of the technique would see more of the blurred region recovered and yielding valid velocity vectors. Whilst some amount of improvement is likely achievable by improved BOS target design other approaches may similarly yield improvement. Cai et al.[60] employed a neural network to predict the flow behaviour that would otherwise be lost to blur and this certainly seems an interesting route. An alternative to perform PIV and BOS measurements using telecentric, rather than entocentric, lenses (a comparison is shown in Figure 6.1).

Telecentric lenses have been proposed to solve a number of optics limiting aspects of performing PIV measurements the first of which was by Konrath and Schröder[76] in relation to error in the stereoscopic measurement of out of plane velocity which incurred error due to parallax. Such lenses have been demonstrated to improve PIV[77] and BOS[78,79] measurements and may see greater adoption as image sensor pixel counts increase thereby introducing increased parallax error[80].

Elsinga et al.[52] provides a good explanation of the origin of blur for entocentric lenses. It is posited that the paraxial nature of a telecentric lens may reduce the extent of the blurred region by some amount. It seems likely there will always be some region that is irrecoverably lost due to blur and the smaller this region is the more simple and efficient a neural network correction would be. Hence the use of a telecentric lens and neural network is likely the approach that will best reduce data loss and error in blurred regions.

The use of a telecentric lens may offer further benefits. The first is the ability to perform simultaneous measurements of PIV and BOS in different planes from a single camera. This would be achievable as both planes could remain in focus whilst being located at different distances

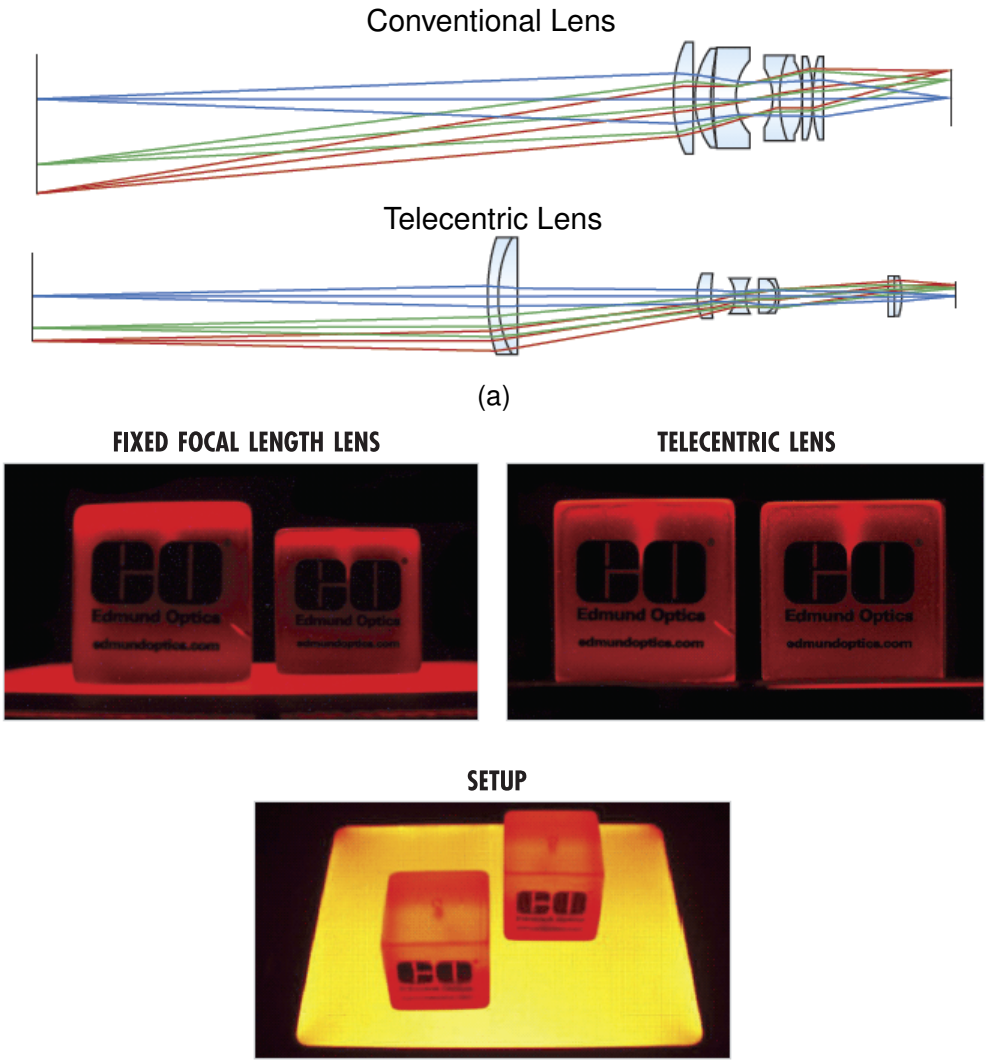

Figure 6.1: Comparison of (a) optical paths and (b) imagery of a conventional and telecentric lens, source Edmund Optics [75]

from the camera. However, with objects at different distances remaining in focus it seems likely the PIV seeding particles would introduce error in the BOS measurements and vica versa. This could perhaps be addressed through discrete illumination of each plane to correspond with a single frame of a PIV camera; similar to the original approach of Dalziel et al. [81]. Alternatively, one might consider the use of an optocoupler, which doubles or repeats an image such that it is repeated on the left and right side of an image sensor. Each half of the sensor could be viewed through a different filter which corresponds with the wavelength of light from the BOS target and the PIV seeding particles.

Extending this idea further, the use of a telecentric lens could enable a scanning approach to volume measurements. For PIV measurement of flow in a natural convection channel, this is particularly appealing. This is because the velocity is relatively slow which makes a scanning approach viable. Also, limited optical access due to the heaters which make up a channel makes tomographic measurements difficult to accommodate. Such a scanning approach was recently

demonstrated by Partridge et al.[51] where conventional entocentric lenses were used and a combined PIV and LIF approach, requiring optical access for three cameras. It seems likely that similar measurements of velocity and density fields could have been achieved by a single camera with an optocoupler and telecentric lens performing combined PIV and BOS measurements. In addition the reduced requirement for optical access and availability of cameras, this would simultaneously allow for correction of the PIV data and perhaps allow for a wider range of conditions or sources of refraction to be studied with their scanning approach.

Appendices

Appendix A

Derivation of optical distortion equations

Here the equations which describe how light travels through a variable refractive index media, and how this relates to a BOS measurement, are developed. Several authors describe the development of these equations in different ways and with different nomenclature. The nomenclature introduced in this work generally follows that of Dalziel et al.[57,81] and Elsinga et al.[52,72].

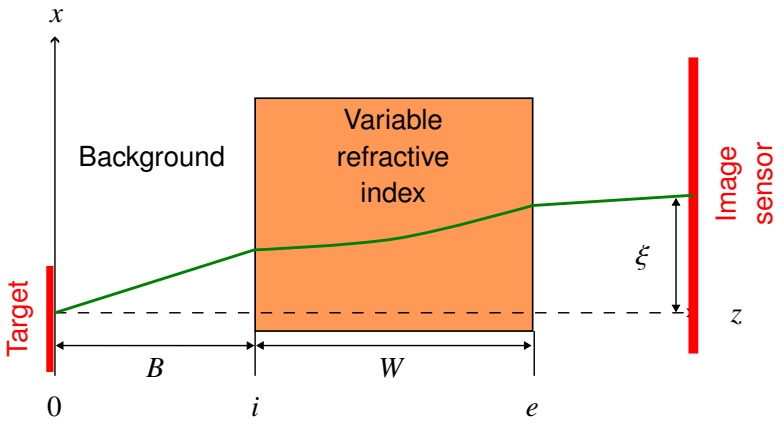

Figure A.1: A schematic of a simplified BOS measurement through a variable refractive index region. The optical axis is the z axis and the refracted path of the light is shown in green.

For brevity a generic simplified schematic is shown in Figure A.1. It may be seen that there are several regions:

1. A background region where a target is located somewhat removed from the variable refractive index field.
2. The variable refractive index field.
3. A region between the camera and variable refractive index field

As described in Merzkirch[82], a common starting point is that of Weyl[83] who presents Fermat's

variational principle as a set of differential equations

$$\frac{d^2\xi}{dz^2} = \left[1 + \left(\frac{d\xi}{dz}\right)^2 + \left(\frac{d\zeta}{dz}\right)^2\right]\frac{1}{n}\frac{\partial n}{\partial x} - \frac{d\xi}{dz}\frac{1}{n}\frac{\partial n}{\partial z} \tag{A.1}$$

$$\frac{d^2\zeta}{dz^2} = \left[1 + \left(\frac{d\xi}{dz}\right)^2 + \left(\frac{d\zeta}{dz}\right)^2\right]\frac{1}{n}\frac{\partial n}{\partial y} - \frac{d\zeta}{dz}\frac{1}{n}\frac{\partial n}{\partial z} \tag{A.2}$$

where ξ and ζ are the local displacement between the optical axis and the light path in the x and y direction, respectively.

Light rays which enter a camera lens nearly parallel to the optical axis are referred to as *paraxial*, whereas those towards the outer edges are *marginal*. It is instructive to consider the case of very slightly marginal light rays. Under these circumstances the displacement gradients are small but not zero i.e. $\frac{d\xi}{dz} \approxeq \frac{d\zeta}{dz} \to 0 \neq 0$. The square of such small quantities may still be considered negligible but an additional term on the right hand side remains.

$$\frac{d^2\xi}{dz^2} = \frac{1}{n}\frac{\partial n}{\partial x} - \frac{d\xi}{dz}\frac{1}{n}\frac{\partial n}{\partial z} \tag{A.3}$$

$$\frac{d^2\zeta}{dz^2} = \frac{1}{n}\frac{\partial n}{\partial y} - \frac{d\zeta}{dz}\frac{1}{n}\frac{\partial n}{\partial z} \tag{A.4}$$

The final term on the right hand side includes the gradient of the refractive index along the optical path $\frac{\partial n}{\partial z}$. If the refractive index field is considered 2D as described at the start of this chapter and stated in eqn (4.2), then $\frac{\partial n}{\partial z} \approxeq 0$ and can be neglected. As the field becomes more 3D this assumption does not hold.

Many authors[52,55,57,72,81] assume a paraxial measurement. By making this assumption the linear gradients of displacement $\frac{d\xi}{dz} \approxeq \frac{d\zeta}{dz} \approxeq 0$ and thus eqn (A.1) and (A.2) reduce to

$$\frac{d^2\xi}{dz^2} = \frac{1}{n}\frac{\partial n}{\partial x} \tag{A.5}$$

$$\frac{d^2\zeta}{dz^2} = \frac{1}{n}\frac{\partial n}{\partial y} \tag{A.6}$$

For brevity only the x-direction, and thus, ξ will be derived. However, the same steps are applicable in the y-direction for ζ. The intention is to derive an equation for ξ in each region and summate them to yield the culmulative displacement between target and image sensor.

First considering the background section. The origin is located at the target surface with z extended toward the camera. Starting with eqn (A.5) and noting there is no refractive index gradient

i.e. $\frac{\partial n}{\partial x} = 0$

$$\int_0 d\left(\frac{d\xi}{dz}\right) = 0 \int_0 dz \tag{A.7}$$

$$\frac{d\xi}{dz} = \left(\frac{d\xi}{dz}\right)_0 \tag{A.8}$$

$$\tag{A.9}$$

The gradient $\left(\frac{d\xi}{dz}\right)_0$ may be related to the angle of incidence with the target surface i.e.

$$\left(\frac{d\xi}{dz}\right)_0 = \tan\phi_0 \tag{A.10}$$

Substituting yields

$$\frac{d\xi}{dz} = \tan\phi_0 \tag{A.11}$$

$$\int_0 d\xi = \int_0 \tan\phi_0 dz \tag{A.12}$$

$$\xi = \xi_0 + z\tan\phi_0 \tag{A.13}$$

Finally the total displacement over this region occurs when $z = z_i = B$, hence,

$$\xi_i = \xi_0 + B\tan\phi_0 \tag{A.14}$$

Next the region with variable refractive index is considered, again starting from eqn (A.5).

$$\int_i d\left(\frac{d\xi}{dz}\right) = \int_i \frac{1}{n}\frac{\partial n}{\partial x} dz \tag{A.15}$$

$$\frac{d\xi}{dz} = \tan\phi_i + z\frac{1}{n_0}\frac{\partial n}{\partial x} - B\frac{1}{n_b}\frac{\partial n}{\partial x} \tag{A.16}$$

$$\int_i d\xi = \int_i \tan\phi_i dz + \int_i z\frac{1}{n}\frac{\partial n}{\partial x} dz - \int_i B\frac{1}{n_b}\frac{\partial n}{\partial x} dz \tag{A.17}$$

$$\xi = \xi_i + z\tan\phi_i + \left(\frac{z^2}{2}\right)\frac{1}{n_0}\frac{\partial n}{\partial x} - zB\frac{1}{n_b}\frac{\partial n}{\partial x} \tag{A.18}$$

Snell's law[82] for small angles can be used to replace the unknown $\tan\phi_i$ term accounting for any

difference in the refractive index between the two media

$$n_b \tan\phi_0 = n_0 \tan\phi_i \tag{A.19}$$

$$\tan\phi_i = \left(\frac{n_b}{n_0}\right)\tan\phi_0 \tag{A.20}$$

Substituting this and eqn (A.14) into eqn (A.18) yields

$$\xi = \xi_0 + B\tan\phi_0 + z\left(\frac{n_b}{n_0}\right)\tan\phi_0 + \left(\frac{z^2}{2}\right)\frac{1}{n_0}\frac{\partial n}{\partial x} - zB\frac{1}{n_b}\frac{\partial n}{\partial x} \tag{A.21}$$

$$\xi = \xi_0 + \left[B + z\left(\frac{n_b}{n_0}\right)\right]\tan\phi_0 + \left[\frac{z}{2}\left(z - 2\frac{n_0}{n_b}B\right)\right]\frac{1}{n_0}\frac{\partial n}{\partial x} \tag{A.22}$$

$$\xi_e = \xi_0 + \left[B + W\left(\frac{n_b}{n_0}\right)\right]\tan\phi_0 + \left[\frac{W}{2}\left(W - 2\frac{n_0}{n_b}B\right)\right]\frac{1}{n_0}\frac{\partial n}{\partial x} \tag{A.23}$$

At this point it is worth comparing eqn (A.23) to that proposed by Dalziel et al.[57] and Elsinga et al.[52]. It should be noted these equations have been adjusted to conform with the nomenclature and orientation of axis defined in this work and thus appear slightly different to their original presentation.

$$\xi_e = \xi_0 + \left[\frac{W}{2}\left(W - 2\frac{n_0}{n_b}B\right)\right]\frac{1}{n_0}\frac{\partial n}{\partial x} \qquad \text{(Dalziel et al.[57])}$$

$$\xi_e = \xi_0 + \left[\frac{W^2}{2}\right]\frac{1}{n_0}\frac{\partial n}{\partial x} \qquad \text{(Elsinga et al.[52])}$$

It may be seen that if a perfectly perpendicular alignment between target and optical axis is assumed then $\tan\phi_0 = 0$ and eqn (A.23) becomes identical to that of Dalziel et al.[57]. If a further assumption is made that $n_b \equiv n_0$ and the target is located at the extent of the variable refractive index region i.e. $B = 0$, then eqn (A.23) becomes identical to that of Elsinga et al.[52]. For Elsinga et al.[52] the fluid in and around their test section was air which was approximated to unity by the authors. Whereas Dalziel et al.[81] had an aqueous test section surrounded by air. Furthermore, Dalziel et al.[57] also accounted for the refraction of the windows in the test section between the background and region of variable refractive index to yield

$$\xi_e = \xi_0 + \left[\frac{W}{2}\left(W - 2\frac{n_0}{n_b}B - 2\frac{n_0}{n_T}T\right)\right]\frac{1}{n_0}\frac{\partial n}{\partial x} \qquad \text{(Dalziel et al.[57])}$$

where T and n_T are the wall thickness and refractive index, respectively.

In the current work the target is located at the extent of the variable refractive index field and thus $B = 0$. Hence, for the simplified case considered here, eqn (A.23) simplifies to

$$\xi_e = \xi_0 + W\tan\phi_0 + \left[\frac{W^2}{2}\right]\frac{1}{n_0}\frac{\partial n}{\partial x} \tag{A.24}$$

Bibliography

1. D. Bestion, R. Camy, C. Heib, O. Marfaing, F. Moretti, and T. Skorek. Requirements for cfd-grade experiments for nucelar reactor thermalhydraulics. URL https://hal-cea.archives-ouvertes.fr/cea-02328974/document.

2. IAEA. Tecdoc 1474 - natural circulation in water cooled nuclear power plants. Technical report, International Atomic Energy Agency, 2005.

3. IAEA. Tecdoc 1624 - passive safety systems and natural circulation in water cooled nuclear power plants. Technical report, International Atomic Energy Agency, 2009.

4. B. Gebhart, Y. Jaluria, R. L. Mahajan, and B. Sammakia. *Buoyancy induced flows and transport*. Hemisphere, 1988.

5. J. P. Holman. *Heat Transfer*. McGraw Hill, 10 edition, 2010.

6. F. P. Incropera and D. P. DeWitt. *Fundamentals of Heat and Mass Transfer*. Wiley, fourth edition, 1996.

7. G. F. Hewitt. *Heat exchanger design handbook 2008*. Begell House, New York, 2008. ISBN 9781567002553.

8. P. H. Oosthuizen and A. Y. Kalendar. Natural convective heat transfer from narrow vertical plates. In *Natural Convective Heat Transfer from Narrow Plates*, pages 15–30. Springer New York, aug 2012. doi: 10.1007/978-1-4614-5158-7_2.

9. P. H. Oosthuizen. Free convection: External surface. In *Handbook of Thermal Science and Engineering*, pages 527–602. Springer International Publishing, 2018. doi: 10.1007/978-3-319-26695-4_10.

10. A. Ede. Advances in free convection. In *Advances in Heat Transfer*, pages 1–64. Elsevier, 1967. doi: 10.1016/s0065-2717(08)70272-7.

11. E. M. Sparrow and J. L. Gregg. Laminar free convection from a vertical plate with uniform surface heat flux. In *Trans. ASME*.

12. E. Pohlhausen. Der wärmeauwärme zwischen festen kr̈pern und flüssigkeiten mit kleiner reibung und kleiner wärmewärme. *—eitschrift für Angewandte Mathematik unt Mechanik*, 1921.

13. E. Schmidt and W. Beckmann. Das temperatur- und geschwindigkeitsfeld vor einer wärme abgebenden senkrechten platte bei natürlicher konvektion. *Technische Mechanik und Thermodynamik*, 1930.

14. S. Ostrach. Analysis of laminar free-convection flow and heat transfer about a flat plate parallel to the direction of the generating body force. Technical Report 2635, NACA, 1952.

15. G. C. Vliet. Natural convection local heat transfer on constant heat flux inclined surfaces. *Int. J. Heat Mass Transfer*, 1969. URL https://sci-hub.se/10.1115/1.3580236.

16. S. Churchill and H. Chu. Correlating equations for laminar and turbulent free convection from a vertical plate. *International Journal of Heat and Mass Transfer*, 1975.

17. S. W. Churchill. *Heat exchanger design handbook*, volume 2, chapter 2.5.7 - Free convection around immersed bodies. begell house inc. publishers, 2008.

18. T. Fujii and H. Imura. Natural-convection heat transfer from a plate with arbitrary inclination. *International Journal of Heat and Mass Transfer*, 1972.

19. F. Godaux and B. Gebhart. An experimental study of the transition of natural convection flow adjacent to a vertical surface. *International Journal of Heat and Mass Transfer*, 17(1): 93–107, jan 1974. doi: 10.1016/0017-9310(74)90042-8.

20. Y. Jaluria and B. Gebhart. On transition mechanisms in vertical natural convection flow. *Journal of Fluid Mechanics*, 66(2):309–337, nov 1974. doi: 10.1017/s002211207400022x.

21. R. L. Mahajan and B. Gebhart. An experimental determination of transition limits in a vertical natural convection flow adjacent to a surface. *Journal of Fluid Mechanics*, 91(01):131, mar 1979. doi: 10.1017/s0022112079000070.

22. G. C. Vliet and C. K. Liu. An experimental study of turbulent natural convection boundary layers. *Journal of Heat Transfer*, 91(4):517–531, nov 1969. doi: 10.1115/1.3580236.

23. Y. Joshi and B. Gebhart. Transition of transient vertical natural-convection flows in water. *Journal of Fluid Mechanics*, 179:407–438, jun 1987. doi: 10.1017/s0022112087001599.

24. Y. Zhao, C. Lei, and J. C. Patterson. PIV measurements of the k-type transition in natural convection boundary layers. *Experimental Thermal and Fluid Science*, 101:62–75, jan 2019. doi: 10.1016/j.expthermflusci.2018.09.007.

25. Y. Jaluria and B. Gebhart. Stability and transition of buoyancy-induced flows in a stratified medium. *Journal of Fluid Mechanics*, 66(3):593–612, nov 1974. doi: 10.1017/s0022112074000383.

26. J. Tanny and J. Cohen. The mean temperature field of a buoyancyinduced boundary layer adjacent to a vertical plate immersed in a stratified medium. *International Journal of Heat and Mass Transfer*, 41(14):2125–2130, jul 1998. doi: 10.1016/s0017-9310(97)00350-5.

27. S. Paolucci and Z. J. Zikoski. Free convective flow from a heated vertical wall immersed in a thermally stratified environment. *International Journal of Heat and Mass Transfer*, 67: 1062–1071, dec 2013. doi: 10.1016/j.ijheatmasstransfer.2013.08.076.

28. K. Oswatitsch, L. Prandtl, and K. Wieghardt. *Führer durch die Strömungslehre*. Vieweg+Teubner Verlag, 2013. ISBN 9783322994912. URL https://www.ebook.de/de/product/33503625/klaus_oswatitsch_ludwig_prandtl_karl_wieghardt_fuehrer_durch_die_stroemungslehre.html.

29. M. Raffell, C. Willert, S. Wereley, and J. Kompenhans. *Particle Image Velocimetry - A Practical Guide*. Springer, 2007.

30. LaVision. *DaVis 10.2 Software*.

31. M. Thebault, J. Reizes, S. Giroux-Julien, V. Timchenko, and C. Ménézo. Impact of external temperature distribution on the convective mass flow rate in a vertical channel – a theoretical and experimental study. *International Journal of Heat and Mass Transfer*, 121:1264–1272, jun 2018. doi: 10.1016/j.ijheatmasstransfer.2018.01.081.

32. L. Verso and A. Liberzon. Background oriented schlieren in a density stratified fluid. *Review of Scientific Instruments*, 86(10):103705, oct 2015. doi: 10.1063/1.4934576.

33. E. Archbold and A. Ennos. Displacement measurement from double-exposure laser photographs. *Optica Acta: International Journal of Optics*, 19(4):253–271, apr 1972. doi: 10.1080/713818559.

34. D. B. Barker and M. E. Fourney. Measuring fluid velocities with speckle patterns. *Optics Letters*, 1(4):135, oct 1977. doi: 10.1364/ol.1.000135.

35. P. G. Simpkins and T. D. Dudderar. Laser speckle measurements of transient bénard convection. *Journal of Fluid Mechanics*, 89(4):665–671, dec 1978. doi: 10.1017/s0022112078002797.

36. D. Dabiri and M. Gharib. The effects of forced boundary conditions on flow within a cubic cavity using digital particle image thermometry and velocimetry (DPITV). *Experimental Thermal and Fluid Science*, 13(4):349–363, nov 1996. doi: 10.1016/s0894-1777(96)00113-6.

37. Y. Zhao, C. Lei, and J. C. Patterson. A PIV measurement of the natural transition of a natural convection boundary layer. *Experiments in Fluids*, 56(1), jan 2015. doi: 10.1007/s00348-014-1891-5.

38. Y. Hattori, T. Tsuji, Y. Nagano, and N. Tanaka. Effects of freestream on turbulent combined-convection boundary layer along a vertical heated plate. *Int. J. Heat and Fluid flows*, 22(3): 315–322, jun 2001. doi: 10.1016/s0142-727x(01)00094-7.

39. E. Sanvicente, S. Giroux-Julien, C. Ménézo, and H. Bouia. Transitional natural convection flow and heat transfer in an open channel. *International Journal of Thermal Sciences*, 63: 87–104, jan 2013. doi: 10.1016/j.ijthermalsci.2012.07.004.

40. O. Tkachenko, V. Timchenko, S. Giroux-Julien, C. Ménézo, G. Yeoh, J. Reizes, E. Sanvicente, and M. Fossa. Numerical and experimental investigation of unsteady natural convection in a non-uniformly heated vertical open-ended channel. *International Journal of Thermal Sciences*, 99:9–25, jan 2016. doi: 10.1016/j.ijthermalsci.2015.07.029.

41. T. F. Ayinde, S. A. M. Said, and M. A. Habib. Experimental investigation of turbulent natural convection flow in a channel. *Heat and Mass Transfer*, 42(3):169–177, sep 2005. doi: 10.1007/s00231-005-0017-2.

42. T. F. Ayinde, S. A. M. Said, and M. A. Habib. Turbulent natural convection flow in a vertical channel with anti-symmetric heating. *Heat and Mass Transfer*, 44(10):1207–1216, nov 2007. doi: 10.1007/s00231-007-0359-z.

43. E. Sanvicente. *Experimental investigation of thermal and fluid dynamical behavior of flows in open-ended channels : Application to Building Integrated Photovoltaic (BiPV) Systems*. Theses, INSA de Lyon, July 2013. URL https://tel.archives-ouvertes.fr/tel-00961231.

44. T. Tsuji, T. Kajitani, and T. Nishino. Heat transfer enhancement in a turbulent natural convection boundary layer along a vertical flat plate. *International Journal of Heat and Fluid Flow*, 28(6):1472–1483, dec 2007. doi: 10.1016/j.ijheatfluidflow.2007.04.021.

45. R. P. Laein, S. Rashidi, and J. A. Esfahani. Experimental investigation of nanofluid free convection over the vertical and horizontal flat plates with uniform heat flux by PIV. *Advanced Powder Technology*, 27(2):312–322, mar 2016. doi: 10.1016/j.apt.2015.12.011.

46. M. A. Habib, S. A. M. Said, S. A. Ahmed, and A. Asghar. Velocity characteristics of turbulent natural convection in symmertrically and asymmetrically heated vertical channels. *Exp. Thermal Fluids*, 2002.

47. C. Daverat, Y. Li, H. Pabiou, C. Ménézo, and S. Xin. Transition to turbulent heat transfer in heated vertical channel - experimental analysis. *International Journal of Thermal Sciences*, 111:321–329, jan 2017. doi: 10.1016/j.ijthermalsci.2016.09.004.

48. A. Sciacchitano. Uncertainty quantification in particle image velocimetry. *Measurement Science and Technology*, 30(9):092001, jul 2019. doi: 10.1088/1361-6501/ab1db8.

49. Y. Joshi and B. Gebhart. Measurements and visualizations of transient and steady-state vertical natural convection flow in cold water. *International Journal of Heat and Mass Transfer*, 29(11):1723–1740, nov 1986. doi: 10.1016/0017-9310(86)90112-2.

50. A. Alahyari and E. K. Longmire. Particle image velocimetry in a variable density flow: application to a dynamically evolving microburst. *Experiments in Fluids*, 17(6):434–440, oct 1994. doi: 10.1007/bf01877047.

51. J. L. Partridge, A. Lefauve, and S. B. Dalziel. A versatile scanning method for volumetric measurements of velocity and density fields. *Measurement Science and Technology*, 30(5): 055203, apr 2019. doi: 10.1088/1361-6501/ab0bfd.

52. G. E. Elsinga, B. W. van Oudheusden, and F. Scarano. Evaluation of aero-optical distortion effects in PIV. *Experiments in Fluids*, 39(2):246–256, jul 2005. doi: 10.1007/s00348-005-1002-8.

53. C. F. Ihle, S. B. Dalziel, and Y. Niño. Simultaneous particle image velocimetry and synthetic schlieren measurements of an erupting thermal plume. *Measurement Science and Technology*, 20(12):125402, oct 2009. doi: 10.1088/0957-0233/20/12/125402.

54. G. E. A. Meier. New optical tools for fluid mechanics. *Sadhana*, 23(5-6):557–567, oct 1998. doi: 10.1007/bf02744579.

55. M. Raffel. Background-oriented schlieren (BOS) techniques. *Experiments in Fluids*, 56(3), mar 2015. doi: 10.1007/s00348-015-1927-5.

56. S. Tokgoz, R. Geisler, L. J. A. van Bokhoven, and B. Wieneke. Temperature and velocity measurements in a fluid layer using background-oriented schlieren and PIV methods. *Measurement Science and Technology*, 23(11):115302, oct 2012. doi: 10.1088/0957-0233/23/11/115302.

57. S. B. Dalziel, M. Carr, J. K. Sveen, and P. A. Davies. Simultaneous synthetic schlieren and PIV measurements for internal solitary waves. *Measurement Science and Technology*, 18 (3):533–547, jan 2007. doi: 10.1088/0957-0233/18/3/001.

58. J. Wu, H. Xu, F. Song, J. Xu, Y. Li, and T. Wang. Temperature field reconstruction in high-temperature gas by using the colored background oriented schlieren method. doi: 10.15918/j.jbit1004-0579.20053.

59. S. Amjad, S. Karami, J. Soria, and C. Atkinson. Assessment of three-dimensional density measurements from tomographic background-oriented schlieren (BOS). *Measurement Science and Technology*, 31(11):114002, sep 2020. doi: 10.1088/1361-6501/ab955a.

60. S. Cai, Z. Wang, F. Fuest, Y. J. Jeon, C. Gray, and G. E. Karniadakis. Flow over an espresso cup: inferring 3-d velocity and pressure fields from tomographic background oriented schlieren via physics-informed neural networks. *Journal of Fluid Mechanics*, 915, mar 2021. doi: 10.1017/jfm.2021.135.

61. J. K. Davis, C. J. Clifford, D. L. Kelly, and B. S. Thurow. Tomographic background oriented schlieren using plenoptic cameras. *Measurement Science and Technology*, 33(2):025203, dec 2021. doi: 10.1088/1361-6501/ac3b09.

62. J. K. Sveen and S. B. Dalziel. A dynamic masking technique for combined measurements of PIV and synthetic schlieren applied to internal gravity waves. *Measurement Science and Technology*, 16(10):1954–1960, aug 2005. doi: 10.1088/0957-0233/16/10/010.

63. L. K. Rajendran, S. P. M. Bane, and P. P. Vlachos. PIV/BOS synthetic image generation in variable density environments for error analysis and experiment design. *Measurement Science and Technology*, 30(8):085302, jul 2019. doi: 10.1088/1361-6501/ab1ca8.

64. E. Sparrow and L. Azevedo. Vertical-channel natural convection spanning between the fully-developed limit and the single-plate boundary-layer limit. *International Journal of Heat and Mass Transfer*, 28(10):1847–1857, oct 1985. doi: 10.1016/0017-9310(85)90207-8.

65. C. Daverat, H. Pabiou, C. Menezo, H. Bouia, and S. Xin. Experimental investigation of turbulent natural convection ina vertical water channel with symmetric heating: Flow and heat transfer. *Exp. Thermal Fluids*, 2013.

66. W. Elenbaas. Heat dissipation of parallel plates by free convection. *Physica*, XI(1), January 1942.

67. *Metrix MTX 3293 user manual*. Chauvin Arnoux Ltd. URL https://www.aemc.com/userfiles/files/resources/usermanuals/Multimeters/MTX3292-3293_EN.pdf.

68. H. W. Coleman and W. G. Steele. *Experimentation, validation, and uncertainty analysis for engineers*. Third edition, 2009.

69. Omega. *HFS-5 Heat FluxSensor Datasheet*. URL https://assets.omega.com/spec/Omega_Heat_Flux_Sensor.pdf.

70. *Datasheet NI9201*. URL https://www.ni.com/pdf/manuals/373783a_02.pdf.

71. Revised supplementary release on properties of liquid water at 0.1 mpa. Technical report, The International Association for the Properties of Water and Steam. URL http://www.iapws.org/relguide/LiquidWater.pdf.

72. G. E. Elsinga, B. W. van Oudheusden, F. Scarano, and D. W. Watt. Assessment and application of quantitative schlieren methods: Calibrated color schlieren and background oriented schlieren. 36(2):309–325. doi: 10.1007/s00348-003-0724-8.

73. K. A. Stroud. *Engineering mathematics*. Palgrave Macmillan. ISBN 9781403942463.

74. H. Otto and C. Cierpka. Influence of thermal stratification on vertical natural convection—experimental investigations on the example of thermal energy storage systems. *Physics of Fluids*, 33(8):083614, aug 2021. doi: 10.1063/5.0056232.

75. Edmund Optics. Imaging optics resource guide. URL https://www.edmundoptics.co.uk/knowledge-center/industry-expertise/imaging-optics/imaging-resource-guide/.

76. R. Konrath and W. Schröder. Telecentric lenses for imaging in particle image velocimetry: a new stereoscopic approach. *Experiments in Fluids*, 33(5):703–708, nov 2002. doi: 10.1007/s00348-002-0531-7.

77. T. Fournel, S. Coudert, C. Fournier, and C. Ducottet. Stereoscopic particle image velocimetry using telecentric lenses. *Measurement Science and Technology*, 14(4):494–499, mar 2003. doi: 10.1088/0957-0233/14/4/313.

78. M. Ota, F. Leopold, R. Noda, and K. Maeno. Improvement in spatial resolution of background-oriented schlieren technique by introducing a telecentric optical system and its application to supersonic flow. *Experiments in Fluids*, 56(3), feb 2015. doi: 10.1007/s00348-015-1919-5.

79. F. Cozzi, E. Göttlich, L. Angelucci, V. Dossena, and A. Guardone. Development of a background-oriented schlieren technique with telecentric lenses for supersonic flow. *Journal of Physics: Conference Series*, 778:012006, jan 2017. doi: 10.1088/1742-6596/778/1/012006.

80. B. Sun, M. Shehzad, D. Jovic, C. Cuvier, C. Willert, Y. Ostovan, J.-M. Foucaut, C. Atkinson, and J. Soria. Distortion correction of two-component two-dimensional PIV using a large imaging sensor with application to measurements of a turbulent boundary layer flow at $Re_\tau = 2386$. *Experiments in Fluids*, 62(9), aug 2021. doi: 10.1007/s00348-021-03273-w.

81. S. B. Dalziel, G. O. Hughes, and B. R. Sutherland. Whole-field density measurements by 'synthetic schlieren'. *Experiments in Fluids*, 28(4):322–335, apr 2000. doi: 10.1007/s003480050391.

82. W. Merzkirch. *Flow visualization*. Academic Press, Orlando, 1987. ISBN 9780124913516.

83. F. J. Weyl. *Analysis of optical methods*. Princeton university press.